ABSTRACT

ATMOSPHERIC MERCURY CHEMISTRY: DETECTION, KINETICS, AND MECHANISM

by
Na Mao

The presence of mercury in the environment is of global concern due to its toxicity. The atmosphere is an important transient reservoir for mercury released by human activities and natural sources. The knowledge of atmospheric mercury chemistry is critical for understanding the global biogeochemical cycle. In the atmosphere, mercury primarily exists in three forms: gaseous elemental mercury (GEM), gaseous oxidized mercury (GOM), and particulate-bound mercury (PBM). Over the last decade, the existing knowledge of mercury cycle has dramatically changed: (1) There has been increasing evidence that current detection methods do not accurately quantify gaseous oxidized mercury and a technique which could do both quantitative measurements and molecular speciation of atmospheric oxidized mercury is needed. (2) The gas-phase oxidation of elemental mercury initiated by bromine radical has been proposed as the major oxidation pathway, however, the experimental confirmation for the fate of HgBr radical is limited. (3) Heterogeneous reactions of gaseous oxidized mercury on environmental surfaces are poorly understood.

Accordingly, the **goal** of this work is (a) to develop a new mass spectrometry-based detection technique, which can be employed for both laboratory and field measurements of gaseous oxidized mercury and use this technique to investigate the (b) heterogeneous reactions of gaseous oxidized mercury with environmental surfaces; and (c) the kinetics and mechanism of gas-phase reactions of elemental mercury to form gaseous oxidized

mercury. This work has broad implications, it provides a better understanding of mercury chemistry in mechanisms and kinetics, which helps to model the atmospheric mercury cycle, enhance our current knowledge concerning the biogeochemical cycling of mercury, broaden our understanding of the mercury chemistry in the atmosphere, and provide a direct detection technique of atmospheric mercury which can be applied in future field and laboratory studies.

ATMOSPHERIC MERCURY CHEMISTRY: DETECTION, KINETICS, AND MECHANISM

by
Na Mao

A Dissertation
Submitted to the Faculty of
New Jersey Institute of Technology
in Partial Fulfillment of the Requirements for the Degree of
Doctor of Philosophy in Environmental Science

Department of Chemistry and Environmental Science

May 2022

APPROVAL PAGE

ATMOSPHERIC MERCURY CHEMISTRY: DETECTION, KINETICS, AND MECHANISM

Na Mao

Dr. Alexei Khalizov, Dissertation Advisor — Date
Associate Professor of Chemistry and Environmental Science, NJIT

Dr. Hao Chen, Committee Member — Date
Professor of Chemistry and Environmental Science, NJIT

Dr. Farnaz A Shakib, Committee Member — Date
Assistant Professor of Chemistry and Environmental Science, NJIT

Dr. Yuanwei Zhang, Committee Member — Date
Assistant Professor of Chemistry and Environmental Science, NJIT

Dr. Yuan Gao, Committee Member — Date
Professor of Earth and Environmental Sciences, Rutgers University-Newark

BIOGRAPHICAL SKETCH

Author: Na Mao

Degree: Doctor of Philosophy

Date: May 2022

Undergraduate and Graduate Education:

- Doctor of Philosophy in Environmental Science,
  New Jersey Institute of Technology, Newark, NJ, 2022

- Bachelor of Science in Environmental Science,
  Jilin University, Changchun, P. R. China, 2017

Major: Environmental Science

Presentations and Publications:

Publications:

Mao, N., Khalizov, A., The pH Dependence of Reactivity of Particle Phase Organic Acids with Gaseous Oxidized Mercury, in preparation, 2022.

Mao, N., Khalizov, A. Binding of Mercuric Halides with the (100) Surface of Sodium Chloride, in preparation, 2022.

Mao, N., Khalizov, A. (2021). Exchange Reactions Alter Molecular Speciation of Gaseous Oxidized Mercury. *ACS Earth and Space Chemistry*. *5* (8), 1842-1853.

Mao, N., Antley, J., Cooper, M., Shah, N., Kadam, A., & Khalizov, A. (2021). Heterogeneous Chemistry of Mercuric Chloride on Inorganic Salt Surfaces. *The Journal of Physical Chemistry A, 125*(18), 3943-3952.

Khalizov, A. F., Guzman, F. J., Cooper, M., Mao, N., Antley, J., & Bozzelli, J. (2020). Direct Detection of Gas-Phase Mercuric Chloride by Ion Drift – Chemical Ionization Mass Spectrometry. *Atmospheric Environment*, *238*, 117687.

Presentations:

Mao, N., Khalizov, A., Heterogeneous Uptake of $HgCl_2$ on Carbonaceous Aerosol Surfaces, Presented virtually at 40^{TH} Regional Meeting on Kinetics and Dynamics, Jan 29, 2022

Mao, N., Khalizov, A., Heterogeneous Uptake of $HgCl_2$ on Carbonaceous Aerosol Surfaces, Presented at Annual Fall Meeting of the American Geophysical Union (AGU), December 13-17, 2021, New Orleans, LA.

Mao, N., Nguyen, D., Khalizov, A., Fast Ligand Exchange during Analysis of Gaseous Oxidized Mercury, Presented virtually at 39^{TH} Regional Meeting on Kinetics and Dynamics, Jan 30, 2021.

Mao, N., Nguyen, D., Khalizov, A., Possible Exchange Reactions during Analysis of Gaseous Oxidized Mercury, Presented at Annual Fall meeting of the American Geophysical Union (AGU), December 1-17, 2020, online.

Mao, N., Nguyen, D., Khalizov, A., Possible Exchange Reactions during Analysis of Gaseous Oxidized Mercury, Presented virtually at the Annual Meeting of the Mid Atlantic Section of the American Physical Society, Dec 4-6, 2020.

Mao, N., Antley, J., Cooper, M., Shah, N., Kadam, A., & Khalizov, A., Gas-Surface Uptake of Gaseous Oxidized Mercury on Inorganic Salts, Presented at Air and Waste Management Association Student Poster Competition (AWMAS), March 4, 2020, New Brunswick, NJ.

Mao, N., Antley, J., Cooper, M., Shah, N., Kadam, A., & Khalizov, A., Mechanism for Gas-Surface Uptake of Gaseous Oxidized Mercury on Inorganic Salts, Presented at The Dana Knox Student Research Showcase, April 17, 2019, Newark, NJ.

Mao, N., Antley, J., Cooper, M., Shah, N., Kadam, A., & Khalizov, A., Gas-Surface Uptake of Gaseous Oxidized Mercury on Inorganic Salts, Presented at the 104^{TH} Annual New Jersey Water Environment Association (NJWEA) Conference, May 8, 2019, Atlantic City, NJ.

Mao, N., Antley, J., Cooper, M., Shah, N., Kadam, A., & Khalizov, A., Gas-Surface Uptake of Gaseous Oxidized Mercury on Inorganic Salts, Presented at 37^{TH} Regional Meeting on Kinetics and Dynamics, January 26, 2019, Hartford, CT.

Mao, N., Antley, J., Cooper, M., Shah, N., Kadam, A., & Khalizov, A., Gas-Surface Uptake of Gaseous Oxidized Mercury on Inorganic Salts, Presented at Annual Fall Meeting of the American Geophysical Union (AGU), December 10-14, 2018, Washington, DC.

To my parents:
Yufeng Mao (Daddy) and Limei Lu (Mummy)
Thank you for your unconditional love and consistent support throughout this journey.

To my grandparents:
Zhiming Mao (Grandfather) and Chunfang Liu (Grandmother)
For your consistent support, kindness, and warmth. You have always been there for me.

To my brother:
Junhao Mao
For always believing me and cheering me on.

To my boyfriend:
Xi Chen
For your love.

ACKNOWLEDGMENT

I am grateful to Dr. Alexei Khalizov for his guidance, everlasting patience, constant support, and encouragement as my dissertation advisor. Besides being an outstanding advisor, he is a friend who encouraged and allowed me to grow as an independent researcher through this Ph.D. journey.

I would also like to thank my committee members: Dr. Hao Chen, Dr. Farnaz A Shakib, Dr. Yuanwei Zhang, and Dr. Yuan Gao, for spending their time and sharing their expertise on completing my Ph.D.

I am grateful to the Department of Chemistry and Environmental Science for supporting me as a teaching assistant and the National Science Foundation (NSF) for their research support (grant # AGS-1554777).

I want to express my special thanks to the very diverse group members from the Atmospheric Chemistry Lab. You are amazing graduates and undergraduates. We have shared successes and failures and have been through those never-ending presentation rehearsals and brainstorming meetings. It was also my pleasure to hear life experiences and research opinions from Dr. Chong Qiu and Dr. Ogochukwu Enekwizu. Thank you for sharing research experiences, interviewing tips, and encouragement over numerous chats.

My gratitude goes to my friends at NJIT: Na Liu, Jie Dou, Chunzhao Chen, Fei Li, Zhaoxiong Wan, Qi Wang, Chen Wu, and Pham Dung. Thank you for being friends of mine and encouraging me to finish this journey. I would especially like to thank my roommates: Ruqi Pei and Hongling Deng. Thank you for sharing numerous dinners (Hot Pot and Toasted Fish) with me and caring for me during the COVID-19 time. I am especially thankful to my sister, Xinqian Li, and my old friend, Junyao Gu, for encouraging me to pursue a better life and for their surprise visits.

Finally, sincerely thank the Mao's family for their unconditional love and constant support, motivating me to pursue my dreams, cheering me up when I felt sad, and taking care of me when I had hard times to inspire me to be the best I can be. I hope that your lovely granddaughter/daughter/sister makes you all proud of me and always.

TABLE OF CONTENTS

TABLE OF CONTENTS
(Continued)

Chapter **Page**

TABLE OF CONTENTS
(Continued)

TABLE OF CONTENTS
(Continued)

LIST OF TABLES

LIST OF FIGURES

LIST OF FIGURES
(Continued)

LIST OF FIGURES
(Continued)

LIST OF FIGURES
(Continued)

LIST OF FIGURES
(Continued)

LIST OF FIGURES
(Continued)

Figure **Page**

LIST OF FIGURES
(Continued)

LIST OF FIGURES
(Continued)

LIST OF FIGURES
(Continued)

CHAPTER 1

INTRODUCTION

1.1 Background

1.1.1 Mercury Cycling in the Environment

Mercury is an environmental pollutant of global concern that has high toxicity to a broad range of living organisms, exacerbated by its strong ability to bioaccumulate (Rice et al., 2014). It is released primarily in elemental state (Hg^0), entering the atmosphere as gaseous elemental mercury (GEM) (Obrist et al., 2018). Atmospheric GEM is involved in long-range transport and oxidative transformations due to its relatively long lifetime, which is about a year (Lin et al., 1999; Schroeder et al., 1998b), producing gaseous oxidized mercury (GOM) and particle-bound mercury (PBM) (Lyman et al., 2020a). All forms of mercury can be transferred to oceanic and terrestrial environments (as shown in Figure 1.1). GEM has been shown to exchange dynamically with plant stomata and soils (Naharro et al., 2019; Obrist et al., 2017; Rutter et al., 2011; Stamenkovic et al., 2009), whereas GOM and PBM undergo both wet and dry deposition (Sather et al., 2013; Wright et al., 2016; Zhou et al., 2018). Although the oxidized mercury typically represents less than 5% of the total atmospheric mercury, due to the high solubility it is the primary contributor to the mercury deposition to land and oceans (Lindberg et al., 2007).

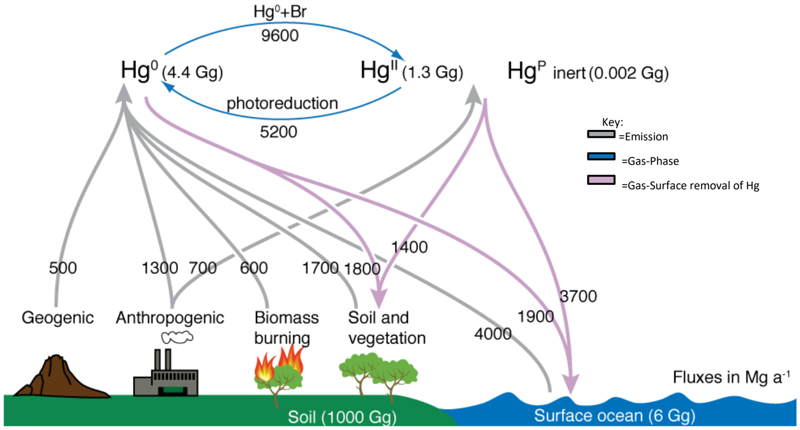

Figure 1.1 The global atmospheric budget for mercury derived from the GEOS-Chem model.
Source: (Holmes et al., 2010).

1.1.2 Oxidation of Atmospheric Mercury

The concentration of mercury in precipitation (1 to 50 ng/L) is several orders of magnitude higher than the predicted using GEM concentration by Henry's law. Thus, GEM must be oxidized either within aqueous aerosol or in the gas phase then adsorbed to RM (RM=GOM + PBM), which is more reactive and soluble in water compared with GEM. In early studies (Hall, 1995), it was assumed that the largest GEM loss occurred in the presence of O_3 with a gas phase rate constant of 3×10^{-20} cm^3 $molecule^{-1}$ s^{-1} at 20 °C is primarily responsible for the atmospheric lifetime of GEM,

$$Hg^0 + O_3 \rightarrow HgO + O_2 \tag{1.1}$$

which is too slow to explain the rapid depletions of mercury in the Arctic atmospheric boundary layer at springtime (Schroeder et al., 1998a) and in the Antarctic (Ebinghaus et al., 2002).

There has been increasing evidence that chemical reactions of halogens are involved in the elemental mercury depletions (Lindberg et al., 2002). Both laboratory and computational studies have focused on the gas phase oxidations of GEM by molecular and atomic halogens, halogen oxides, nitrate radical, and hydroxyl radical (Calvert et al., 2003; Impey et al., 1997; Sommar et al., 1997). However, the oxidations of GEM by all other chemicals except bromine radical were disputed by subsequent studies (Calvert et al., 2005; Sommar et al., 2001). The oxidation of GEM by atomic bromine is sufficiently fast ($k_{\mathrm{Hg+Br}} = 3\times10^{-12}$ cm^3 molecule^{-1} s^{-1}), and the concentration of Br present in the troposphere is sufficiently high, these could explain the Arctic depletion events (Ariya et al., 2002) as following,

$$\mathrm{Hg^0 + Br + M \rightarrow HgBr + M} \tag{1.2}$$

where M is the third body to help to remove extra energy in the reaction. The bromine radical is formed by oxidation and photolysis of short-lived bromocarbons and from debromination of sea-salt aerosol, transport from the stratosphere, and recycling from reservoir species by homogeneous and heterogeneous processes (Parrella et al., 2012). This reaction dominates the oxidation although the reaction has shown a lower reaction rate constant ($k_{\mathrm{Hg+Br}} = 0.3\times10^{-12}$ to 1.0×10^{-12} cm^3 molecule^{-1} s^{-1}) in subsequent studies (Donohoue et al., 2006; Khalizov et al., 2003). Quantum chemicals studies (Jiao et al., 2015, 2017a; Lam et al., 2019b; Shah et al., 2021) have pointed out that HgBr radical tends to react with NO_2 and HO_2 radicals (Equation 1.3), and O_3 (Equation 1.4) to form the most probable GOM species, such as BrHgONO and BrHgOOH, and BrHgOH (Equation 1.5).

$$\mathrm{HgBr} + \mathrm{X} \rightarrow \mathrm{HgBrX}\ \ (\mathrm{X} = \mathrm{NO_2}, \mathrm{HO_2}) \tag{1.3}$$

$$\mathrm{HgBr} + \mathrm{O_3} \rightarrow \mathrm{HgBrO}\ +\ \mathrm{O_2} \tag{1.4}$$

$$\mathrm{HgBrO} + \mathrm{RH} \rightarrow \mathrm{HgBrOH}\ +\ \mathrm{R} \tag{1.5}$$

However, the theoretical studies (Saiz-Lopez et al., 2018; Saiz-Lopez et al., 2020) have shown that BrHgONO and BrHgOOH are rapidly photolyzed. Wu et al have confirmed the existence of a reduction channel in the formation of BrHgONO using their experimental kinetic studies of HgBr radical with NO_2 (Wu et al., 2020). An improved GEOS-Chem global atmospheric mercury chemistry model includes the reduction and oxidation pathways of BrHg when reacting at the Br and the Hg, respectively, in its reaction with ozone (Shah et al., 2021). Later, a kinetic study of HgBr radical with O_3 was reported, indicating its dominating role on the gas-phase oxidation of Hg(I) to Hg(II) (Equation 1.4); meanwhile, Hg(II) was reduced through the reduction channel of BrHgO with O_3 (Equation 1.5) (Wu et al., 2021).

1.1.3 Interaction of Gaseous Oxidized Mercury with Surfaces

The lifetime of atmospheric mercury is estimated to range from a few months to a year, giving rise to its global transport, reaching even the remote oceans (Holmes et al., 2010; Selin et al., 2007). Some of the mercury can deposit from the atmosphere as GEM, via the direct exchange with plant stomata and soils (Naharro et al., 2019; Obrist et al., 2017; Rutter et al., 2011; Stamenkovic & Gustin, 2009). However, a significant fraction of GEM is converted to GOM, or gaseous Hg(II), through a process of photochemical oxidation (Ariya et al., 2002; Donohoue et al., 2006; Holmes et al., 2010; Jiao & Dibble, 2015). The evaluation of the GOM and PBM deposition is severely hindered by the inadequate knowledge of their chemical identities, which in the absence of solid experimental evidence are deduced based on the chemical intuition and quantum chemical calculations (Dibble et al., 2012; Jiao & Dibble, 2015; Jiao et al., 2017b; Lindqvist et al., 1985).

Quantum chemical calculations suggest that BrHgONO, $BrHgONO_2$, BrHgOOH, and BrHgOH are among the most abundant oxidation products of GEM (Dibble et al., 2012; Jiao & Dibble, 2015, 2017b; Lam et al., 2019b). Being less volatile and more water-soluble than elemental mercury, GOM can engage in several competing pathways that together control the overall rate of atmospheric mercury removal through deposition to the Earth's surface. For instance, some of the GOM is taken up by atmospheric waters, depositing through precipitation (Zhou et al., 2018), or it can undergo dry deposition to terrestrial and aquatic surfaces (Sather et al., 2013; Wright et al., 2016). Modeling studies show that dry deposition alone is too slow to account for the rapid decrease in GOM concentration in the afternoon and evening hours; hence, uptake of GOM by sea salt aerosols often has to be included as an additional loss pathway in marine environments (Holmes et al., 2009; Selin et al., 2007). The uptake of GOM by aerosol particles produces so-called particulate-bound mercury (PBM), which can undergo wet and dry deposition (Sather et al., 2013; Wright et al., 2016; Zhou et al., 2018).

Computational studies report that adsorption of Hg(II) on dry surfaces reduces the amount of energy required to generate Hg(0) (Tacey et al., 2018a; Tacey et al., 2016), while laboratory and field studies confirm that Hg(II) can be promptly reduced upon solar light irradiation on both dry and wet aerosols (Deng et al., 2019; Tong et al., 2013). Thus, the knowledge of GOM transfer to cloud droplets and aerosol particles is important for an accurate evaluation of atmospheric mercury cycling.

The scavenging of GOM by water droplets is described by Henry's law in most modeling studies (Amos et al., 2012; Ye et al., 2016), but there is no uniform treatment of the GOM conversion to PBM. For instance, three studies utilizing the same global 3-D chemical transport model GEOS-Chem made three different assumptions: no GOM-to-PBM partitioning (Selin et al., 2008), a 50/50 partitioning (Holmes et al., 2010), or partitioning according to an empirically derived temperature-dependent distribution coefficient (Amos et al., 2012). Furthermore, the scavenging of GOM by sea salt is treated separately from other aerosols, typically as a first-order sink with an empirically derived rate coefficient (Selin et al., 2007). In a more advanced approach (Holmes et al., 2010), the rate coefficient is parameterized based on the results from a box model, where the uptake of GOM is limited by mass-transport at the gas-particle interface, assuming a constant mass uptake coefficient of 0.5 (Holmes et al., 2009). However, the latter value might be significantly lower, varying with the composition and concentration of chemical species in the condensed phase, and that may produce a significant uncertainty in the uptake by fine aerosol particles, where mass accommodation rather than gas diffusion is the limiting step of uptake (Davidovits et al., 2011).

The knowledge of GOM interaction with aerosol surfaces remains rather limited at present, with the majority of quantitative information pertaining to equilibrium partitioning, but not kinetics. For instance, particles made of sodium nitrate, potassium chloride, and sodium chloride were found to show high partitioning coefficients for Hg(II), while ammonium sulfate, levoglucosan, and adipic acid caused Hg(II) to partition toward the gas phase (Rutter et al., 2007). Quantum-chemical calculations have been successfully applied to estimate partitioning coefficients for $HgCl_2$ on iron oxide and sodium chloride surfaces, showing general agreement with the experimental measurements (Tacey et al., 2018b). On the other hand, the information on the uptake kinetics is mostly semi-quantitative, such as in the study by Malcolm et al. (2009), who have demonstrated that ambient GOM and laboratory $HgCl_2$ have a comparable affinity for KCl, NaCl, and sea salt, and are therefore likely to be scavenged by sea salt aerosols. However, the rate of uptake in these adsorption experiments, performed with coated denuders in the air at atmospheric pressure, was limited by gas diffusion and hence did not allow for the retrieval of any quantitative information about the reactive uptake.

1.1.4 Model of Gas-Surface Chemistry

Current understanding of the interaction between aerosol particles and trace gases is illustrated schematically in Figure 1.2a. The entire process comprises several steps: (a) gas molecules diffuse towards the particle surface; (b) gas molecules experience surface adsorption, desorption, and/or surface reaction; and (c) if the particle is liquid, the molecules can become solvated, entering the liquid phase, where they are subject to diffusion and/or reaction.

Overall, gas-surface reactions are represented as a first-order kinetic process: a gas molecule A reacts on the surface to form B with rate constant k,

$$\mathrm{A} \xrightarrow{\text{surface}} \mathrm{B} \tag{1.6}$$

where k is the rate constant of the overall gas-surface reaction that depends on the uptake coefficient (γ), mean thermal velocity of the reacting gas molecules ($\bar{c}$); and aerosol surface area (n_s),

$$k = \frac{\gamma \bar{c} n_s}{4} \tag{1.7}$$

the uptake coefficient, also called reaction probability, is defined as the ratio of the number of trace gas molecules removed from the gas phase (net loss) to the total number of trace-gas molecule collisions with the surface,

$$\gamma = \frac{number\ of\ molecules\ lost\ on\ the\ surface}{total\ number\ of\ collisions} \tag{1.8}$$

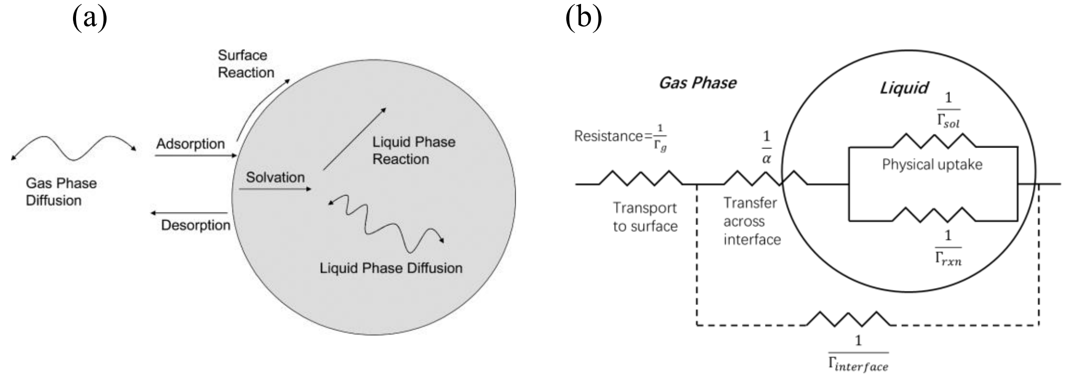

Figure 1.2 Interaction of gas molecules with aerosol particles: (a) multi-step model of gas-particle chemistry and (b) resistance model.
Source for (a): (Davidovits et al., 2006).

The interaction of gas molecules with aerosol particles (Figure 1.2a) can be described by differential equations, which are commonly solved numerically. However, the differential equations are too complex to solve. To simplify the solving processes, individual resistances similar to a resistor in an electrical circuit are applied (as shown in Figure 1.2b). The resistance model is demonstrated in Equation (1.9), $\frac{1}{\gamma}$ is the total resistance, which is represented by the sum of individual resistances:

$$\frac{1}{\gamma} = \frac{1}{\Gamma_g} + \frac{1}{\alpha} + \frac{1}{\Gamma_{rxn} + \Gamma_{sol}} \qquad (1.9)$$

where Γ_g represents the gas transport to the surface of the particles, α is the mass accommodation coefficient for transfer across the interface, Γ_{rxn} represents the bulk liquid-phase reaction, and Γ_{sol} represents solubilization and diffusion in the liquid phase. The rate constant (k) can be estimated based on uptake coefficient obtained from Equation (1.9).

1.1.5 Reduction of Atmospheric Mercury

In addition to atmospheric mercury removal by wet and dry deposition, atmospheric GOM and PBM can be reduced back to GEM (Edgerton et al., 2006; Landis et al., 2014). Models predict that reduction is nearly comparable to or faster than deposition, and hence the competition between these two processes may control the global patterns of mercury entering the terrestrial and aquatic environments (Francés-Monerris et al., 2020; Holmes et al., 2010; Horowitz et al., 2017; Saiz-Lopez et al., 2018). The reduction mechanism is thought to be photochemical, but there is a lack of agreement on whether gaseous or condensed-phase Hg(II) is the principal form which is reduced (Horowitz et al., 2017; Lam et al., 2019b; Saiz-Lopez et al., 2018). The gas-phase photoreduction of Hg(II) has recently been shown to change mercury cycling significantly in the atmosphere and its deposition to the Earth's surface (Saiz-Lopez et al., 2018). Recently, the reduction reaction of BrHgO with O_3 has been verified as the major reduction reaction for Hg(II) (Wu et al., 2021). Photoreduction of Hg(II) to Hg(0) by organic matter in an aqueous system takes place largely through photolysis of aqueous Hg(II)–organic complexes (Shah et al 2021, O'Driscoll et al, 2004, Whalin et al, 2007).

1.1.6 Detection of Atmospheric Mercury

The quantification of atmospheric mercury is a substantial analytical accomplishment because of the challenge associated with the low atmospheric mercury concentrations, ranging from tens of pg m^{-3} (GOM and PBM) to few ng m^{-3} (GEM). Due to the challenge, most existing detection methods must rely on some form of chemical or physical trapping to increase the sample concentration (Gustin et al., 2015; Pandey et al., 2011). For instance, GEM is trapped as an amalgam on gold-coated surfaces, then thermally desorbed and detected by atomic absorption or atomic fluorescence spectroscopy. GOM is often pre-concentrated on a KCl-coated denuder, then thermally decomposed and detected as GEM (Landis et al., 2002). Although these methods are widely commercialized, significant measurement biases have been discovered over the last decade, including the interferences from ozone and water vapor in the KCl denuder method for GOM (Gustin et al., 2013; Lyman et al., 2010) and the passivation of gold surface during GEM analysis (Landis et al., 2002). The interferences vary significantly with environmental conditions, calling into question the large set of GOM data collected and hence the current scientific understanding of the atmospheric mercury chemistry and dynamics (Jaffe et al., 2014).

In response to the call to improve the knowledge of the chemical speciation of GOM (Jaffe et al., 2014), active work is conducted by several groups to develop alternative analysis methods. The methods differ in the types of adsorbing media and analysis methods, but all of them involve a two-step scheme, where in the first step GOM is pre-concentrated and in the second step it is thermally desorbed and analyzed. For instance, GOM from ambient air can be collected on nylon membranes or quartz wool and then desorbed in a programmed temperature sequence, where it is pyrolyzed and analyzed as GEM (Ernest et al., 2014; Gustin et al., 2016; Huang et al., 2013). A series of peaks appearing at different temperatures are identified by comparing them against mercury (II) standards that are loaded onto membranes and analyzed under identical conditions. This approach is sufficiently sensitive to be deployed in the field, but the chemical speciation it produces is rather indirect and requires the use of authentic standards. To improve chemical speciation, Jones et al. (2016) substituted chemical analysis of the evolving GOM for pyrolysis. In their method, GOM from a sample collector is thermally desorbed, focused on a capillary column head with a cryogenic pre-concentrator, separated in a gas chromatograph, and then analyzed with an electron impact ionization mass spectrometer (GC-MS). With sufficient collection time, mercury (II) halides could be analyzed with a limit of detection low enough to be used for ambient sampling, but improvements in the collection device were needed to make the approach field worthy. Similarly, (Deeds et al., 2015) used commercial atmospheric pressure chemical ionization mass spectrometer (APCI-MS) interfaced to a custom-made collector to detect $HgCl_2$ and $HgBr_2$ by pre-concentration and thermal desorption, with detection limit comparable to other methods for the measurement of total GOM. However, air matrix interfered with the identification of $HgCl_2$ and $HgBr_2$ in ambient air samples.

All of the methods outlined above rely on the sample pre-concentration, which is a double-edged sword. On the one hand, pre-concentration allows the collection of sufficient sample mass making chemical analysis possible. On the other hand, it can produce artifacts in the case of stable species and it prohibits the analysis of labile species (e.g., free radicals), making those methods unsuitable in kinetic studies. The question of possible artifacts is an important one, as no validation has yet been presented that GOM molecules adsorbed on the surface can be desorbed in the same chemical form they had when in the air. Based on what we know of molecular structure from quantum chemicals studies (Jiao & Dibble, 2015, 2017b; Lam et al., 2019a), the most probable GOM species, such as BrHgONO, $BrHgONO_2$, BrHgOH, and BrHgOOH, do not appear to be particularly volatile or thermally stable. Furthermore, once on the surface, these species may engage in exchange reactions with each other (Ammlung et al., 1974; Spiro et al., 1961) or with other more abundant chemicals, such as HCl, adsorbed to the surface from the air. These exchange reactions on surfaces may potentially convert the original low-volatility chemicals, such as BrHgONO, to volatile mercury-containing products, like HgClBr, which can be thermally desorbed and will interfere with molecular analysis of GOM. For instance, BrHgCl observed in the mass spectra of adsorbed and then desorbed $HgCl_2$ is thought to have been produced in an exchange reaction with $HgBr_2$ present as a residue on the surface (Jones et al., 2016).

A way to avoid artifacts stemming from sample pre-concentration is by excluding that step entirely and using direct analysis instead. With direct analysis, a limit of detection (LOD) for GOM in the range of parts per billion by volume (ppbv) is relatively simple to achieve, opening an opportunity to conduct kinetic and mechanistic experiments in laboratory, like it has been done with GEM (Donohoue et al., 2006; Donohoue et al., 2005). For instance, Tong et al. (1999) have reported direct analysis of $HgBr_2$ by photo-fragment fluorescence spectroscopy, where the molecule was photolyzed with a 222 nm laser and fluorescence from the excited mercury atom was measured at 253.7 nm. The LOD of 1 ppbv makes this method appropriate for laboratory studies of mercury chemistry, but the analysis can only be carried out in an inert atmosphere (e.g., argon) due to Hg* ($^3P_1$) quenching by molecular oxygen. Furthermore, because of the relatively broad UV absorption peaks (Francés-Monerris et al., 2020; Maya, 1977; Saiz-Lopez et al., 2018), the capability to distinguish between different mercury-containing molecules is limited. The use of this method for ambient GOM is less straightforward because the LOD would have to be in the lower sub part per trillion (pptv) range.

1.2 Ion Drift-Chemical Ionization Mass Spectrometry

The sensitivity and chemical identification issues can be overcome using mass spectrometry, or more specifically chemical ionization mass spectrometry (CIMS) with multistage ionization, where the region of reagent ion generation is separated from the region of neutral analyte ionization (Huey, 2007; Knop et al., 1985). In CIMS, the reagent ion produced externally by electric discharge or radioactive source from precursor chemical is injected into the sampled airflow and allowed to react with neutral analyte for a specific time. By design, metastable and radical species formed in the ionization region are prevented from interfering with ion-molecule chemistry, and the reagent ion can be flexibly chosen to detect specific trace chemicals with high selectivity (Viggiano, 1993). CIMS has been widely applied to atmospheric trace gases measurements. CIMS could be modified to proton transfer reaction-mass spectrometry (PTR-MS) and ion-drift chemical ionization mass spectrometry (ID-CIMS). For instance, the detection of volatile organic compounds (VOCs) (Lindinger et al., 1998) and nitric acid (Huey, 2007) using PTR-MS and ID-CIMS, respectively. CIMS can be adapted to the ambient detection of ammonia and amines (Hanson et al., 2011), VOCs (Jordan et al., 2009) using atmospheric pressure chemical ionization-mass spectrometry (APCI-MS). Using chemical ionization at atmospheric pressure (AP), ultrahigh sensitivity can also be achieved, with notable examples being the detection of atmospheric sulfuric acid, methanesulfonic acid, and hydroxyl radical (Eisele et al., 1991, 1993; Mount et al., 1992). For a 5-min integration time in AP-CIMS, a LOD of 7×10^4 molecule cm^{-3} has been reported, while increasing the integration time to 60 min allowed to improve the detection down to 2×10^4 molecule cm^{-3} (Eisele & Tanner, 1991; Mount & Eisele, 1992). Additionally, a CIMS instrument can be equipped with an Ion Drift (ID) tube to improve control of ion-molecule reaction time and ion clustering, resulting in an ID-CIMS (Fortner et al., 2004; Zheng et al., 2010). For instance, PTR-MS utilizes H_3O^+ as a reagent ion and uses the electric field in the ion drift tube to minimize H_3O^+ clustering with water molecules (Lindinger et al., 1998). With a fast response time and a low detection limit, this technique has been applied extensively for the detection of many important volatile organic compounds with proton affinities higher than that of water (de Gouw et al., 2003).

Using quantum chemical calculations, Dibble et al. (2014) have evaluated the applicability of PTR-MS towards the detection of GOM. The study investigated the protonation of HgX_2 (X = Cl, Br, and I) and BrHgY (Y = NO_2, ClO, BrO, HOO) in reactions with H_3O^+, showing that stable protonated products could be formed with HgI_2 and with most of BrHgY, but not with $HgBr_2$ and $HgCl_2$ due to their low proton affinity. In principle, PTR-MS can be used for the detection of GOM in laboratory settings, but to achieve the required LOD for atmospheric detection, the drift tube would have to operate at atmospheric pressure to increase the ion-molecule reaction time and decrease sample dilution (Hanson et al., 2011). At atmospheric pressure, H_3O^+ is converted to hydrates $H_3O^+(H_2O)_n$, which have significantly lower reactivities than H_3O^+, rendering most if not all Hg-containing species non-detectable. De-clustering of $H_3O^+(H_2O)_n$ is possible, but it would require the use of prohibitively high drift tube voltage and temperature, which are not technically feasible.

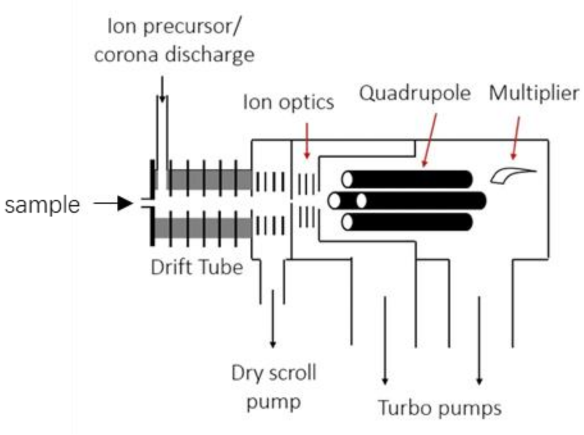

Figure 1.3 Ion drift - chemical ionization mass spectrometer.

ID-CIMS allows qualitative detection of chemicals and quantitative investigation of their ion-molecule chemistry. The instrument consists of an ion source, an ion drift tube, and a quadrupole mass analyzer (Figure 1.3). The sample can come from either ambient air or a chemical reactor. In the common mass spectrometry technique, ion generation and ion-molecule reactions happen in the same region, making more noise in the background. ID-CIMS takes advantage of separating the reagent ion generation by corona discharge and ion-molecule reactions in the drift tube as it reduces the signal background. Reagent ions

(R) are generated from precursors in corona discharge, which is used as the ion source. Positive or negative reagent ions ($R^{+/-}$) can react with analyte molecules or radicals (X) inside the ion drift tube to form product ions,

$$X \ + R^{+/-} \rightarrow X^{+/-} + R \tag{1.10}$$

the drift tube allows precise control of the residence time and better ionization efficiency due to constrained ion trajectories and velocities. Based on the ratio of the product-ion to reagent-ion ($I_{product\ ion}/I_{reagent\ ion}$) together with the residence time (t) and ion-molecule rate constant (k'), the gas phase concentrations of the product can be calculated (Equation 1.11),

$$[\mathrm{C}] = \frac{I_{product\ ion}}{I_{reagent\ ion}} \frac{1}{k' \times t} \tag{1.11}$$

the residence time (t) in the drift tube is determined by the gas flow rate, electric field, pressure, and ion mobility. Thus, quantitative concentration measurement can be done by ID-CIMS in the absence of calibration with authentic standards (Fortner et al., 2004) because it only requires $I_{product\ ion}/I_{reagent\ ion}$, k', and t (see Equation 1.11). To conclude, ID-CIMS is a substantial solution for the experimental studies of atmospheric oxidized mercury, and the ultimate goal is to find appropriate reagent ions for the oxidized mercury detection.

1.3 Research Objectives

To elucidate the atmospheric mercury chemistry, which includes kinetics, mechanism, and detection of GOM in the atmosphere, this proposal has four major objectives: (1) Explore a direct detection of GOM by chemical ionization mass spectrometry (CIMS) to enable further investigations on heterogeneous reactions, gas phase oxidations, and field measurements. (2) Investigate heterogeneous uptake of GOM on surfaces to improve understanding of the gas-surface processes that form PBM. (3) Explore the exchange reactions of GOM species on surfaces to help understanding artifacts during detection pre-concentration. (4) Elucidate the kinetics and mechanism of gas-phase reactions of HgBr, the principal intermediate in the oxidation of GEM in order to evaluate the lifetime of GEM and molecular speciation of GOM. Figure 1.4 shows the project overview.

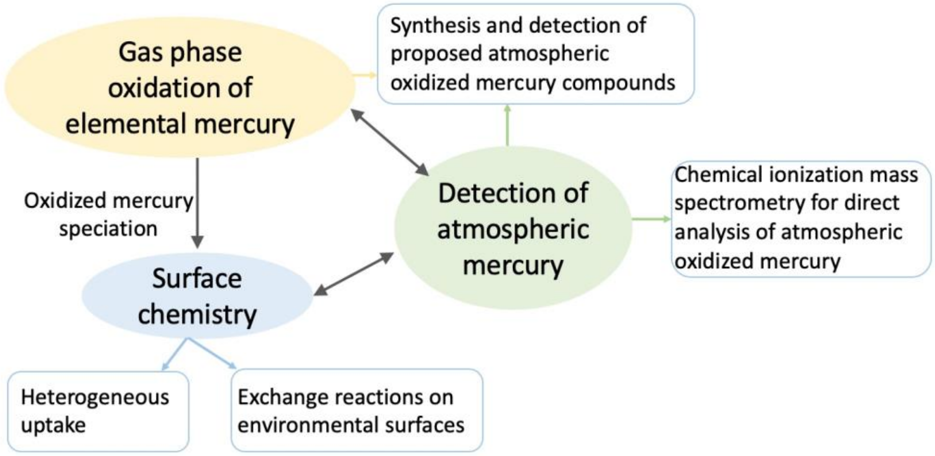

Figure 1.4 Overview of the study of the atmospheric mercury chemistry.

Task 1: Detection of atmospheric oxidized mercury. Investigate ion-molecule reactions for the oxidized mercury detection to understand its molecular speciation, explore the detection of simple GOM ($HgCl_2$ and $HgBr_2$) by ID-CIMS, and improve the sensitivity of ID-CIMS by several orders of magnitude.

Task 2: Uptake of oxidized mercury by environmental surfaces. The removal of GOM surrogates ($HgCl_2$ and $HgBr_2$) on different surfaces which are made by inorganic and organic materials. The reaction probabilities are determined to compare the reactivities of GOM on different surfaces, which will help to understand the mechanism rate of GOM transformation to form PBM.

Task 3: Exchange reactions of oxidized mercury on surfaces. A series of exchange reactions between: 1) different GOM species, 2) GOM and other chemicals which typically exist on current GOM collecting material (KCl coated denuder surface, HCl absorbed on the Nylon, cation exchange membrane surfaces) are performed to understand surface chemistry of mercury. Consists of **a.** explore exchange reactions of GOM in aqueous phase and on the surface. The molecular speciation will be determined by appropriate ionization reaction for GOM; **b.** investigate thermal decomposition of GOM on the membranes that will help to understand bias in current detection method during sample collection.

Task 4: Gas phase oxidation of elemental mercury. The kinetics and mechanism of elemental mercury gas phase oxidation are studied in the following: **a.** elemental mercury reacts with bromine radical to form HgBr radical; and **b.** generate and detect HgBrONO, HgBrOOH in the gas phase by reacting HgBr radical with atmospherically relevant chemicals (NO_2, HO_2).

CHAPTER 2

EXPLORATION OF ION-MOLECULE CHEMISTRY FOR DIRECT ANALYSIS OF GASEOUS MERCURY SPECIES BY CHEMICAL IONIZATION MASS SPECTROMETRY

2.1 Introduction

The development and application of methods for operational and molecular speciation is described in several detailed reviews (Gustin et al., 2015; Gustin et al., 2021a; Huang et al., 2014; Lyman et al., 2020b; Pandey et al., 2011), so in the following we will outline only the major differences between those methods, along with reported analysis interferences.

The early methods for GOM and RM analysis relied on mist chambers (Stratton et al., 1995), and already in those early studies, researchers raised concerns about possible interferences caused by the presence of ozone and aerosols in ambient air (Lindberg et al., 1998; Stratton & Lindberg, 1995). In addition to these wet methods, various types of filters (e.g., Teflon and quartz), plugs (e.g., quartz wool), and membranes (e.g., ion exchange) were introduced, where the collected GOM was either extracted by digestion as Hg^{2+} or thermally desorbed as GEM for subsequent analysis (Ebinghaus et al., 1999; Munthe et al., 2001). A somewhat different approach relied on tubular and annular denuders coated with gold (Xiao et al., 1991) or KCl (Feng et al., 2000), where the quantification of GOM was performed by extraction or thermal desorption. Later, a repeated collection-desorption cycling of the annual denuder was introduced for use in an automated system commercialized by Tekran (Landis et al., 2002), where GOM collected in a KCl annular denuder is thermally desorbed, pyrolysed into GEM, which is trapped on gold-coated sand, and desorbed and analyzed by cold vapor atomic fluorescence spectroscopy (CVAFS).

Although the Tekran system has found a broad use in research and regulatory monitoring, there have been a number of concerns raised, including the undersampling of GOM under certain conditions (Brosset et al., 1995) and a frequent lack of closure for the atmospheric mercury mass balance based on all measured forms (Choi et al., 2013; Swartzendruber et al., 2009). Further systematic studies have revealed that elevated ozone and high relative humidity interfere with GOM detection, and it was suggested that GOM on the KCl surface becomes converted into GEM through reactions initiated by ozone (Ambrose et al., 2015; Lyman et al., 2012; McClure et al., 2014). Thus, subsequent efforts were focused on the development of a system that avoids the use of the KCl denuder. For instance, in the Detector for Oxidized Hg Species (DOHGS) (Ambrose et al., 2013), GOM is not collected but measured as a difference between TGM and GEM, using two Tekran modules. The sampled air is split into two flows, where the first flow is passed through a pyrolyser to quantify TGM and the second flow is passed through an RM trap made of quartz wool to remove RM and hence measure only GEM.

Later on, other research groups have modified the DOHGS system for use with a single Tekran module instead of two (Gustin et al., 2019; Lyman et al., 2020c). When further studies discovered that GOM was partially converted to GEM on the quartz wool at an elevated humidity, the wool has been replaced with a cation exchange membrane (CEM) (Ambrose et al., 2013). The high collection efficiency of CEM has been further utilized to develop the Reactive Mercury Active System (RMAS and RMAS 2.0), where RM and GOM are quantified by membrane digestion (Luippold et al., 2020; Lyman et al., 2020c). Also, to distinguish GOM from RM, a PTFE filter was added before the membrane to remove PBM (Gustin et al., 2021b). In principle, the CEM could be analyzed not only by digestion, but also by thermal denuding. However, heating leads to membrane decomposition that interferes with subsequent CVAFS quantification (Lyman et al., 2020c).

All the methods above are associated with pre-concentration and collecting materials, which may scramble the detection. As I mentioned in Section 1.2, a direct analysis method is such needed for GOM detection. Here I demonstrate the development of a direct approach for laboratory detection of GOM, using the ion drift-chemical ionization mass spectrometry (ID-CIMS).

2.2 Selection of Reagent Ions

An ideal reagent ion must meet several requirements. First and foremost, its reaction with GOM must be spontaneous and generate a single (or only a few) product ion(s). This criterion may not always hold for the broadest range of possible GOM and reagent ion combinations. For instance, quantum chemical calculations have shown that H_3O^+ can protonate most oxygen-containing GOM and HgI_2, but not $HgCl_2$ or $HgBr_2$ because of the low proton affinity of the latter (Dibble et al., 2014). Second, clustering of reagent ion with water molecules should not reduce its reactivity significantly. Finally, the reactivity of reagent ion towards other atmospheric trace gases, such as O_3 and NO_2, must be low because their concentrations are many orders of magnitude higher than that of GOM, potentially leading to the reagent ion depletion. Some additional requirements imposed on the reagent ion precursor may include commercial availability, chemical stability, non-corrosiveness, and low toxicity. Obviously, no single reagent ion or its precursor is likely to meet all of these requirements. SF_6^-, CO_3^-, $HNO_3 \cdot NO_3^-$, Cl^-, and CH_3COO^- were selected as reagent ions based on their prior use for the detection of trace gases in laboratory and field studies. Our previous group member, Dr. Francisco J. Guzman conducted calculations of ion affinities with mercury compounds for all reagent ions. Matthew Cooper has conducted qualitative detection studies using three different reagent ions (SF_6^-, CO_3^-, $HNO_3 \cdot NO_3^-$). My goal is (1) to extend the number of reagent ions from three pre-selected to five reagent ions, including Cl^- and CH_3COO^- and (2) to conduct quantitative optimization of conditions for all five reagent ions under both ~2 Torr and near-ambient pressures, includes measurements of sensitivity and limit of detection (LOD).

SF_6^- is a versatile reagent ion widely utilized in laboratory studies, where humidity can be controlled, but it is less appropriate for atmospheric measurements because of the rapid reaction with water (Arnold et al., 2001; Viggiano et al., 2005). In laboratory studies, SF_6^- has been used for the detection of many chemicals, including $ClONO_2$, O_3, NO_2, N_2O_5, and SO_2 (Huey et al., 1995; Viggiano et al., 2005). Depending on the neutral co-reactant, SF_6^- can react via electron transfer (Equation 2.1) or ion transfer (Equation 2.2) mechanisms,

$$O_3 + SF_6^- \rightarrow O_3^- + SF_6 \qquad (2.1)$$

$$HCl + SF_6^- \rightarrow HClF^- + SF_5 \qquad (2.2)$$

often producing multiple products, which are indicative of complex transformation pathways (Arnold & Viggiano, 2001; Huey et al., 1995). As an electron acceptor, SF_6 was used as an additive to isobutane (IB) for the detection of mercury halides using APCI-MS (Deeds et al., 2015). In the case of $HgCl_2$ detection using IB/SF_6, $HgCl_2^-$, $HgCl_3^-$, and

$HgCl_2{\cdot}F^-$were detected, but no ions related to IB, which caught our attention that SF_6 may potentially be used as a reagent ion precursor for the detection of $HgCl_2$ using ID-CIMS, the ion-molecule reaction occurs via either electron transfer (Equation 2.3) or ion transfer (Equation 2.4).

$$HgCl_2 + SF_6^- \rightarrow HgCl_2^- + SF_6 \tag{2.3}$$

$$HgCl_2 + SF_6^- \rightarrow HgCl_2{\cdot}F^- + SF_5 \tag{2.4}$$

The CO_3^- ion often reacts via ion transfer. For instance, it collisionally transfers O^- to SO_2 (Equation 2.5) (Jost et al., 2003; Salcedo et al., 2004) and SO_3 (Arnold et al., 1995), but abstracts H^+ from the acids, such as HCOOH (Equation 2.6) (Viidanoja et al., 1998), CH_3COOH (Viidanoja et al., 1998), H_2SO_4 (Salcedo et al., 2004; Viggiano et al., 1997), and HNO_3 (Arijs et al., 1998). Clustering of CO_3^- with neutral molecules is also possible (Salcedo et al., 2004; Viidanoja et al., 1998). At an elevated relative humidity, CO_3^- and its ion products can cluster with water and this may lead to a decrease in the detection sensitivity in some cases (Salcedo et al., 2004).

$$SO_2 + CO_3^- \rightarrow SO_3^- + CO_2 \tag{2.5}$$

$$HCOOH + CO_3^- \rightarrow HCOO^- + CO_2 + OH \tag{2.6}$$

The $CO_2 \cdot O_2^-$ ion, often present along with CO_3^-, has been used for the detection of various acids, such as HCOOH (Equation 2.7) (Viidanoja et al., 1998), HNO_3 (Amelynck et al., 1994), and CH_3SO_3H (Schoon et al., 2002). Its reaction with acids proceeds by H^+ abstraction and O_2^- transfer. In both cases, the product ion can cluster with a water molecule or the second acid molecule.

$$HCOOH + CO_4^- \rightarrow CO_2 + O_2^- HCOOH \tag{2.7}$$

The nitrate ion NO_3^-, unlike the CO_3^- and $CO_2 \cdot O_2^-$ ions, can deprotonate only strong acids, such as H_2SO_4 (Equation 2.8) (Eisele & Tanner, 1993) and CH_3SO_3H (Schoon et al., 2002), but with weaker acids and other molecules it reacts via clustering. This ion is highly selective towards highly oxidized organic molecules (Ehn et al., 2014; Zhao et al., 2010) and so it has received a wide use for the detection of such molecules in both field and laboratory measurements (Bianchi et al., 2019; Kirkby et al., 2016; Tröstl et al., 2016; Yan et al., 2016). A quantum chemical study has shown that NO_3^- binds to highly oxidized organic molecules through hydrogen bonds and at least two hydrogen bond donor functional groups are needed for such molecules to be detected by chemical ionization mass spectrometry (Hyttinen et al., 2015). Clustering with water has only a minor impact on the sensitivity when using NO_3^- (Arnold et al., 1995; Viggiano et al., 1997), but to simplify the detection scheme, NO_3^- is often used as clustering with nitric acid, $HNO_3 \cdot NO_3^-$ (Eisele & Tanner, 1993; Zheng et al., 2010).

$$H_2SO_4 + NO_3^- \rightarrow HNO_3 + HSO_4^- \tag{2.8}$$

The chloride ion Cl^- is expected to react via clustering. Cl^- has high selectivity with many organic molecules such as the Criegee intermediate (CH_2OO) (via Equation 2.9) formed during SOA formation (Sakamoto et al., 2013) and the cyclopropyl bromide (Colosimo et al., 1985).

$$CH_2OO + Cl^- \rightarrow CH_2OO{\cdot}Cl^- \tag{2.9}$$

It was reported that Cl^- was used to detect Hg(0) via Equation (2.10), but the spectrum of $HgCl^-$ in this paper did not match its isotope distribution, indicating the spectrum was incorrectly interpreted or there is missing information in the paper (Valadbeigi et al., 2020). However, the reaction of Hg with Cl^- may still happen because the reaction enthalpy is -9.8 kcal/mol. In that paper, Cl^- can also cluster to form Cl_2^- to interfere with the detection using $CHCl_3$ as a reagent ion precursor. We hypothesized that Cl_2^- may not form but only Cl^- if CH_3Cl replaces $CHCl_3$ in the selection of Cl^- precursor so that interferences are reduced.

$$Hg + Cl^- \rightarrow HgCl^- \tag{2.10}$$

Acetate, CH_3COO^-, is used as a reagent ion to selectively detect organic acids, phenols, and hydroperoxides (Veres et al., 2008), or clustering with acetic acid to form $CH_3COOH{\cdot}CH_3COO^-$, used for the detection of a wide range of carbonaceous compounds such as hydroxymethyl hydroperoxide and levoglucosan (Equation 2.11) (Brophy et al., 2016; Inomata et al., 2017; Zhao et al., 2014). The ion-molecule reactions usually occur via clustering (Equation 2.11) and hydrogen abstraction (Equation 2.12). $HgCl_2$ is also expected to react with acetate or acetic-acetate cluster as a Lewis acid.

$$\text{Levoglucosan} + CH_3COO^- \rightarrow \text{Levoglucosan}\cdot CH_3COO^- \tag{2.11}$$

$$RCOOH + CH_3COO^- \rightarrow RCOO^- + CH_3COOH \tag{2.12}$$

2.3 Experimental

Here we used ID-CIMS to investigate ion-molecule reactions of several commonly utilized negative reagent ions (SF_6^-, CO_3^-, $NO_3^-\cdot HNO_3$, Cl^-, and CH_3COO^-) with $HgCl_2$, which served as the GOM surrogate. We performed instrument calibration to determine the sensitivity and LOD of ID-CIMS towards $HgCl_2$ and provide recommendation on how to improve them in future studies. The instrument is shown in Figure 2.1A.

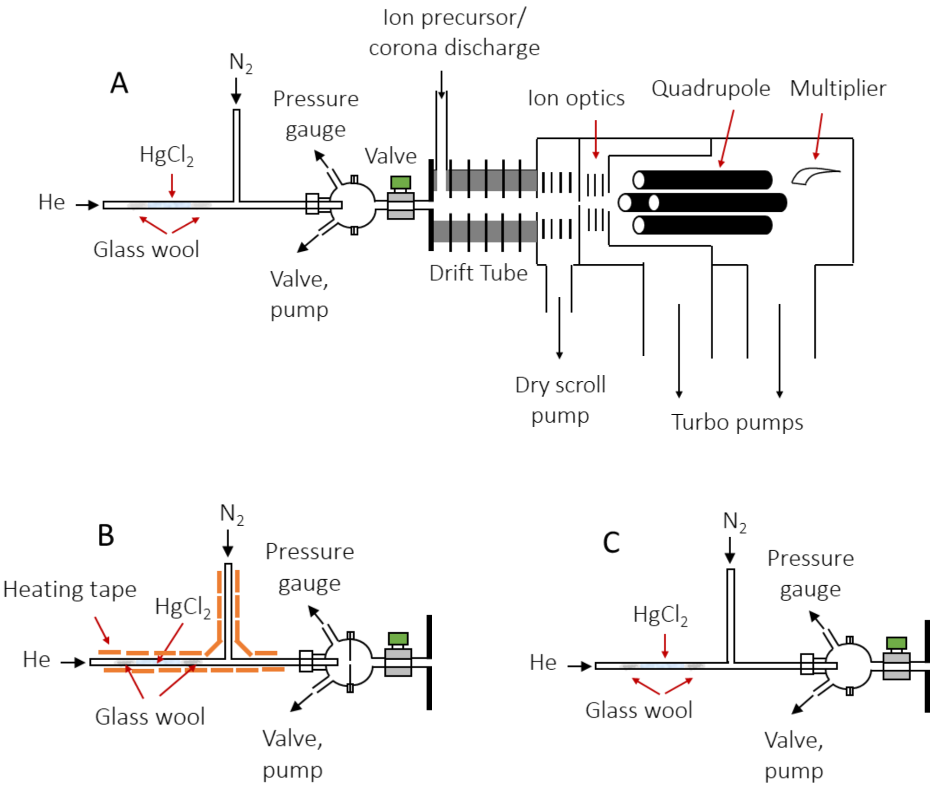

Figure 2.1 Experimental system: (a) ion drift – chemical ionization mass spectrometer; (b) $HgCl_2$ source for low concentration calibration; and (c) $HgCl_2$ source for high concentration calibration.

Three sources for introducing gaseous $HgCl_2$ in a flow of helium were tested: a plug of $HgCl_2$-impregnated fiberglass wool inside a ¼ inch outer diameter (OD) glass tube, a glass impinger with its inner wall coated by a layer of solid $HgCl_2$, and crystalline $HgCl_2$ powder packed between two plugs of deactivated glass wool inside a ¼ inch OD glass tube. The latter source performed the best and was used in all of experiments reported here. The gas-phase concentration of $HgCl_2$ was calculated based on the temperature dependence of the $HgCl_2$ saturation vapor pressure reported by Bernard et al. (1997). Reagent ions were generated by passing a trace amount of an appropriate precursor in a carrier gas through the afterglow of a corona discharge established between a stainless steel needle inside a stainless steel tube (Ferguson et al., 1969; Fortner et al., 2004). The voltage drop across the discharge gap was around 500 V and the electric current was limited by two 2-MΩ resistors, one at each side of discharge.

The SF_6^- reagent ion, along with a small amount of SF_5^- (SF_6^-:SF_5^- = 10:1), was generated from SF_6 in N_2. The CO_3^-, along with small amount of $CO_2 \cdot O_2^-$ was produced from CO_2 in O_2. The $NO_3^-(HNO_3)$ reagent ion, along with small amounts of NO_3^- and $NO_3^-(HNO_3)_2$, was generated from HNO_3 in N_2. The Cl^- was generated from CH_3Cl in N_2. The CH_3COO^- , along with CH_2CO^- (CH_3COO^- CH_2CO^- = 3:1) was generated from acetic anhydride in N_2. The purpose of the drift tube was to control the ion paths, ion clustering, and ion-molecule reaction time. In the presence of a 10-20 V cm^{-1} electric field at a 1.5-2.1 Torr pressure (corresponding to an electric field to number density ratio E/N of 20–29 Td, where 1 Td = 1 Townsend = 10^{17} V cm^2), the ions were constrained to a relatively narrow beam of about 2 mm diameter (Hanson et al., 2003). The collimated ion beam entered the first vacuum chamber through a 0.3 mm pinhole where the majority of neutral gas molecules were pumped away; the beam was then focused using a set of ion optics and introduced to the second chamber, where the ions were detected with a quadrupole mass spectrometer. A typical count rate of the reagent ion signal was 3-5 MHz or Mcps. The chambers were differentially pumped using two Agilent TwisTorr 304 FS turbo pumps (250 L s^{-1} pumping speed). The mass spectrometer was Extrel (19 mm quadrupole, 880 kHz oscillator, 5221 Command System, 2-1000 amu mass range) with a DeTech 402A-H electron multiplier and a counting pre-amplifier (MTS-100, Advanced Research Instruments). All gases were of the Ultra High Purity (UHP) grade as supplied by Airgas. SF_6 was provided as 15% of it in argon by Airgas. Chemicals were of an ACS reagent or better quality and were used as purchased: mercury (II) chloride (31005-100G, Honeywell), chloromethane ($\geq$ 99.5%, Sigma Aldrich), acetic anhydride (99.5%, Sigma Aldrich), and nitric acid (9601-04, Avantor).

2.4 Detection of $HgCl_2$ Using Different Reagent Ions

2.4.1 Detection of $HgCl_2$ Using SF_6^-

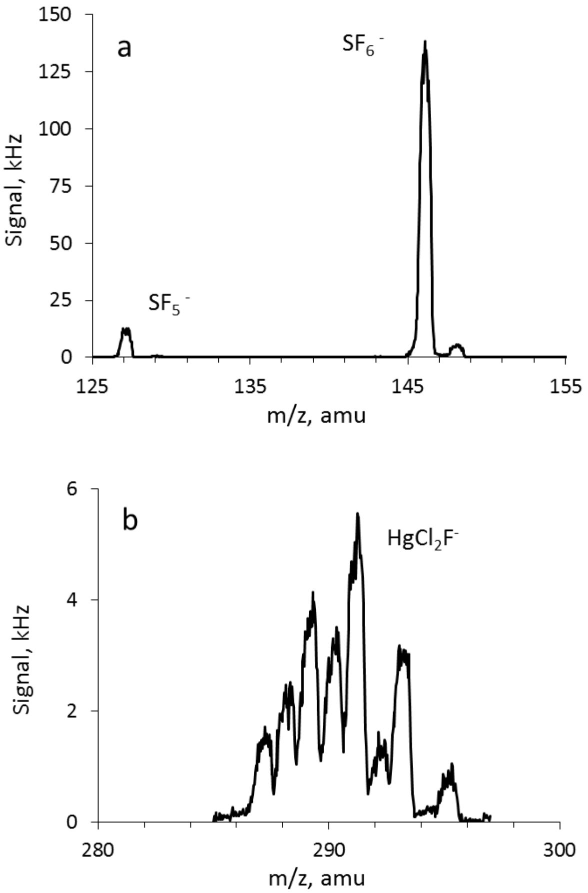

Figure 2.2 Mass spectra of (a) reagent ions generated by sending SF_6 in N_2 through corona discharge and (b) corresponding product ion $HgCl_2F^-$ generated in the presence of $HgCl_2$. The displayed mass spectrum of reagent ions was obtained using a lower electron multiplier voltage to prevent signal saturation.

Figure 2.2a shows reagent ion mass spectrum generated by sending ~200 part per million by volume (ppmv) SF_6 in N_2 through the plasma of the negative corona discharge. The two major peaks at *m/z* 127 and 146 amu correspond to SF_5^- and SF_6^- ions, present in a ratio of 1 to 10. All other peaks were less than 1% of the SF_6^- peak. The SF_6^- signal intensity typically was 3.5-5.7 MHz at a 1900 V electron multiplier voltage, as estimated from the signal of $^{34}SF_6^-$ at *m/z* 148 amu, using the standard isotopic abundances of ^{32}S and ^{34}S. The less abundant isotope was monitored to prevent the signal saturation and also to extend the multiplier lifespan.

Figure 2.2b shows the mass spectrum of the only product ion, which was observed upon the addition of $\sim 2\times10^{10}$ molecule cm^{-3} gas-phase $HgCl_2$ to the ion drift tube. The signal was a multiplet centered at ~290 amu, with the peak intensity of ~5.8 kHz. This multiplet is a superposition of seven Hg isotopes (*m/z* 196, 198–202, and 204 amu) and two Cl isotopes (*m/z* 35 and 37 amu). Based on the unique distribution of peak intensities calculated using the online tool (Manura et al., 1996-2009), we identified this ion product as $HgCl_2{\cdot}F^-$ via Equation (2.4) (Figure 2.3). The scans of the lower and higher *m/z* ranges showed no other significant peaks that could be assigned to the mercury-containing ions. For instance, we detected no peaks corresponding to $HgCl_2^-$ or $HgCl_2{\cdot}SF_6^-$, which could have been produced via electron transfer (Equation 2.3) and ion clustering reactions, respectively. The latter product ion, $HgCl_2{\cdot}SF_6^-$, might be produced but then decomposed in the strong electric field in the drift tube.

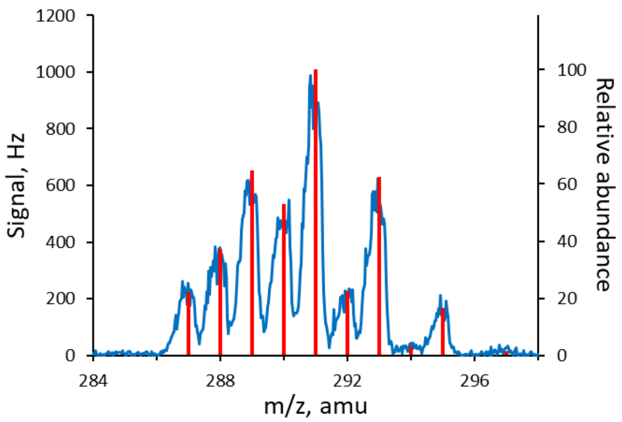

Figure 2.3 Measured and calculated mass spectra of $HgCl_2{\cdot}F^-$. The stick spectrum (red) was calculated using isotope distributions of mercury, chlorine, and fluorine.

2.4.2 Detection of $HgCl_2$ Using CO_3^-

Figure 2.4a shows a mass spectrum obtained in the afterglow of corona discharge, using ~100 ppmv CO_2 in O_2. The major ion observed was CO_3^- (*m/z* 60 amu). Other relatively abundant ions were $CO_2{\cdot}O_2^-$ (76 amu) and HCO_3^- (61 amu). In some cases, small amounts of hydrate $CO_2{\cdot}O_2^-{\cdot}H_2O$ (94 amu) were detected. Due to the contribution of HCO_3^- at *m/z* 61, the theoretical isotopic ratio could not be used to derive the ion signal of CO_3^- at the full electron multiplier voltage. Instead, the experimental ratio of *m/z* 60 over *m/z* 61 at a lower voltage was measured and used for the reagent ion signal estimation.

Several other ions were also present in much smaller quantities, including O^- (16 amu), OH^- (17 amu), O_2^- (32 amu), NO_2^- (46 amu), O_3^- (48 amu), and $O_2^-{\cdot}H_2O$ (50 amu). The first step is the ionization of O_2, producing O^-, O_2^-, O_3^-, and O_4^-, most of which in the presence of CO_2 react rapidly to form CO_3^- and some $CO_2{\cdot}O_2^-$. Once formed, CO_3^- and $CO_2{\cdot}O_2^-$ can both react with the neutral O to generate O_2^- and CO_3^-, respectively. This could explain why there is typically more CO_3^- relative to $CO_2 \cdot O_2^-$. The discharge is also responsible for the generation of NO_2^-, either from N_2 impurity in O_2 or from traces of HNO_3. Similarly, hydrates $O_2^- \cdot H_2O$ and $CO_2 \cdot O_2^- \cdot H_2O$ were formed through the complexation of the residual water vapor with the corresponding bare ions produced in the discharge.

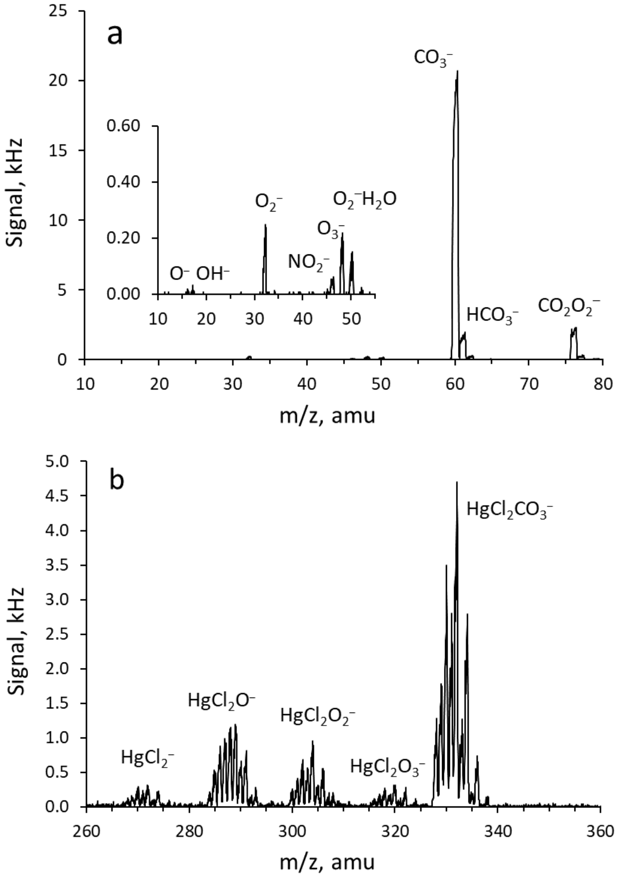

Figure 2.4 Mass spectra of (a) reagent ions generated by corona discharge in CO_2/O_2 and (b) corresponding product ions formed in the presence of $HgCl_2$. The displayed mass spectrum of reagent ions was obtained using a lower electron multiplier voltage to prevent signal saturation.

Figure 2.4b shows that multiple product ions were formed upon introducing $HgCl_2$. The signals were characteristic multiplets with isotope distributions corresponding to

$HgCl_2^-$ (266–278 amu), $HgCl_2{\cdot}O^-$ (282–294 amu), $HgCl_2{\cdot}O_2^-$ (298–310 amu), $HgCl_2{\cdot}O_3^-$ (314–326 amu), and $HgCl_2{\cdot}CO_3^-$ (326–338 amu). The signal of $HgCl_2{\cdot}O_2^-{\cdot}CO_2$ (342–354 amu) was weak and observed only occasionally. The strongest peak was $HgCl_2{\cdot}CO_3^-$, which is formed via clustering of $HgCl_2$ with CO_3^- (Equation 2.13), typically followed by $HgCl_2{\cdot}O^-$ and $HgCl_2{\cdot}O_2^-$, and then by $HgCl_2{\cdot}O_3^-$ and $HgCl_2^-$. Notably, none of the detected product ions was clustered with water, even under conditions when some of reagent ions were hydrated, pointing to the low hydration energies of product ions.

$$HgCl_2 + CO_3^- \rightarrow HgCl_2{\cdot}CO_3^- \qquad (2.13)$$

2.4.3 Detection of $HgCl_2$ Using $NO_3^-{\cdot}HNO_3$

Several reagent ions could be formed in this system, including NO_2^-, NO_3^-, $NO_3^-{\cdot}HNO_3$, and $NO_3^-{\cdot}(HNO_3)_2$ depending on the electric field and nitric acid concentration in the drift tube. In our experiments, conditions were typically adjusted to have $NO_3^-{\cdot}HNO_3$ as the major ion (*m/z* 125 amu), with small amounts of NO_3^- (62 amu) and $NO_3^-{\cdot}(HNO_3)_2$ (188 amu), as shown in Figure 2.5a.

In the presence of an excess HNO_3, the nitrate ion can form $NO_3^-{\cdot}HNO_3$ and then $NO_3^-{\cdot}(HNO_3)_2$. Increasing the HNO_3 concentration drives the formation of larger $NO_3{\cdot}(HNO_3)_n^-$ clusters, where n progressively increases from 0 to 2. On the contrary, increasing the electric field in the drift tube results in the dissociation of clusters, i.e., resulting in a smaller n. In most of our experiments, the electric field was optimized first to improve ion transmission and then the HNO_3 concentration was adjusted to achieve the desired cluster distribution, which is shown in Figure 2.5a.

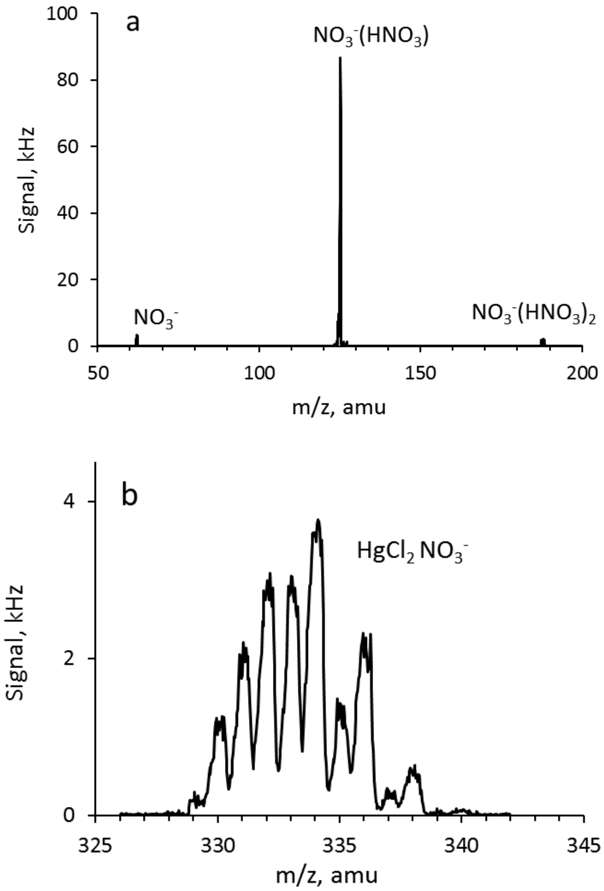

Figure 2.5 Mass spectra of (a) reagent ions generated by corona discharge in HNO_3/N_2 and (b) corresponding product ion formed in the presence of $HgCl_2$. The displayed mass spectrum of reagent ions was obtained using a lower electron multiplier voltage to prevent signal saturation.

According to Figure 2.5b, the only product ion detected using the reagent ion distribution of Figure 2.5a was $HgCl_2 \cdot NO_3^-$ (*m/z* 328–340 amu) via ion transfer of NO_3^- with $HgCl_2$ (Equation 2.14). However, when using a lower concentration of HNO_3 in the drift tube, we also observed $HgCl_2 \cdot NO_2^-$ (312 and 324 amu), which was produced via clustering of $HgCl_2$ with leftover NO_2^- (Equation 2.15).

$$HgCl_2 + NO_3^-{\cdot}HNO_3 \rightarrow HgCl_2{\cdot}NO_3^- + HNO_3 \tag{2.14}$$

$$HgCl_2 + NO_2^-{\cdot} \rightarrow HgCl_2{\cdot}NO_2^- \tag{2.15}$$

2.4.4 Detection of $HgCl_2$ Using Cl^-

The only reagent ion Cl^- (*m/z* 35 amu) was generated (Figure 2.6a) using CH_3Cl/N_2 as reagent gas through corona discharge, providing a much cleaner signal background in the system, not like NO_3^- and CO_3^-. The only product ion, $HgCl_3^-$ (*m/z* 299–317 amu), was detected. Nearly no clusters of Cl^- with other molecules were detected to interfere with the product ion formation with $HgCl_2$. The normalized sensitivity of Cl^- was approximately ten times smaller when compared with the other three reagent ions (SF_6^-, CO_3^-, and $HNO_3{\cdot}NO_3^-$), although it has a cleaner background and less interference from clusters. The details of sensitivities and LOD are provided in section 2.6.

$$HgCl_2 + Cl^- \rightarrow HgCl_3^- \tag{2.16}$$

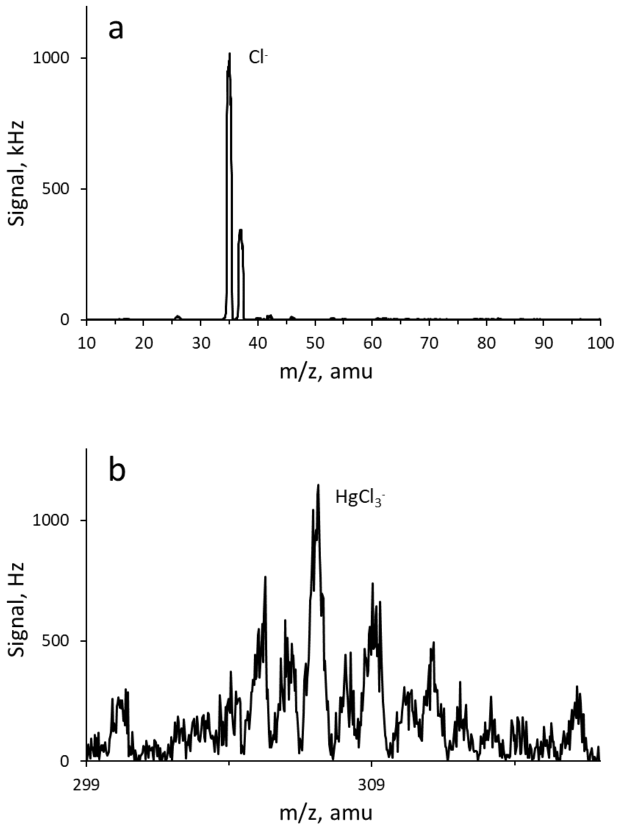

Figure 2.6 Mass spectra of (a) reagent ions generated by corona discharge in CH_3Cl/N_2 and (b) corresponding product ion formed in the presence of $HgCl_2$. The displayed mass spectrum of reagent ions was obtained using a lower electron multiplier voltage to prevent signal saturation.

2.4.5 Detection of $HgCl_2$ Using CH_3COO^-

As shown in Figure 2.7a, only two reagent ions, CH_3COO^- (m/z = 59 amu) and CH_2CO^- (m/z = 42 amu), were produced in corona discharge using acetic anhydride/N_2. The CH_3COO^- was formed via decomposition of acetic anhydride, whereas CH_2CO^- formed via secondary chemistry.

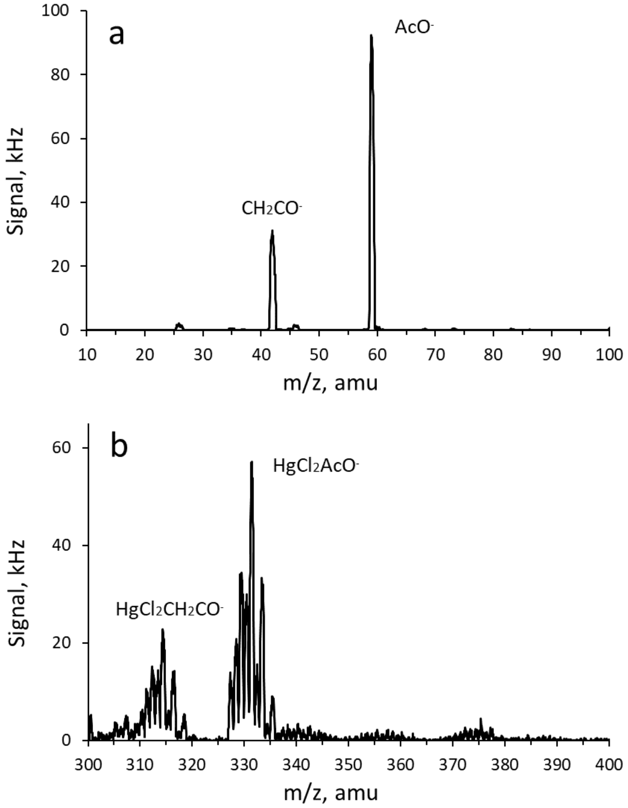

Figure 2.7 Mass spectra of (a) reagent ions generated by corona discharge in acetic anhydride/N_2 and (b) corresponding product ion formed in the presence of $HgCl_2$. The displayed mass spectrum of reagent ions was obtained using a lower electron multiplier voltage to prevent signal saturation.

A previous study has reported that clusters of acetate, $CH_3COOH{\cdot}CH_3COO^-$ (m/z = 119 amu), but we did not observe it using corona discharge because our ion-molecule reaction occurred at low pressure (~2 Torr) (Inomata & Hirokawa, 2017). We used CH_3COO^- as the major reagent ion in our experiments. In the presence of $HgCl_2$, both CH_3COO^- and CH_2CO^- react with $HgCl_2$ via clustering (Equation 2.17a, b) to form $HgCl_2{\cdot}CH_3COO^-$ and $HgCl_2{\cdot}CH_2CO^-$, the spectra were shown in Figure 2.7b.

$$HgCl_2 + CH_3COO^- \rightarrow HgCl_2{\cdot}CH_3COO^- \qquad (2.17a)$$

$$HgCl_2 + CH_2CO^- \rightarrow HgCl_2 \cdot CH_2CO^- \quad (2.17b)$$

2.5 Detection of Hg(0) Using O_2^+ and Cl^-

To be able to measure Hg(0) using ID-CIMS and evaluate the contribution from the dissociative pathway leading to Hg(0) in our experiments, we need to establish a calibration for the detection of Hg(0) using ID-CIMS. The Hg(0) was introduced to the reactor in a flow of N_2 over an impinger containing liquid mercury, which was at room temperature or heated to 90 ºC. We tried both O_2^+ and Cl^- as reagent ions for the detection of Hg(0).

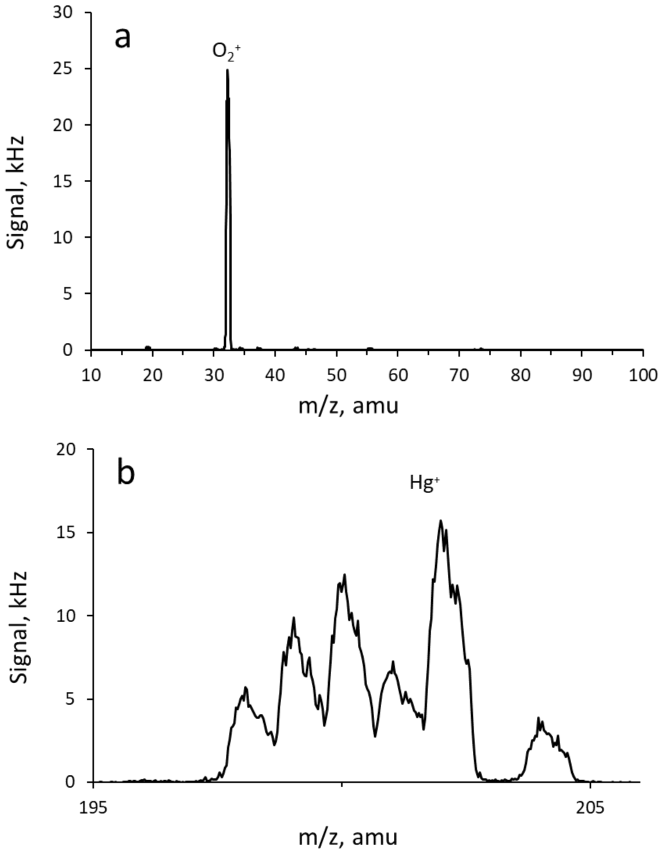

Figure 2.8 Mass spectra of (a) reagent ions generated by corona discharge in O_2/He and (b) corresponding product ion formed in the presence of Hg^0. The displayed mass spectrum of reagent ions was obtained using a lower electron multiplier voltage to prevent signal saturation.

O_2^+ was generated through corona discharge in a mixture of He with a few percent of O_2. The only reagent ion formed was O_2^+ (*m/z* 32 amu) (Figure 2.8a). As shown in Figure 2.8b, the only detected product ion was Hg^+ (*m/z* 195–206 amu) formed via electron transfer (Equation 2.18),

$$Hg + O_2^+ \rightarrow Hg^+ + O_2 \tag{2.18}$$

The Cl^- was generated through corona discharge in $CHCl_3/N_2$. Although Hg(0) detection using Cl^- as the reagent ion was reported (Valadbeigi et al., 2020), where $HgCl^-$ was observed, we did not see any product ion of Cl^- with Hg(0) in our system. The binding energy is ~ 10 kcal/mol in $HgCl^-$, which may not survive at the exit of our drift tube where the focusing electric field is 30-40 V, so our future work is to reduce the electric field but maintain the sensitivity.

2.6 Sensitivity and Limit of Detection of ID-CIMS towards Mercury Species

2.6.1 $HgCl_2$

To determine the sensitivity and LOD of ID-CIMS towards $HgCl_2$, the instrument was calibrated over two $HgCl_2$ concentration ranges, $(0.3–5.2)\times10^9$ and $(0.2–1.2)\times10^{11}$ molecule cm^{-3}, as measured in the drift tube. These concentrations translate into approximately 5–80 ppbv and 290–1760 ppbv mixing ratios because at a 2.1 Torr pressure and 295 K, 1 part per billion by volume (ppbv) corresponds to 6.8×10^7 molecule cm^{-3}. Calibrations in both ranges were performed using a $HgCl_2$ source that operated at two different pressure and temperature sets of conditions.

For the low-concentration range, **method 1** was used (Figure 2.1b), where a plate with a 0.5 mm pinhole was installed between the drift tube and $HgCl_2$ source, allowing maintaining a 360 Torr pressure in the $HgCl_2$ source region and a 1.9-2.1 Torr pressure in the drift tube. A constant flow of 10 standard cubic centimeters per minute (sccm) helium carrier passed through the $HgCl_2$ source, producing a 21 ccm volumetric flow saturated with $HgCl_2$. The gas-phase concentration of $HgCl_2$ was varied by changing the source temperature. The carrier flow was then mixed with a 150 sccm flow of nitrogen diluent, which was pre-heated to the same temperature as that of the $HgCl_2$ source.

For the high-concentration range (**method 2**), the pinhole plate was removed and hence the $HgCl_2$ source was kept at the same 1.9-2.1 Torr pressure as the drift tube (Figure 2.1c). The entire assembly was at a room temperature and the gas-phase concentration of $HgCl_2$ was varied by changing the carrier flow (2–10 sccm) while keeping a constant diluent flow (150 sccm). Thus, a significantly larger amount of the $HgCl_2$ analyte was delivered to the drift tube by a 720-3620 ccm saturated volumetric carrier flow.

Figure 2.9a shows calibration plots obtained in the 5-80 ppbv $HgCl_2$ range with three different reagent ions. The signals correspond to the most abundant peak in each product ion multiplet, i.e., *m/z* 291, 334, and 332 amu for $HgCl_2{\cdot}F^-$, $HgCl_2{\cdot}NO_3^-$, and $HgCl_2{\cdot}CO_3^-$, respectively. The largest slope was observed with SF_6^- and it was followed by $NO_3^-{\cdot}HNO_3$ and CO_3^- reagent ions. Using these slopes and accounting for the sample dilution by the reagent ion carrier, experimental sensitivities S_{exp} of 2.4, 0.8, and 0.9 Hz ppbv^{-1} were obtained.

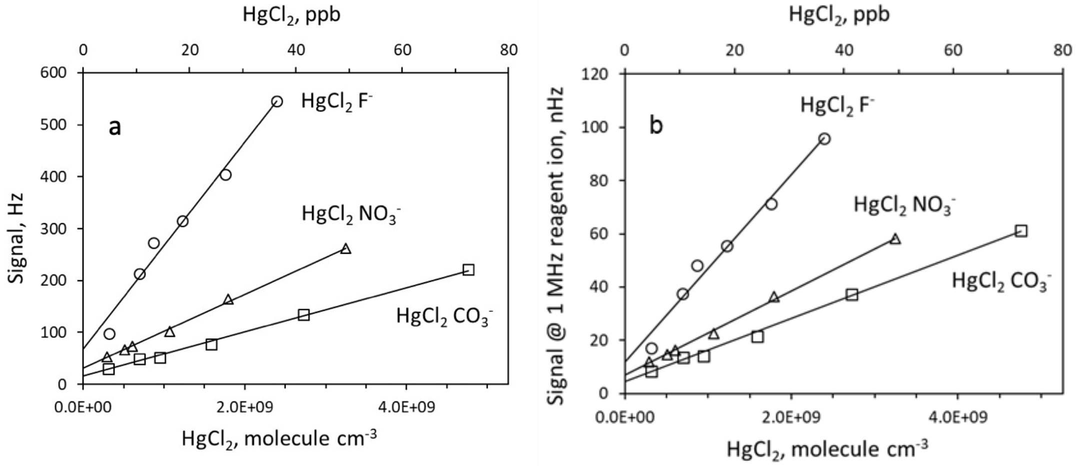

Figure 2.9 Dependence of: (a) the product ion signal and (b) the normalized product ion signal on the calculated concentration of $HgCl_2$ in the drift tube generated using **method 1**. The signal was normalized to 1 MHz reagent count rate. Product ions $HgCl_2{\cdot}F^-$, $HgCl_2{\cdot}NO_3^-$, and $HgCl_2{\cdot}CO_3^-$ were produced using SF_6^-, $HNO_3{\cdot}NO_3^-$, and CO_3^- reagent ions, respectively. Gas flow containing $HgCl_2$ was introduced into the drift tube (1.9-2.1 Torr) through a pinhole from a mixing chamber (360 Torr). The concentration of $HgCl_2$ in the mixing chamber was varied by adjusting the temperature of a solid $HgCl_2$ sample, which was continuously purged with 10 sccm He and then diluted with 150 sccm N_2 heated to the same temperature as the sample.

Figure 2.9b demonstrates that when the data were plotted using the normalized counts per second (nHz or ncps), nominal experimental sensitivities were 0.43, 0.19, and 0.24 Hz ppbv^{-1}, respectively. Non-zero intercepts (20–70 Hz) were frequently observed due to $HgCl_2$ adsorbed on the mixing chamber wall, which was not heated. Closing the valve to separate the mixing chamber from the drift tube reduced the background signal down to ~1 Hz. With the drift tube separated from the calibration source, LOD was 1.1, 7.4, and 4.6 ppbv, using SF_6^-, $NO_3^-{\cdot}HNO_3$, and CO_3^- reagent ions, respectively, for a 10 s integration time and assuming a signal to noise ratio $S/N = 2$. It should be noted that LOD was strongly dependent on the cleanliness history of the mixing chamber and drift tube. The values quoted above were obtained for the system that was operated with the calibration source over several weeks.

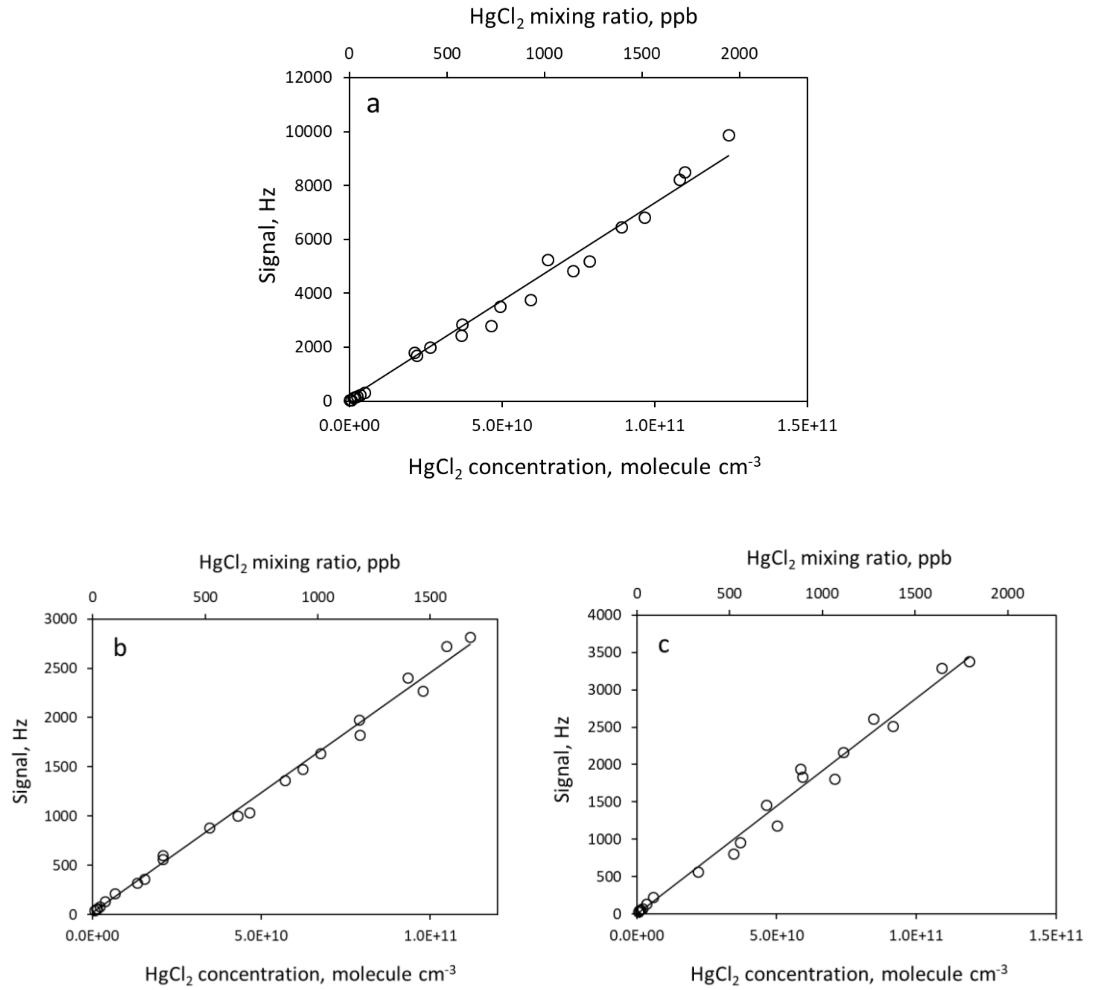

Figure 2.10 Dependence of the product ion signal on the calculated concentration of $HgCl_2$ in the drift tube measured using **method 2** for: (a) SF_6^-, (b) $HNO_3{\cdot}NO_3^-$, and (c) CO_3^- reagent ions. Product ions are $HgCl_2{\cdot}F^-$, $HgCl_2{\cdot}NO_3^-$ and $HgCl_2{\cdot}CO_3^-$, respectively.

Figure 2.10 (a, b, and c) show a good linearity in the calibration plots obtained using higher concentrations of $HgCl_2$, with sensitivities of 1.7, 0.6, and 0.8 Hz ppbv^{-1}, in agreement with those at lower concentrations. Replacing the nitrogen diluent with filtered ambient air at a 40-50% relative humidity resulted in a 0.4% mixing ratio of water vapor in the drift tube but had no notable effect on the detection sensitivity under our analysis conditions.

2.6.2 Hg(0)

The sensitivity of ID-CIMS towards Hg^0 was determined using O_2^+ as the reagent ion. The calibration was conducted in the drift tube under 1.5-2.1 Torr pressure and 293 K. The Hg^0 concentration ranges are $(0.8–1.4)\times10^{11}$ (**method 1**) and $6.2\times10^{11}–1.4\times10^{13}$ (**method 2**) molecule cm^{-3} in the drift tube, corresponding to 1.51–2.12 and 12–223 ppmv mixing ratios, respectively, where 1 part per million by volume (ppmv) corresponds to 5×10^{10} molecule cm^{-3}.

The Hg^0 calibration plots for high ($6.2\times10^{11}–1.4\times10^{13}$ molecule cm^{-3}) and low ($(0.8–1.4)\times10^{11}$ molecule cm^{-3}) Hg^0 concentration ranges are shown in Figures 2.11a and Figure 2.11c, respectively. The signals correspond to the most abundant peak in the Hg^+ multiplet, *m/z* 202 amu. The slope for the higher concentration range is six times lower than the slope for the lower concentration range. In the case of $HgCl_2$, there is good agreement between low and high concentration ranges as the carrier gas helium passes through the column of loosely packed $HgCl_2$ powder to provide sufficient contact surface area and contact time but not for Hg^0, which was introduced into the system by N_2 carrier over Hg(0) source inside an impinger so that there is limited contact time between carrier gas and Hg^0.

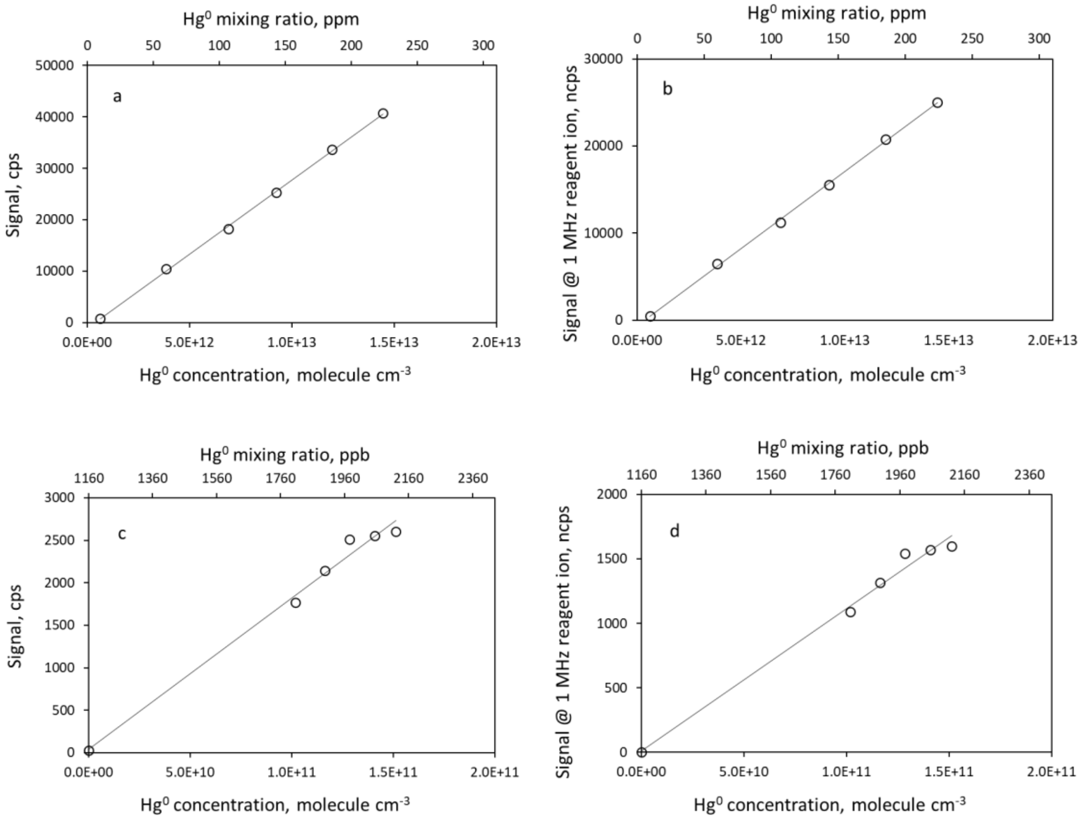

Figure 2.11 Dependence of (a) Hg^+ signal and (b) the normalized Hg^+ signal on the calculated high concentration range of Hg^0 (6.2×10^{11}–1.4×10^{13} molecule cm^{-3} or 12–223 ppmv) using **method 2** and (c) Hg^+ signal and (d) the normalized Hg^+ signal on the calculated low concentration range of Hg^0 (0.8–1.4×10^{11} molecule cm^{-3} or 1511–2119 ppbv) using **method 1**, respectively, in the drift tube. The signal was normalized to 1 MHz reagent count rate. Hg^+ was produced using O_2^+ reacting with Hg^0. Gas flow containing Hg^0 was introduced into the drift tube (1.9-2.1 Torr) directly (a and b) or through a 1/8 inch pinhole (c and d) from a mixing chamber. The concentration of Hg^0 in the mixing chamber was varied by adjusting the Ar flow through a liquid Hg^0 sample and then diluted with 208 sccm He.

Using the slopes and accounting for the sample dilution by the reagent ion carrier, experimental sensitivities S_{exp} of 0.15 and 0.92 Hz ppbv^{-1} were obtained for the concentration ranges of 6.2×10^{11}–1.4×10^{13} molecule cm^{-3} and (0.8–1.4) $\times10^{11}$ molecule cm^{-3}. The normalized count per second (ncps) (Hanson et al., 2003; Warneke et al., 2001), nominal experimental sensitivities (i.e., at a 1 MHz reagent ion signal) were 90 and 570 Hz ppmv^{-1} in Figure 2.11b and 2.11d, respectively. The background signal where ~ 20 Hz nonintercepts exist would drop down to 1 Hz when closing the valve to separate the mixing chamber from the drift tube. The LOD was 0.6 ppbv, corresponding to 4 $\times 10^8$ atom cm^{-3}, for a 10 s integration time and assuming a signal to noise ratio $S/N = 1.5$.

2.7 Steps to Improve LOD and Atmospheric Detection

Using $HgCl_2$ as a surrogate, we demonstrated that ID-CIMS could be applied for direct detection of GOM. The 2.4 Hz $ppbv^{-1}$ sensitivity and 1.1 ppbv LOD obtained with SF_6^- are more than sufficient for laboratory studies of mercury chemistry, including gas-phase oxidation and gas-surface uptake. However, current performance values fall short of the sensitivity and LOD required for direct detection of GOM in the lower troposphere, where its concentration rarely exceeds 100 pg m^{-3} (Travnikov et al., 2017), a value that corresponds to 3×10^5 molecule cm^{-3} or 0.015 part per trillion by volume (pptv) at atmospheric temperature and pressure. Below, we discuss factors that limit the sensitivity and LOD of our ID-CIMS relative to comparable instruments and propose modifications for making direct detection of atmospheric GOM possible.

A state-of-art ID-CIMS (or PTR-MS) with a drift tube operating at a 4-10 Torr pressure may attain a sensitivity as high as 200-1000 Hz $ppbv^{-1}$ and an LOD as low as 10-100 ppt (Hanson et al., 2009; Levy et al., 2014). In terms of hardware, major contributors to the higher sensitivity relative to our system are a larger displacement turbo pump (e.g., 650 L s^{-1}) and the presence of a tri-filter quadrupole, which combined allow extraction of a larger number of ions from the drift tube (×3) and mass-filtering those ions at a higher transmission rate (×2), respectively. Operating our drift tube at 4 to 10 Torr pressure would provide an additional (×2-5) boost in sensitivity due to a longer ion-molecule reaction time, whereas keeping the drift tube at an elevated temperature (50-70 °C) would reduce background signal from the adsorbed analytes, improving the LOD. An additional gain in sensitivity (×2-3) can be attained by using a higher multiplier voltage (a sub-optimal voltage was used in our study to preserve the multiplier lifespan). Finally, it should be noted that the total signal of mercury ions is distributed among several isotopes, where the strongest isotope contributes approximately 26% of the total sum. Hence, the sensitivity to mercury is a factor of 4 lower than the sensitivity to chemicals that contain no multiple abundant isotopes.

Another way to improve sensitivity is to change the electric field configuration in the drift tube. By adding a parallel 0.5 MΩ resistor in the drift tube, the electric field in the drift tube was decreased from 11 V/cm to 3 V/cm; the signal intensity was enhanced by 15 times, leading to a boost in normalized sensitivity about 15 times. The reasons are (1). A lower electric field leads to better focusing of ions; (2). Longer ion-molecule reaction time in the drift tube. As described in Equation (1.11), the product ion intensity is proportional to the reaction time.

More improvements in the sensitivity and LOD were made, including replacing the quadrupole and enlarging the pin hole. The old quadrupole was replaced by a 19 mm tri-filter quadrupole, which improves the transmission and peak shape, leading to a twice higher sensitivity in the detection. Noted that the chamber separator had to be replaced as well in order to fit the tri-filter quadrupole, whose cables and connections took slightly more space than the old quadrupole, into the vacuum chamber. Meanwhile, since the hole pattern and enclosure of the tri-filter quadrupole are slightly different from the old quadrupole, ions generated by the ionization gauge can fly directly into it, producing noises in the lower mass region (10-50 amu), a 1/2 inch stainless steel elbow has to be inserted to prevent the noises from the ionization gauge entering the new quadrupole. To increase the number of ions passing through the pin hole, we replaced the 0.3 mm pin-hole plate with a 0.4 mm pin-hole plate, which requires better pumping to maintain the same pressure in the region between the mass spectrometer and the drift tube, so that an Agilent Twis Torr 304FS turbopump was added to that region. The product ion intensity remains the same, which means that the ion beam and focusing are reasonable when passing the pin hole.

Table 2.1 Relative Sensitivity for the Modifications Made in ID-CIMS Compared Against its Initial Sensitivity

Instrumental modifications	Increase in sensitivity
After modifying the drift tube	×15
After replacing quadrupole	×2
After increasing the pin-hole diameter	1

The most significant improvement in sensitivity in the future, by nearly 3 orders of magnitude, can be achieved by switching to multi-stage atmospheric pressure chemical ionization. Operating the drift tube at atmospheric pressure eliminates the dilution of the analyte and allows a significantly longer ion-molecule reaction time. A sensitivity of 500 Hz pptv^{-1} with an LOD of (2-5)×10^{4} molecules cm^{-3} has been achieved using this approach for analytes with molecular weights of around 100 amu, such as sulfuric acid (Eisele & Tanner, 1993; Zheng et al., 2010).

To reduce mass discrimination and improve sensitivity when analyzing significantly heavier mercury-containing ions where the signal is comprised of several isotopes, the use of a lower mass resolution will be beneficial. For instance, increasing Δm

to 1.6 amu in our system resulted in a factor of 3 increase in the signal intensity and a proportional increase in the sensitivity (Figure 2.12). As shown by Eisele and Hanson, a more substantial decrease in the resolution (Δm ~ 10) may afford a 20-fold increase in the signal intensity at *m/z* 500 amu (Eisele et al., 2000). Note that decreasing the resolution may cause mercury peaks to overlap with the ones produced by other chemicals, so future work should focus on elucidating reagent ions that react with mercury-containing molecules with high selectivity. Another important factor to consider is that the ion-molecule reactions must be fast and produce a single ion product, which is strongly bound. Overall, we estimate that at a 1 amu resolution, AP-CIMS can achieve an LOD of (8-20)$\times 10^4$ molecules cm^{-3} for GOM. Reducing the resolution, can bring the LOD to the same level as reported for H_2SO_4 (Eisele & Tanner, 1993; Zheng et al., 2010).

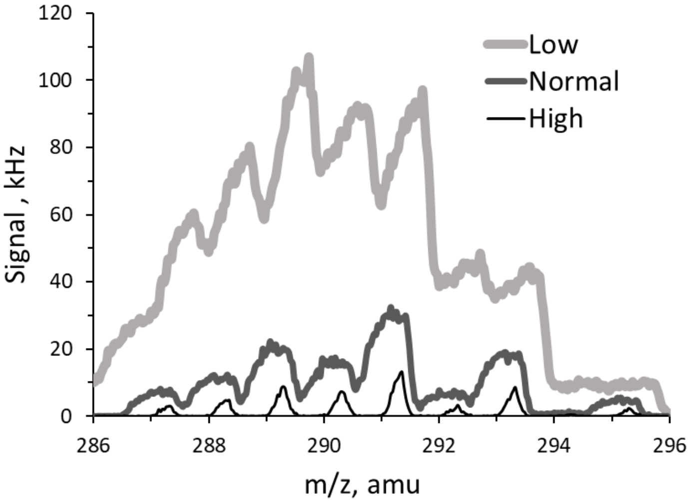

Figure 2.12 Mass spectra of $HgCl_2F^-$ obtained using high, normal, and low quadrupole resolutions, corresponding to Δm of approximately 0.4, 0.9, and 1.6 amu.

CHAPTER 3

HETEROGENEOUS UPTAKE OF GASEOUS OXIDIZED MERCURY ON SURFACES

3.1 Introduction

Atmospheric deposition is an important source of various toxic chemicals for surface waters and terrestrial environments. Atmospheric mercury is deposited through dry deposition (ocean and surfaces) and wet deposition (aerosol particles, rain droplets), which is considered as an important removal pathway of GOM and PBM. However, studies of GOM and its interaction with environmental surfaces were limited by the current detection method, which cannot provide molecular speciation of GOM. This section aims to study heterogeneous uptake of GOM surrogates on environmental surfaces, including inorganic salts and organic compounds. Experiments are performed in a fast flow reactor coupled with ID-CIMS. The mechanisms are determined by changing GOM surrogates and changing inorganic/organic aerosol substrates on the surfaces. Reactivities of GOM on different surfaces are affected by the surface composition and structure of molecules that are applied on the surface. Mercury chloride, mercury bromide, and mercury iodide are used as surrogates of GOM.

3.2 Selection of Gas and Surfaces

3.2.1 Selection of GOM Surrogate

We selected $HgCl_2$, $HgBr_2$, and HgI_2 as a GOM surrogates for our experiments, following the finding that it behaves similarly to atmospheric GOM with respect to capture by denuders (Malcolm et al., 2009). These chemicals are commercially available, chemically stable, readily transferred to the gas phase, and detected by ion drift-chemical ionization mass spectrometry (ID-CIMS) (Khalizov et al., 2020). As Lewis acids (Cotton et al., 1980), mercury halides readily bind with negatively charged ligands both in the gas phase (Khalizov et al., 2020) and in aqueous solutions (Sjoberg, 1977).

3.2.2 Selection of Surfaces

Aerosols are liquid or solid particles suspended in the air and generated from natural and anthropogenic sources. These small particles can provide sufficient surfaces for the wet deposition and are typical of sizes in the range of few nanometers to tens micrometers. The chemical composition of aerosols may affect the gas-surface reactions of GOM. Natural aerosols include sea salt generated from breaking waves, mineral dust blown from the surface by wind, and organic aerosols from biogenic emissions. Anthropogenic aerosols include sulfate, nitrate, and carbonaceous aerosols and are mainly from fossil fuel combustion sources. In general, I choose two types of aerosol surfaces for the uptake experiments: inorganic salts and organics.

Inorganic salts. Atmospheric aerosols are made of a large number of organic and inorganic compounds, where the inorganics can contribute up to 25-50% of the total dry fine particle mass (Heintzenberg, 1989; Jimenez et al., 2009). Although the fractional composition varies widely between different locations, certain inorganic constituents are ubiquitous in the majority of atmospheric particles. Ammonium, sulfate, and nitrate ions are common in urban aerosols; sodium, chloride, and sulfate ions are some of the major ions in marine aerosols; various oxides are the principal constituents of mineral dust. Accordingly, we selected ammonium sulfate ($(NH_4)_2SO_4$, Sigma Aldrich, $\geq 99\%$) and ammonium nitrate (NH_4NO_3, Acros Organics, $> 99\%$) to represent fine urban aerosols, sodium chloride (NaCl, Fisher Scientific, ≥ 99%) and sodium sulfate (Na_2SO_4, Sigma Aldrich, ≥ 99%) for sea salt, and the surface of an untreated frosted borosilicate glass tube for mineral dust.

Organic compounds. Organic aerosols in the atmosphere contain a multitude of organic species which are either directly emitted or produced by a series of chemical reactions. Organic species are the most abundant aerosol species in both urban and rural areas (Pöschl, 2005). Hydrogen to carbon atomic ratio (H:C) and the oxygen to carbon atomic ratio (O:C) are good indicators of atmospheric oxidation of organic aerosols (Kroll et al., 2011). Here, I used several carbonaceous aerosols of primary and secondary origin as organic surfaces. Primary combustion aerosols were represented by soot, levoglucosan (H:C=5:3), and polycyclic aromatic hydrocarbons (PAHs, such as perylene and pyrene). Secondary aerosols were represented by carboxylic acids (succinic, pimelic, and citric acid) and dioctyl sebacate (DOS). Soot and PAHs are produced by combustion processes, levoglucosan is the indicator of biomass burning. Organic acids are chosen because they are soluble, commonly exist in aerosols. $HgCl_2$ is expected to partitioning differently on these organic aerosols with different ratios of O:C and H:C.

3.3 Experimental

Gas-surface uptake of $HgCl_2$ was studied using a fast flow reactor coupled to an ion drift-chemical ionization mass spectrometer (ID-CIMS, Figure 3.1) (Khalizov et al., 2020; Qiu et al., 2011). Measurements were conducted by exposing gaseous $HgCl_2$ to an inorganic salt surface and then detecting the unreacted gaseous $HgCl_2$ by converting it to the

$HgCl_2 \cdot NO_3^-$ product ion through the ion-molecule reaction with $HNO_3 \cdot NO_3^-$ (Equation 2.4).

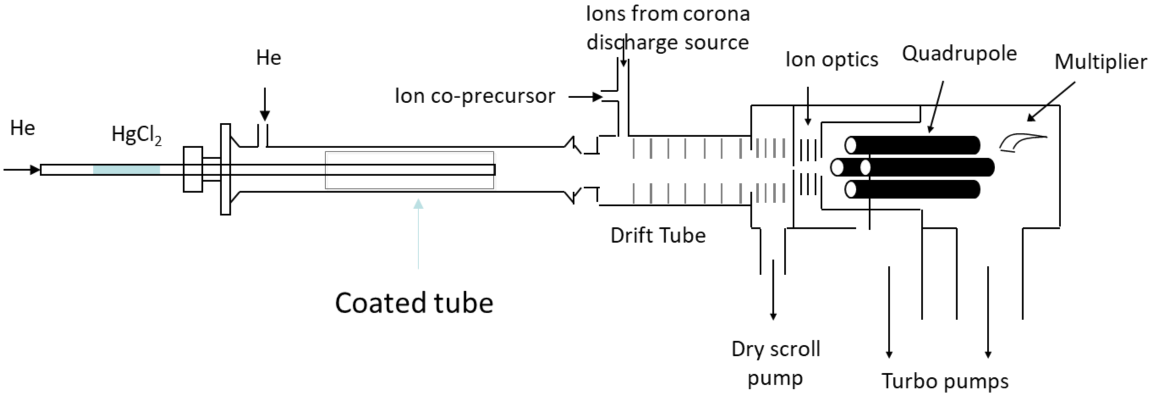

Figure 3.1 A fast-flow reactor coupled to an ion drift - chemical ionization mass spectrometer.

The reagent ion was generated from a trace amount of HNO_3 vapor in N_2 gas in the corona discharge (Figure 3.1) (Khalizov et al., 2020). Gaseous $HgCl_2$ in helium (1-10 sccm) was introduced into the flow reactor through a movable injector. The source of $HgCl_2$ was a glass impinger with a solid $HgCl_2$ layer coated on the inner wall or, in later experiments, a column of crystalline $HgCl_2$ powder packed between two plugs of deactivated glass wool. The carrier helium flow (135 sccm) was introduced through the side inlet at the back of the reactor. All gas flows were monitored/controlled by calibrated mass flow meters/controllers. To minimize $HgCl_2$ wall adsorption, the reactor wall was deactivated by pre-treating it with dichlorodimethylsilane (DCDMS). The reactor temperature and pressure were 293 ± 2 K and 1.8-2.0 Torr, respectively.

Inorganic salts were used in the form of a polycrystalline coating layer deposited on the inner surface of a frosted glass tube (1.56 cm inner diameter and 10 cm length), which was placed inside the reactor (2 cm inner diameter and 30 cm length). To prepare the coating layer, the frosted tube was rinsed inside with the saturated solution of inorganic salt and then dried in a rotating holder in a flow of nitrogen (Landis et al., 2002). To obtain thicker coats, the rinse-dry procedure was repeated several times. To ensure a uniform layer, coating and drying steps were performed in custom-made devices (details described in Section 3.3.1). The coating layer uniformity, critical for obtaining reproducible uptake results, was found to be within 10% between the two halves of the tube, using dissolution experiments (details described in Section 3.3.2). In several experiments, we attempted to detect the release of Hg(0) from the surface, using the O_2^+ reagent ion (Equation 2.7).

In the case of organic coatings, PAH coatings were dissolved in acetone, then applied the solution on the frosted tube surfaces to let acetone evaporates by flowing nitrogen. DOS liquid was applied directly to the frosted glass tube without further drying. The soot was generated by burning propane onto the glass tube, where coating thickness was estimated based on a previous study (Khalizov et al., 2010). Other organic acid coatings were prepared the same as the inorganic salt coatings preparation mentioned above. Noted that the pH of organic acids referred to the pH in the aqueous solution, not on the surface.

3.3.1 Tube Coating Preparation

Frosted tubes were prepared by sandblasting the inner surface of plain borosilicate tubes. Figures 3.2 and 3.3 show the rinsing and drying procedures utilized to prepare a uniform inorganic salt layer on frosted glass tubes. For coating, the frosted glass tube is dipped into a beaker with a saturated inorganic salt solution, and a vacuum is applied to suck the solution up the tube, repeating at least three times to make sure that the saturated solution distributes uniformly (Figure 3.2). After shaking off the excess solution, the rinsed tube is placed in a plastic tube holder connected to an electric motor, and a ¼ inch outer diameter stainless injector is inserted coaxially to supply dry nitrogen gas (Figure 3.3). The injector has multiple 1/8 inch holes drilled along its length. In addition, a stainless-steel braid sleeve is placed over the injector to ensure a uniform drying flow.

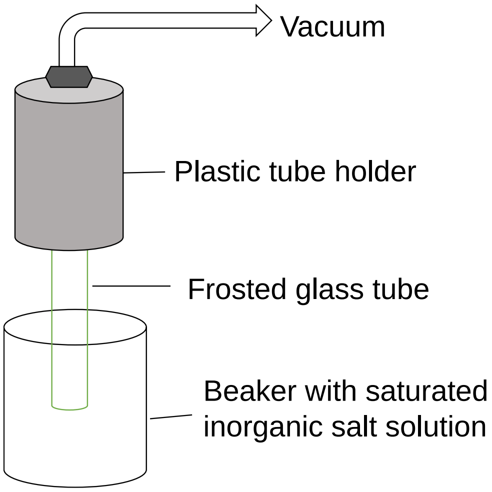

Figure 3.2 Tube coating device.

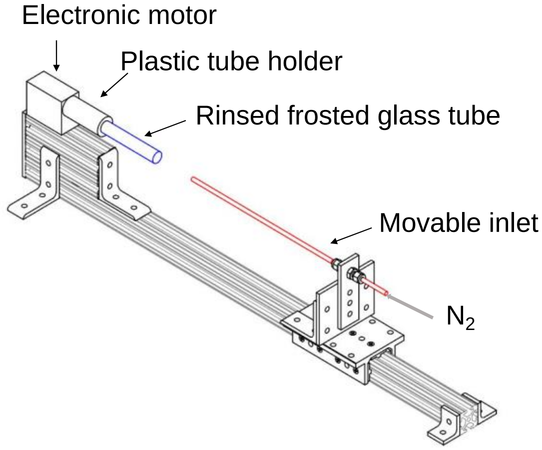

Figure 3.3 Tube drier with a movable stage.

3.3.2 Verification of Uniformity of the Coating Layer

To check the uniformity of the coating layer, the coated tube was carefully immersed into distilled water to half of its length to remove half of the coating. The coating mass that remained on the tube was determined by weighing the dried tube, subtracting the mass of the bare tube, and comparing it with the original coating mass. We found that the variation in the coating mass between the two halves of the tube did not exceed 10%.

3.4 Uptake Data Processing

3.4.1 Uptake Coefficient

The signals of the product ion before exposure (I_o) and after exposure (I_t) were used to calculate the observed first-order rate constant (k_{obs}) (Aubin et al., 2007),

$$k_{obs} = \frac{\mathrm{d}\ln I}{\mathrm{d}t} = \frac{u}{L} ln \frac{I_0}{I_t} \tag{3.1}$$

where u is the flow velocity, L is the exposed surface length, and $\mathrm{d}t = u/L$ is the interaction time. The value of k_{obs} is a combination of the reactive loss due to $HgCl_2$ collisions with the surface (k_r) and resistance diffusing to the surface (k_d) (Gershenzon et al., 1995; Li et al., 2020; Pöschl et al., 1998),

$$\frac{1}{k_{obs}} = \frac{1}{k_d} + \frac{1}{k_r} \tag{3.2}$$

$$k_d = \frac{3.66D_g}{r^2} \tag{3.3}$$

where r is the tube radius and D_g is the diffusivity of $HgCl_2$ in helium at a given temperature and pressure (D_g = 0.431 cm^2 s^{-1} at 298 K and 760 Torr (Yaws, 2012; 2013; 2014)). Owing to using helium carrier gas and reduced reactor pressure, the diffusion correction never exceeded 22%. The uptake coefficient (γ), defined as the ratio of the number of trace-gas molecules removed from the gas to the total number of collisions with the surface, was calculated from $HgCl_2$ mean thermal velocity ($\omega = 1.52\times10^4$ cm/s) and k_r (Davidovits et al., 2011; Howard, 1979).

$$\gamma = \frac{2rk_r}{\omega} = \frac{k}{\omega}\left[\frac{V}{A_{geom}}\right] = \frac{2kr}{\omega}\left[\frac{A_{geom}}{A_{true}}\right] \tag{3.4}$$

On the right-hand side of this equation, V is the reactor volume corresponding to the exposed surface, and A_{geom} and A_{true} are the geometric and true areas of the exposed polycrystalline salt surface. All of the parameters used in calculations are provided in Table 3.1.

Table 3.1 Parameters Used to Process Experimental Data to Derive Uptake Coefficients on Different Surfaces

Parameters	
$\boldsymbol{P}$ (Torr)	~ 2
$\boldsymbol{L}$ (cm)	1 - 5
$\boldsymbol{u}$ (cm s^{-1})	~ 500
$\boldsymbol{D_g}$ (cm^2 s^{-1})	~ 170
$\boldsymbol{k_d}$ (s^{-1})	~1000

3.4.2 Surface Capacity

The surface capacity is defined as the amount of $HgCl_2$ molecules taken up by the surface from the beginning of exposure until the signal recovered to within $1/e$ of its initial value. It is calculated using:

$$\text{Surface Capacity} = \frac{\left(I_{1/e} t_{1/e} - \int_0^{t_{1/e}} I_t dt\right) C_{HgCl_2} Q \frac{760}{P}}{I_{1/e} A_{geom}} \tag{3.5}$$

where $t_{1/e}$ is the time when $HgCl_2$ signal recovers to within $1/e$ of its initial signal (e-folding time), $I_{1/e}$ is the signal of $HgCl_2$ at e-folding time, C_{HgCl_2} represents the gas-phase concentration of $HgCl_2$, Q is the standard flow into the reactor, P is the pressure in the reactor (Torr).

3.5 Heterogeneous Uptake of $HgCl_2$ on Inorganic Surfaces

The aim of our study was to determine the rate and mechanism of the heterogeneous reaction of mercury (II) chloride (mercuric chloride, $HgCl_2$) with the surfaces of inorganic salts commonly present in urban and marine aerosols, including sodium sulfate, sodium chloride, ammonium sulfate, and ammonium nitrate. The obtained kinetic and mechanistic data will help to establish a more detailed mechanism of GOM removal by aerosol particles in atmospheric models.

3.5.1 Initial and Steady-State Uptake Coefficients

Figure 3.4 shows a typical uptake curve, where the $HgCl_2$ signal is plotted against the exposure time and the number of $HgCl_2$ molecules passed over the NaCl surface. The mass of NaCl was 0.25 g, corresponding to a 16 μm effective coating layer (as explained in the following section). The number of molecules was calculated from the exposure time, $HgCl_2$ concentration, and gas flow rate. At the beginning of the experiment, the injector tip was positioned downstream of the coated tube to prevent interactions between the NaCl surface and $HgCl_2$, corresponding to an initial signal (I_A). At approximately 1 min, the injector was retracted to expose gaseous $HgCl_2$ to a 5 cm length of the salt surface. As a result of the exposure of $HgCl_2$ to the surface, the signal dropped rapidly (I_B). It then recovered gradually during several minutes, reaching a nearly steady-state level (I_C), which was below the initial signal, I_A. At ~6 min, the injector was returned to its original position to stop the exposure, at which point the desorption of any unreacted $HgCl_2$ occurred, as seen from the signal rapidly increasing, then decreasing gradually and eventually stabilizing at the initial value I_A. Here and below, we use 'reacted' and 'chemisorbed' synonymously. Note that due to a small signal drift, the signal after uptake often stabilized at a slightly higher or lower value. In such cases, I'_A was interpolated from $HgCl_2$ signals before and after uptake, e.g., at 1.9 and 8.9 min as shown in Figure 3.4. The ratios I_A/I_B and I'_A/I_C were used to calculate the first-order rate constants (eq. 3.1) of the initial and steady-state uptake, which were further converted by eq. 3.2-3.4 to the initial and steady-state uptake coefficients, $\gamma_i = (2.2\pm0.4)\times10^{-2}$ and $\gamma_{ss} = (1.9\pm0.6)\times10^{-3}$ in the case of NaCl. Examples of typical signal intensities and other parameters obtained on NaCl and other salts are provided in Table 3.1.

Additionally, the uptake curve was used to evaluate the surface capacity and surface coverage. The surface capacity corresponds to the number of $HgCl_2$ molecules taken up by the surface over the period from the beginning of exposure to the point when the signal recovered to within $1/e$ of its initial value (1.2×10^{14} molecule cm^{-2} for NaCl in Figure 3.4). The surface coverage (24% for NaCl in Figure 3.4) corresponds to the measured surface capacity normalized by the maximum surface capacity (5.25×10^{14} molecule cm^{-2}), where the latter is calculated based on the area of a single $HgCl_2$ molecule (1.91×10^{-15} cm^{2}) and geometric surface area exposed to $HgCl_2$.

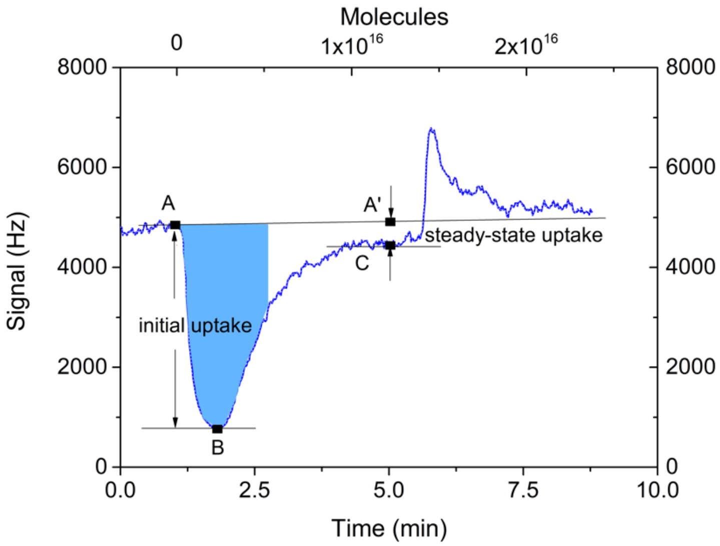

Figure 3.4 Temporal profile of $HgCl_2$ uptake on NaCl surface. The total pressure in the flow reactor is 1.94 Torr and gas-phase concentration of $HgCl_2$ is 5.7×10^{10} molecules cm^{-3}. The secondary abscissa shows the number of $HgCl_2$ molecules that have passed through the reactor at a given reaction time. The effective coating thickness is 16 μm and the exposed length is 5 cm. The shaded area was used to calculate the surface capacity, which is the amount of $HgCl_2$ taken up by the surface from the beginning of exposure until the signal recovered to within 1/*e* of its initial value.

3.5.2 Reactivities of Different Salts

The uptake of $HgCl_2$ was measured on the surfaces of several inorganic salts (Figure 3.5), using effective coating mass of ~0.25 g. All uptake curves showed a common behavior, where upon exposure the gas-phase concentration of $HgCl_2$ dropped rapidly and then recovered gradually. However, the magnitude of the drop and the rate of recovery varied significantly between different salts.

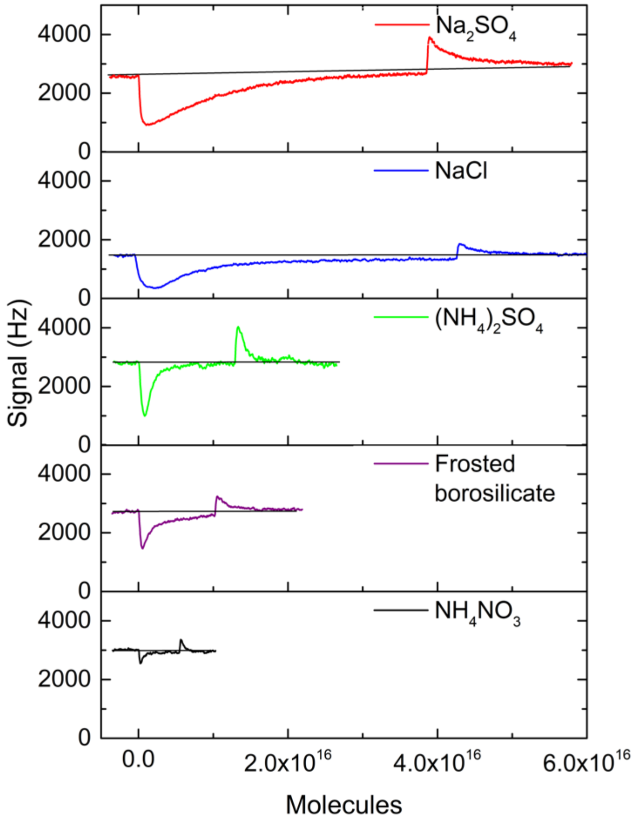

Figure 3.5. Uptake of $HgCl_2$ on different salts. The exposed length is 2 cm for Na_2SO_4 and 5 cm for all other salts. The total pressure in the flow reactor is ~1.94 Torr and gas-phase concentration of $HgCl_2$ is $(3.0\text{-}5.7)\times10^{10}$ molecules/cm^3.

The uptake on NH_4NO_3 was the smallest and nearly fully reversible, with the lowest values of the initial (3.6×10^{-3}) and steady-state (3.3×10^{-4}) uptake coefficients (Table 3.2). At the other end of reactivity was Na_2SO_4, with the largest drop and slowest recovery of the $HgCl_2$ signal, corresponding to initial and steady-state uptake coefficients of 3.1×10^{-2} and 1.7×10^{-3}, respectively. In some cases, the reaction time had to be varied by changing the velocity of the gas flow or exposed length of the salt surface to improve measurement accuracy, e.g., the exposed length was reduced to 2 cm when using the most reactive Na_2SO_4. None of the salts, including NH_4NO_3, showed a full recovery of $HgCl_2$ signal when the injector was kept retracted, indicating the presence of an irreversible chemical reaction in addition to reversible adsorption.

Table 3.2 Initial and Steady-State Uptake Coefficients of $HgCl_2$ on a Fresh Crystalline Coating Layer Made of Different Salts. Coating Mass is 85-330 mg, Corresponding to a 5-21 μm Effective Coating Thickness

Salt	Uptake coefficient [a]		Surface capacity, [b] molecule cm^{-2}	Surface [c] coverage, %
	Initial	Steady-state		
Na_2SO_4	3.1×10^{-2}	1.7×10^{-3}	5.1×10^{14}	98
NaCl	$(2.2 \pm 0.4)\times10^{-2}$	1.9×10^{-3}	3.4×10^{14}	65
$(NH_4)_2SO_4$	$(1.4 \pm 0.3)\times10^{-2}$	7.0×10^{-4}	3.0×10^{13}	5.6
Frosted borosilicate	8.0×10^{-3}	3.9×10^{-4}	2.4×10^{13}	4.6
NH_4NO_3	3.6×10^{-3}	3.3×10^{-4}	1.6×10^{12}	0.3

[a] If the standard deviation is not shown, the relative error is under 30%

[b] The number of $HgCl_2$ molecules taken up by the surface from the beginning of exposure until the signal recovered to within 1/*e* of its initial value

[c] The measured surface capacity normalized by the maximum geometric surface capacity.

The overall reactivity decreased in the series Na_2SO_4 > NaCl > $(NH_4)_2SO_4$ > frosted borosilicate tube > NH_4NO_3, as shown by the values of the initial and steady-state uptake coefficients given in Table 3.2. Surface capacity and surface coverage followed the same trend as the uptake coefficient. The reactivity of the frosted borosilicate glass surface, which can serve as a surrogate for mineral dust, was not negligible, with initial and steady-state uptake coefficients of 8.0×10^{-3} and 3.9×10^{-4}, respectively. However, no observable uptake was detected on the fused (unfrosted) borosilicate glass surface, even in the absence of the DCDMS treatment.

3.5.3 Mechanism

Reaction depth. Our uptake measurements were conducted on crystalline salts, where the bulk diffusion of $HgCl_2$ is expected to be severely limited. For instance, using a typical diffusivity in solids (10^{-11}–10^{-10} cm^2 s^{-1}) and an interaction time of 1000 s, we estimated a diffusion depth of only 1–3 μm. To verify if the uptake indeed was confined to the salt surface, we studied the dependence of the uptake coefficient on the effective thickness of the NaCl coating layer. The thickness was estimated from the mass of the salt deposited inside the tube, its geometric surface area, and bulk density (2.165 g cm^{-3}), assuming a smooth and uniform salt layer.

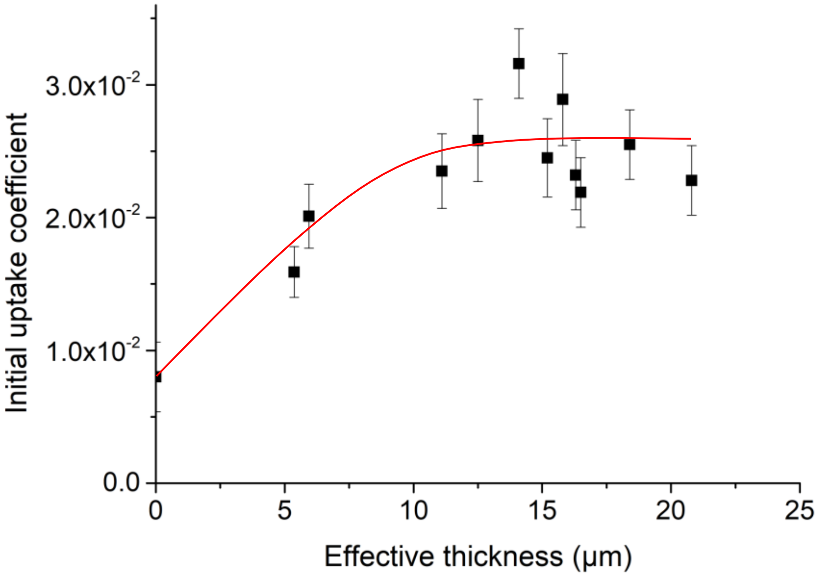

Figure 3.6 Dependence of the uptake coefficient on the effective coating thickness of NaCl. The value at zero thickness corresponds to reaction on bare frosted tube. The line is drawn to guide the eye.

Figure 3.6 shows that starting with a bare frosted tube, the uptake coefficient increased with the effective NaCl layer thickness and then stabilized for layers thicker than 10-15 µm. A coating thickness significantly greater than the estimated diffusion depth of 1–3 µm for reaching saturation could be caused by the solid surface being polycrystalline and non-uniform. Indeed, non-uniformity was visually noticeable as patterns, stripes, and variations in the salt crystal size. To improve coating uniformity, a drying device was designed and built, as described in Section 3.2.1, allowing for the production of more uniform coatings (Section 3.2.2) and for a better reproducibility in the uptake data. Additionally, we cannot rule out the presence of a thin aqueous layer on the salt surface even under conditions of our experiment (a fast flow of dry helium at a 2 Torr pressure). Hence, the surface reaction may have occurred within a thin aqueous layer present on the solid salt (De Haan et al., 1999), which will be shown later in this chapter.

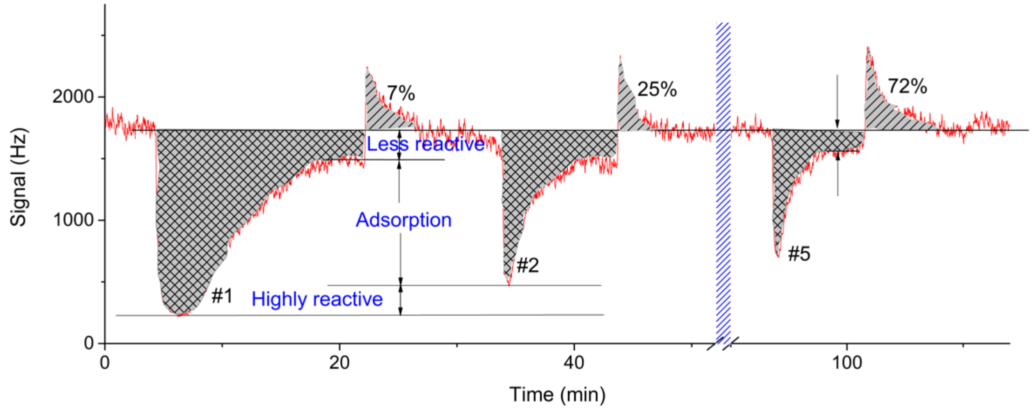

Figure 3.7 A decrease in the NaCl surface reactivity after repeated exposures to gaseous $HgCl_2$. Three regions marked on the uptake curve correspond to reactive sites (highly reactive and less reactive) and physisorption sites. Grey crosshatched and hatched areas mark the amounts of adsorbed and desorbed $HgCl_2$, respectively, where percentages correspond to the ratios of the amount desorbed to the amount adsorbed for each exposure.

Surface coverage. Repeated exposure of the same surface to gaseous $HgCl_2$ resulted in a significant decrease of the surface reactivity. Figure 3.7 shows an uptake curve from the experiment where the injector was retracted to initiate exposure, and then returned to the initial position to stop exposure, and this process was repeated five times. During these experiments, exposure was stopped when the signal recovered to a steady-state value and then sufficient time was given to allow the adsorbed $HgCl_2$ to either react irreversibly with the surface or desorb back, entering the gas flow. It can be seen that the drop in the $HgCl_2$ signal on the second exposure at ~33 min was shallower, and the signal returned to the steady-state level significantly faster than during the first exposure. Upon subsequent exposures, a progressively shallower drop was observed, and the signal recovered faster and to a higher value, which was closer to the initial signal of $HgCl_2$. This behavior indicates the reduction in the number of surface sites capable of reacting irreversibly with $HgCl_2$. Accordingly, progressively larger amounts of $HgCl_2$ (marked in hatched grey) desorbed from the surface, corresponding to 7, 25, and 72% of the amount taken (marked in crosshatched grey) for runs #1, #2, and #5, respectively (Figure 3.7).

Figure 3.8 shows that the initial uptake coefficient decreased by ~50% on the second exposure and remained nearly constant on the third and subsequent exposures. The steady-state uptake coefficient decreased by about 30% after three exposures, remaining nearly constant afterwards. Notably, surface coverage exceeded 150% already after the first exposure and continued to increase, reaching nearly 350% after several subsequent exposures. This surface coverage was estimated using the total area of deposited $HgCl_2$ molecules, as determined from the curve in Figure 3.7, together with the *geometric* surface area of the exposed NaCl. The observed saturation in reactivity at surface coverages in excess of 100% indicates that the actual area of the multicrystalline salt surface exceeded the geometric area. Hence, the uptake coefficients may have been somewhat overestimated, as discussed below. It is also possible that the reaction occurred within a thin aqueous layer on the salt surface, as described above.

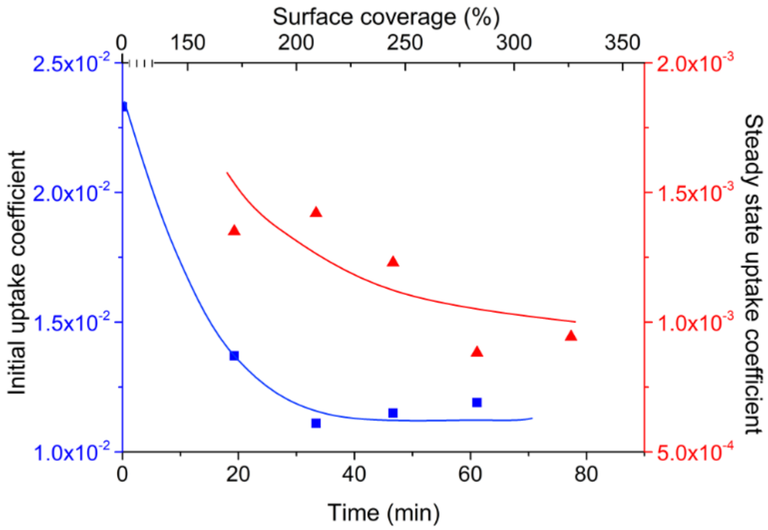

Figure 3.8 Dependence of the initial and steady-state uptake coefficients on the total exposure time and surface coverage ($HgCl_2$ on a NaCl surface). The curves are drawn to guide the eye.

Reversible adsorption and irreversible reaction. The shape of the uptake curve and the observed decrease in reactivity on repeated exposures can be rationalized by considering three types of surface sites: highly reactive (e.g., reactive adsorption), less reactive (e.g., chemisorption), and adsorptive (e.g., physisorption), as marked in Figure 3.7. The initial drop in $HgCl_2$ on the first exposure is due to its interaction with all three types of sites, whereby most of the highly reactive sites are irreversibly consumed. These highly reactive sites probably correspond to surface defects and edges of salt crystals (Butt et al., 2003). Upon the second and further exposures, the remaining reactivity is due to less reactive sites (γ_{ss}) and adsorptive sites (γ_i after two exposures), hence leading to a shallower drop in the signal and a faster recovery. The less reactive sites, responsible for the steady-state uptake, probably correspond to smooth crystal terraces or hard-to-reach locations within the polycrystalline surface. The physical adsorption sites bind reversibly, and when exposure is stopped by resetting the injector, they release the adsorbed $HgCl_2$ and hence can again participate in binding upon subsequent exposures. Based on the relatively fast signal drop and recovery upon the second and further exposures, physisorption sites appear to be limited in number, similar to the highly reactive sites. The actual number of less reactive sites may exceed the number estimated based on the geometric surface area. Whereas this would have a negligible effect on the magnitude of the initial uptake coefficient, which corresponds to $HgCl_2$ interacting with the most reactive (or most available sites), the steady-state coefficient may be overestimated by a factor of 3 or more, as follows from the A_{geom}/A_{true} ratio in Equation (3.6).

The chemical nature of different surface sites is not well known, but computational studies show that $HgCl_2$ binds reversibly on the NaCl(100) surface and dissociatively on the $NaCl(111)^{Na}$ surface (Tacey et al., 2016). For the former pathway, it is possible that similar to aqueous solutions, surface reactions produce tri- and tetra-coordinated mercury ion complexes $[HgCl_3]^-$ and $[HgCl_4]^{2-}$. To evaluate the contribution from the dissociative pathway leading to Hg(0), we attempted to measure the release of elemental mercury during and after $HgCl_2$ uptake, including upon heating of the $HgCl_2$-exposed surface to ~120 °C, but detected no Hg(0). Based on the LOD of our system towards Hg(0), less than 1% of $HgCl_2$ could have been converted to Hg(0) on the NaCl surface. This finding is unsurprising because the NaCl(100) surface with its alternating positive and negative ions is more thermodynamically stable than NaCl(111)^{Na}, composed entirely of positively charged sodium ions (Bruno et al., 2008; Radenović et al., 2006; Tacey et al., 2016). Hence, only the NaCl(100) surface is expected to form upon crystallization of a NaCl solution. It is possible that NaCl(111)^{Na} may have represented some of the surface defects, but the amount of Hg(0) was either below our LOD or the release of Hg(0) may have required photo-irradiation. Further research is needed to establish the nature of the $HgCl_2$ products on salt surfaces.

One-step or two-step mechanism. Referring to adsorptive sites as S, reactive sites as R, and reaction product as P, one can write three possible processes (3.6-3.8) to account for the observed uptake behavior of gaseous $HgCl_2$:

$$HgCl_2 + S \rightleftharpoons HgCl_2 \cdot S \tag{3.6}$$

$$HgCl_2 + R \rightarrow P \tag{3.7}$$

$$HgCl_2 \cdot S + R \rightarrow P + S \tag{3.8}$$

If the uptake follows the Eley–Rideal mechanism, gaseous $HgCl_2$ reversibly adsorbs on S and reacts irreversibly with R independently of each other (Ammann et al., 2007; Pöschl et al., 2007). On the contrary, in the case of the Langmuir–Hinshelwood mechanism, $HgCl_2$ must adsorb onto an adsorptive site S first and only then the surface complex $HgCl_2 \cdot S$ can react with R, releasing S. The vacant site S can then adsorb another $HgCl_2$, and so the uptake would be limited by the availability of surface adsorptive sites,

S. The two mechanisms can be distinguished by studying the dependence of the uptake coefficient on the concentration of the gas-phase reactant (McCabe et al., 2009). Upon increasing the concentration, the uptake rate is expected to increase according to the Eley-Rideal mechanism, but decrease according to the Langmuir-Hinshelwood mechanism. Our experiments with varying $HgCl_2$ concentrations produced a clear decreasing trend in the initial uptake coefficient (Figure 3.9), supporting the two-step Langmuir-Hinshelwood mechanism.

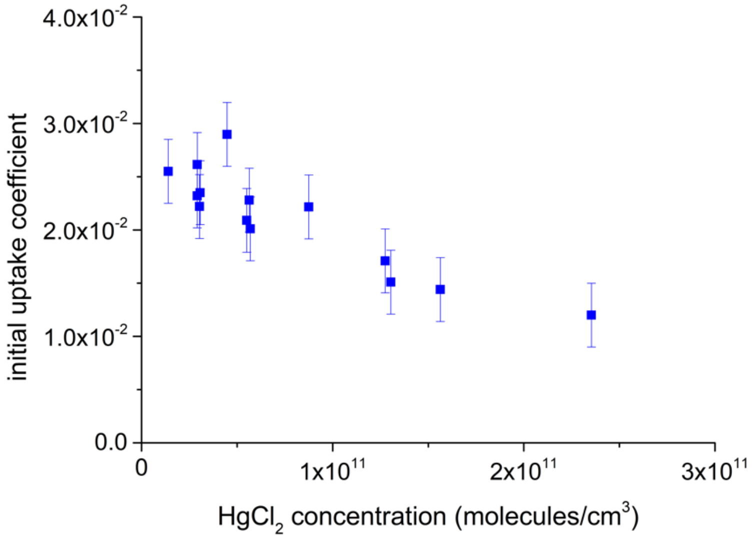

Figure 3.9 Dependence of the uptake coefficient on the gas-phase $HgCl_2$ concentration, using a NaCl surface. The exposure distance is 2 cm, the total pressure in the flow reactor is 1.94-2.00 Torr, and the temperature is 293 K.

This conclusion is further confirmed by the results obtained in a repeated uptake experiment (Figure 3.7). As follows from Equation (3.9), when the exposure of the salt surface to gas-phase $HgCl_2$ is terminated, the fate of $HgCl_2 \cdot S$ is determined by the competition between two processes: desorption (left arrow) and chemical reaction (right arrow).

$$\mathrm{HgCl_2 + S} \leftarrow \mathbf{HgCl_2{\cdot}S} \xrightarrow{+\mathrm{R}} \mathrm{P + S} \tag{3.9}$$

Under the Eley–Rideal mechanism, desorption occurs independently of the chemical reaction. Hence, the amount of $HgCl_2$ desorbed from the surface after terminating the exposure should remain unchanged with repeated exposures. However, Figure 3.7 indicates that the amount of desorbed $HgCl_2$ is higher with each subsequent exposure, although less gaseous $HgCl_2$ is taken. Such behavior is in agreement with the Langmuir-Hinshelwood mechanism, where increasing amounts of $HgCl_2$ are expected to desorb from the surface as it becomes less chemically reactive.

The effect of surface hydration. To look at the effect of water on the surface, we can change the level of hydration instead of using the aqueous surface directly because our fast flow reactor was operated at low pressure (~2 Torr). Gaseous $HgCl_2$ was exposed to the NaCl surface, either pristine or dehydrated by heating up to 118 ºC. When the dehydration was done in the oven, we did not see any difference in the uptake coefficient because the surface became hydrated once the sample got out of the oven. Hence we decided to heat the surface in the reactor at low pressure instead of in the oven to avoid re-hydration of the surface.

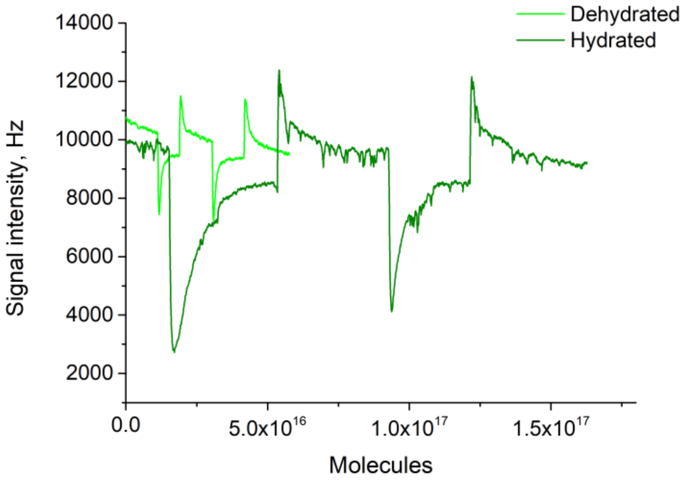

Figure 3.10 The uptake of $HgCl_2$ on a heated (up to 118 ºC) /unheated NaCl surface.

Figure 3.10 demonstrates the uptake of $HgCl_2$ on a hydrated/dehydrated NaCl surface. For the hydrated NaCl surface, the signal intensity dropped ~70% during the first uptake, whereas the signal intensity dropped ~25% for the first uptake in the case of the dehydrated NaCl surface. The signal intensity during the second uptake dropped ~60% and 25% for the hydrated surface and dehydrated surface of NaCl, respectively. Obviously, the existence of water impacts the uptake of $HgCl_2$ on the NaCl surface, which enables a more significant uptake. For the hydrated surface, we hypothesized that $HgCl_2$ dissolved in the hydrated NaCl surface and then reacted with Cl^- on the surface, leading to efficient uptake. In the case of the dehydrated NaCl surface, $HgCl_2$ coordinated via electrostatic binding with the Na^+ in the surface, which was reversible adsorption so that uptake remained the same during the first and second uptake.

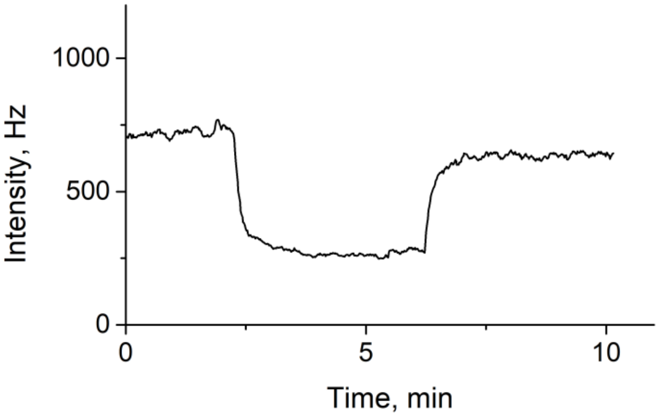

Figure 3.11 Uptake of $HgCl_2$ on the surface of ionic liquid (1-ethyl-3-methyl-imidazolium chloride). The exposure distance is 1 cm.

To verify our hypothesis in liquid that the uptake is not confined to the surface, we used ionic liquid, 1-ethyl-3-methyl-imidazolium chloride, as a surface. As shown in Figure 3.11, when $HgCl_2$ was exposed to 1 cm of the ionic liquid surface at 2 min, the $HgCl_2$ signal dropped significantly, the liquid continuously absorbed $HgCl_2$, and there was no signal recovery until we stopped $HgCl_2$ exposure to the surface at 6 min. That confirmed our hypothesis that the liquids would have almost infinite capacity to react with $HgCl_2$. Similar behavior of GOM uptake is expected in the aqueous solution in the atmosphere.

Reactivation of surface by humidification. Our experiments were conducted on solid salt surfaces in the reactor at 2 Torr, which is quite different from atmospheric conditions, where the relative humidity is sufficiently high to keep most inorganic salt particles deliquesced, or at least with several monolayers of water on their surfaces. In the atmosphere, we may expect that the reaction will not be confined only to the inorganic surface (Figure 3.12a), but rather the reactivity may remain nearly constant until all of the material in the particle reacts away (Figure 3.12b). To verify this hypothesis, we conducted repeated exposure experiments where the inorganic salt surface was treated to predefined levels of relative humidity between uptake runs. Figure 3.12d shows that the initial uptake coefficient on the fresh NaCl surface on the first exposure was 2.6×10^{-2}. Repeating the uptake experiment (exposure #2) produced a lower initial uptake coefficient ($\gamma_i = 1.5\times10^{-2}$) because most of the highly reactive and some of the less reactive sites were consumed (Figure 3.12a). Removing the coated tube from the reactor and treating it to a nitrogen flow maintained at a 33% relative humidity had a negligible effect on the reactivity because the deliquescence relative humidity of NaCl is 75% (Tang, 1996), and hence the salt surface remained crystalline. However, when this coated tube was later treated to 75% and 95% relative humidities, the initial uptake coefficient increased to 1.9×10^{-2} and 2.1×10^{-2}, respectively, nearly reaching the original level of unexposed NaCl. This increase in reactivity was caused by reactivation of the inorganic salt surface, which deliquesced upon humidification, turning into a liquid solution and dissolving the reaction product (Figure 3.12b). The change in the phase state from crystalline to liquid upon humidification was visually apparent, as the coating layer became nearly transparent. When the tube was re-dried, a nearly virgin reactive surface was produced (Figure 3.12c), restoring most of its reactivity.

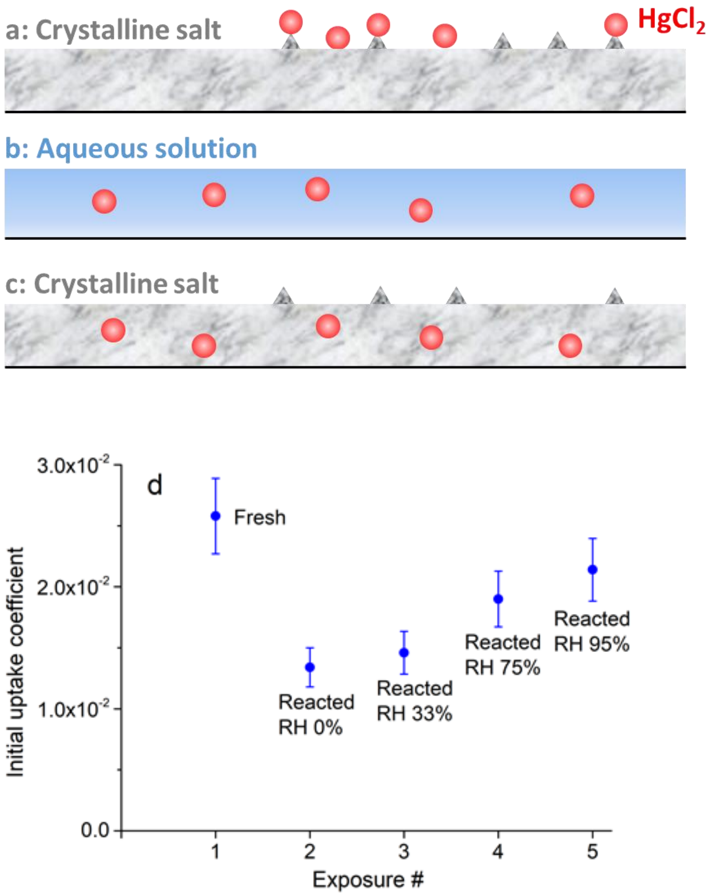

Figure 3.12 Partial reactivation of the NaCl surface achieved by cycling it through different levels of relative humidity: (a-c) schematic showing the mechanism of surface reactivation and (d) the dependence of the uptake coefficient on the maximum relative humidity (RH) experienced by the salt coating before the measurement.

Molecular-level reaction mechanism. The heterogeneous reaction of $HgCl_2$ with inorganic surfaces is a two-step Langmuir-Hinshelwood mechanism, adsorption/desorption and chemical reaction, where the reaction probability depends significantly on the salt anion, salt cation, and the level of surface hydration. Anions have high mobility on the surface in the presence of water, increasing the surface reactivity. There is also electrostatic binding between cation on the surface and halogen in the adsorbed $HgCl_2$. However, there is limited understanding of the effect of salt cations on surface reactivity. To explore the surface reaction mechanism, we investigated the interactions of different mercury halides (HgX_2, X = Cl, Br, I) with the NaCl surface using both experiments and molecular modeling. The scientific questions were: (1) why do salt cations affect the surface reactivity; (2) what is the effect of water on the surface reactivity; (3) what is the chemical state of $HgCl_2$ on the surface?

We are collaborating with Dr. Farnaz A Shakib to conduct computational studies of HgX_2 (X = Cl, Br, I) bind to a slab of NaCl, which is flat, using the CP2K method.

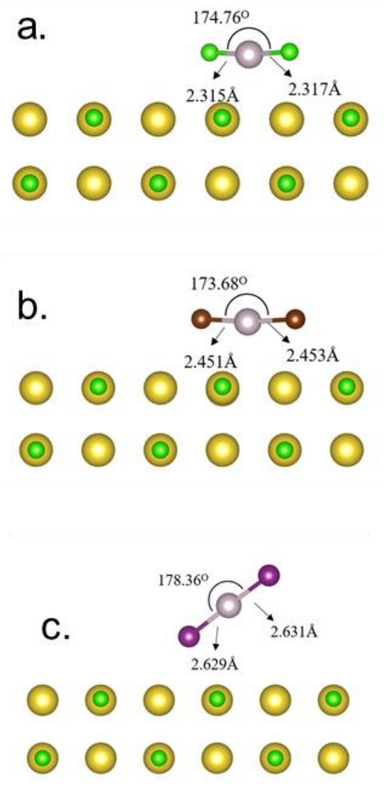

Figure 3. 13 Schematics of binding between a) $HgCl_2$; b) $HgBr_2$; c) HgI_2 molecules on a NaCl surface. Only part of the slab is shown.

As shown in Figure 3.13, gaseous HgX_2 (X = Cl, Br, and I) molecules approach the surface of NaCl and bind electrostatically with the surface at different angles and distances.

We varied mercury halides but used the same NaCl surface unit, as building a unit of the crystal structure is more complicated than changing molecules approaching the surfaces during the modeling. The binding energies of HgX_2 with NaCl surface and the average distance between Hg and halogens were calculated. The adsorption energy of HgX_2 (X = Cl, Br, and I) on the NaCl surface showed a linear correlation with the distance between Hg and Cl, Br, and I when HgX_2 bound to the surface (Figure 3.14). The adsorption energy for $HgCl_2$, $HgBr_2$, and HgI_2 were in decreasing order, where the distance between Hg and Cl, Br, and I increased because less adsorption energy was released to bind with the surface when the distance was longer.

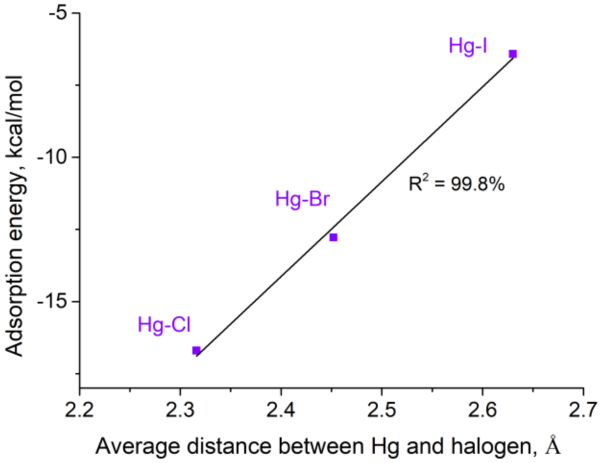

Figure 3.14 The dependence of adsorption energy of HgX_2 (X = Cl, Br, and I) on the average distance between Hg and halogens (Cl, Br, and I).

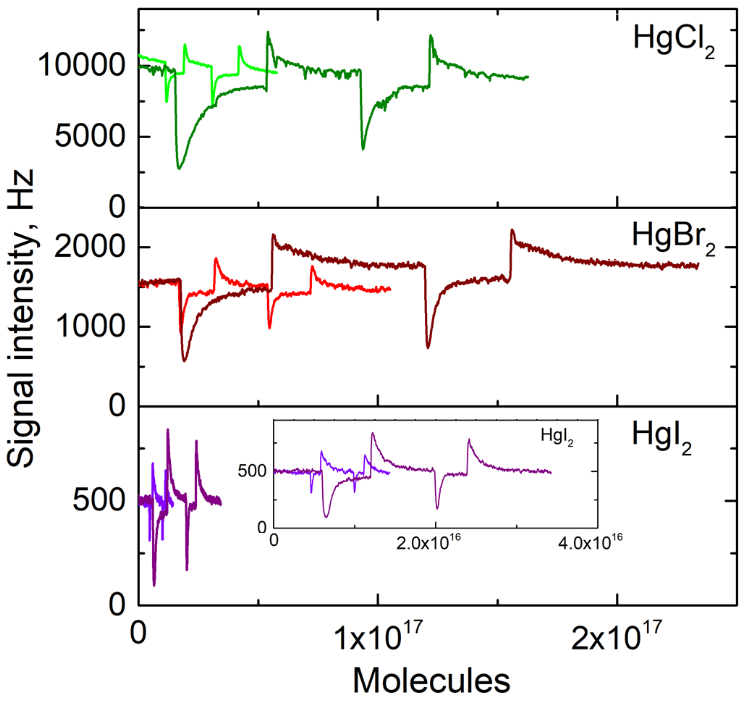

Figure 3.15 Uptake curves of mercury halides (HgX_2, X=Cl, Br, I) on dehydrated (light lines) and hydrated (dark lines) NaCl surfaces on the scale of the number of molecules exposed onto the surface.

The uptakes of $HgCl_2$, $HgBr_2$, and HgI_2 were measured on the hydrated and dehydrated surfaces of NaCl (Figure 3.15). All uptake curves showed a common behavior, where upon exposure the gas-phase concentration of HgX_2 dropped rapidly and then recovered gradually. However, the magnitude of the drop and the rate of recovery varied significantly between different mercury halides and different levels of hydration. The uptakes on dehydrated NaCl surfaces were nearly fully reversible for all gaseous mercury halides, with comparable uptake coefficients $(5.1\text{-}6.6)\times10^{-3}$, smaller than the uptake coefficients $(1.6\text{-}2.2)\times10^{-2}$ on the hydrated NaCl surfaces (Table 3.3).

Table 3.3 The Comparisons of Uptake Coefficients of HgX_2 (X=Cl, Br, I) on Hydrated and Dehydrated NaCl Surfaces

X	**Uptake coefficients (dehydrated)**		**Uptake coefficients (hydrated)**	
	1st uptake	**2nd uptake**	**1st uptake**	**2nd uptake**
Cl	6.0×10^{-3}	4.8×10^{-3}	1.6×10^{-2}	8.7×10^{-3}
Br	6.6×10^{-3}	6.0×10^{-3}	1.3×10^{-2}	1.1×10^{-2}
I	5.1×10^{-3}	4.5×10^{-3}	2.2×10^{-2}	1.5×10^{-2}

The uptake coefficients between different mercury halides on NaCl surfaces at the same condition (hydrated or dehydrated) were comparable, but the surface capacities varied significantly from $(0.28\text{-}3.7)\times10^{13}$ molecules/cm^2 for the dehydrated surface to $(0.25\text{-}4.1)\times10^{14}$ molecules/cm^2 for the hydrated surface (Table 3.4).

Table 3.4 The Comparisons of Surface Capacities of HgX_2 (X=Cl, Br, I) on Dehydrated and Hydrated NaCl Surfaces along with Their Calculated Adsorption Energy and Calculated Distances between Hg and X

Chemicals	**Surface capacity, molecules/cm^2**		**Adsorption energy, kcal/mol**	**Distance, Å**
	(Dehydrated)	**(Hydrated)**		
$HgCl_2$	3.7×10^{13}	4.1×10^{14}	-16.7	2.316
$HgBr_2$	2.6×10^{13}	1.6×10^{14}	-12.8	2.452
HgI_2	2.8×10^{12}	2.5×10^{13}	-6.4	2.630

The surface capacities for the dehydrated surface are almost one order of magnitude lower than the surface capacities on the hydrated surface for each gaseous mercury halide. For both hydrated and dehydrated surfaces, overall surface capacity increased in order $HgI_2 < HgBr_2 < HgCl_2$. The uptake of HgI_2 was the fastest to recover, with the lowest surface capacities of 2.5×10^{13} and 2.8×10^{12} molecules/cm^2 for the hydrated and dehydrated surfaces, respectively (Table 3.4). At the other end of the surface capacity was $HgCl_2$, with the slowest recovery of the signal, corresponding to capacities of 4.1×10^{14} and 3.7×10^{13} on dehydrated and hydrated surfaces, respectively. Table 3.4 summarizes the reacticity of mercury halides on the NaCl surface and compares them against theoretically calculated adsorption energies, which decreased from $HgCl_2$ (16.7 kcal/mol) to $HgBr_2$ (12.8 kcal/mol) and HgI_2 (6.4 kcal/mol) with decreasing surface capacities for both hydrated and dehydrated surfaces.

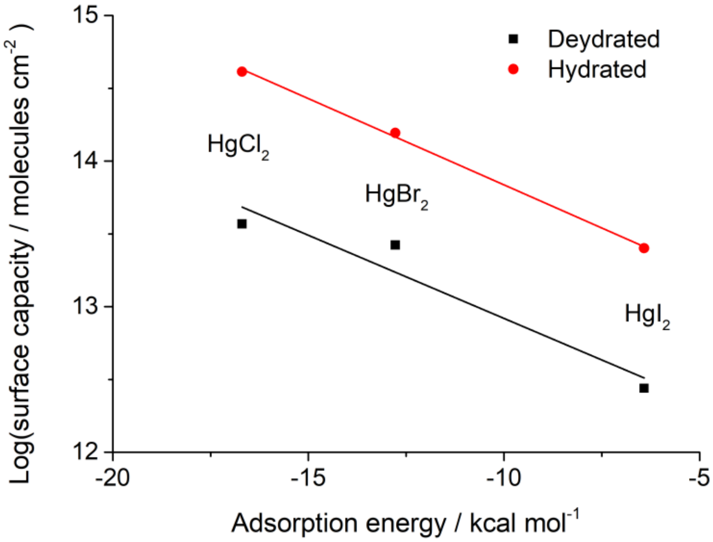

Figure 3.16 The comparisons of surface capacities of HgX_2 on hydrated and dehydrated NaCl surfaces along with calculated adsorption energy (dots). The lines are linear fits of the dependence of the logarithm of the surface capacity with adsorption energy, R^2 (red dots) = 0.99 and R^2 (black dots) = 0.81.

The logarithm of surface capacities versus adsorption energy of different mercury halides on hydrated/dehydrated surfaces is shown in Figure 3.16. In agreement with the thermodynamics, surface capacity fits exponentially with the calculated adsorption energy, indicating that the first step of reaction could be the hydration of the X-Hg-X molecule by the surface-bound water or even partitioning of X-Hg-X into the aqueous layer if the latter is sufficiently thick for the hydrated surface. On the contrary, on the dehydrated NaCl surface, the first reversible step of the L-H mechanism corresponds to the coordination of the negatively charged halide atoms in the X–Hg–X molecule with the positively charged sodium ions of the NaCl surface, and there is practically no second reactive step.

To verify the presence of Hg in the reacted NaCl surface and the chemical state of $HgCl_2$ on the surface, either as a reduced form (Hg^0) or as an oxidized form (Hg^{2+}), we conducted a series of experiments in collaboration with Dr. Andrew Teplyakov (University of Delaware) using X-ray photoelectron spectroscopy (XPS). XPS can determine the elemental composition as well as the chemical and electronic state of the atoms within a material. The basic principle of XPS is that when X-rays shoot on a sample material that absorbs energy, electrons from the top 1–10 nm of the material emerge from the sample with specific kinetic energy, producing spectra of each element. The potentials of transition metals having different oxidation states in solid and liquid oxides allow this technique for characterization, such as iron as Fe^{2+} and Fe^{3+}, manganese as Mn^{2+}, Mn^{3+}, and Mn^{4+}, chromium as Cr^{2+}, Cr^{3+}, and Cr^{6+}.

Our samples were prepared and shipped to the University of Delaware for XPS characterization. Samples of pure solid $HgCl_2$, solid $Hg(NO_3)_2$, and solid NaCl are commercially available. The sample of NaCl with adsorped $HgCl_2$ was prepared using a standard uptake experiment, where gaseous $HgCl_2$ with a concentration of 5.7×10^{10} molecules/cm^3 was exposed to NaCl surface for about 10 minutes, resulting in approximately 65% surface coverage.

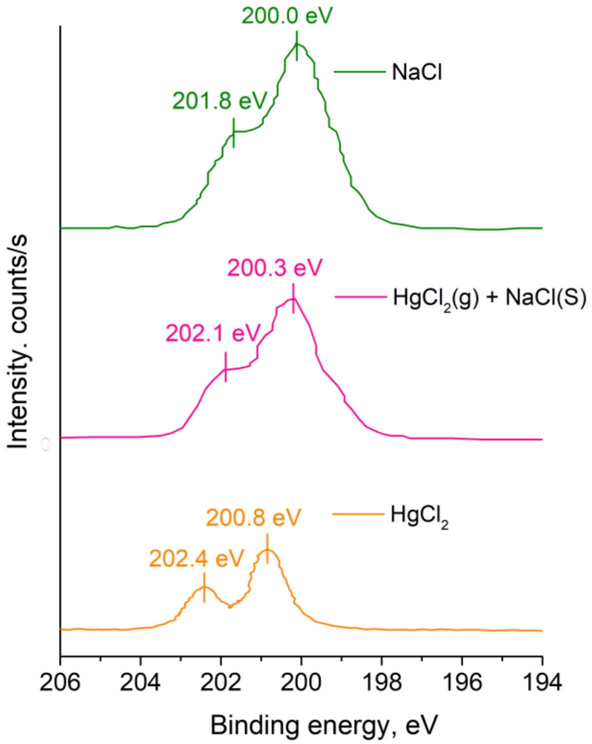

Figure 3.17 The XPS spectra of Cl 2p in solid NaCl, solid $HgCl_2$, and the NaCl surface with adsorbed gaseous $HgCl_2$.

The XPS spectra of Cl 2p in NaCl, $HgCl_2$, and the NaCl surface pretreated by gaseous $HgCl_2$ are shown in Figure 3.17. Explicit peaks at 200.8 and 202.4 eV for the $HgCl_2$ sample, at 200.0 and 201.8 eV for the solid NaCl sample, and at 200.3 and 202.1 eV for the reacted NaCl surface were detected. The Cl 2p peaks in NaCl and $HgCl_2$ were shifted towards each other, resulting in peaks at 200.3 and 202.1 eV. These peaks were assigned to Cl^- at $2p_{1/2}$ ("National Institute of Standards and Technology XPS database," 2012). The peak position depends on the ionic states of Cl, the ratio of the two distinct peak areas remains the same (1:2), which is consistent with the spin–orbit splitting theory for Cl 2p orbital.

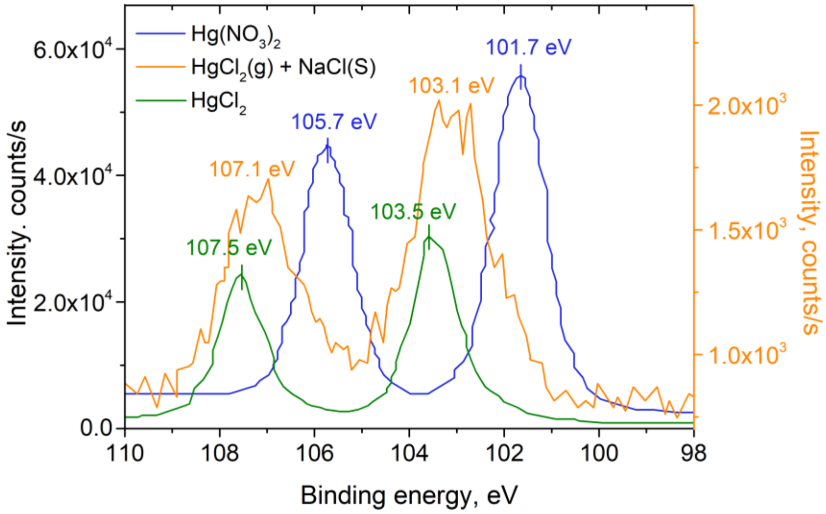

Figure 3.18 The XPS spectra of Hg 4f in solid $HgCl_2$ sample, in solid $Hg(NO_3)_2$ sample, and in gaseous $HgCl_2$ adsorbed on the NaCl surface. The blue and green lines belong to the left Y-axis, and the orange line is for the right Y-axis.

The XPS spectra of Hg 4f in covalent $HgCl_2$, in ionic $Hg(NO_3)_2$, and in $HgCl_2$ adsorped on the NaCl surface are shown in Figure 3.18, demonstrating the presence of Hg 4f in the reacted NaCl surface at 103.1 and 107.1 eV. These two peaks were consistent with 103.5 ($4f_{7/2}$) and 107.5 eV ($4f_{5/2}$) in the covalent $HgCl_2$ sample, but not Hg 4f in the ionic form $Hg(NO_3)_2$. The ratios of two peak areas in the reacted NaCl surface agree with the spin–orbit splitting theory for 4f orbital. The peaks for the ionic form of Hg in $Hg(NO_3)_2$ were 101.7 and 105.7 eV, and both peaks were assigned to Hg^{2+} (Jiang et al., 2020). There is no characteristic of Hg $4f_{7/2}$ at 99.9 eV for Hg^0 in the reacted surface. The $HgCl_2$ adsorbed onto the NaCl surface remained in its covalent form during the sampling, shipping, and detection by XPS till it got detected, so we can conclude that $HgCl_2$ was irreversibly adsorbed on the NaCl surface in the covalent form.

3.6 Heterogeneous Uptake of $HgCl_2$ on Carbonaceous Aerosol Surfaces

Removal by aerosols is an important intermediate step in the deposition of atmospheric gaseous oxidized mercury (GOM). Atmospheric aerosols contain both inorganic salts and a variety of carbonaceous/organic constituents. Here we report the uptake of GOM by surfaces mimicking carbonaceous aerosols of primary and secondary origin. Primary combustion aerosols were represented by soot, levoglucosan, and polycyclic aromatic hydrocarbons (PAHs perylene and pyrene). Secondary aerosols were represented by carboxylic acids (succinic, pimelic, and citric acid) and dioctyl sebacate (DOS). The gas-surface uptake was studied at 293 ± 2 K in a fast flow reactor coupled to an ion drift - chemical ionization mass spectrometer (ID-CIMS), using mercury (II) chloride ($HgCl_2$) as model GOM. The obtained kinetic data will help establish a more detailed mechanism of GOM removal by aerosol particles in atmospheric models.

3.6.1 Reactivities of Carbonaceous Surfaces

The uptake of $HgCl_2$ was measured on the surfaces of primary combustion (Figure 3.19) and secondary aerosols (Figure 3.20), using the coating mass of ~0.06 g. All uptake curves showed a typical behavior, where upon exposure the gas-phase concentration of $HgCl_2$ dropped rapidly and then recovered gradually. Within the similarity, the magnitude of the drop and the recovery rate varied significantly between soot and other organics.

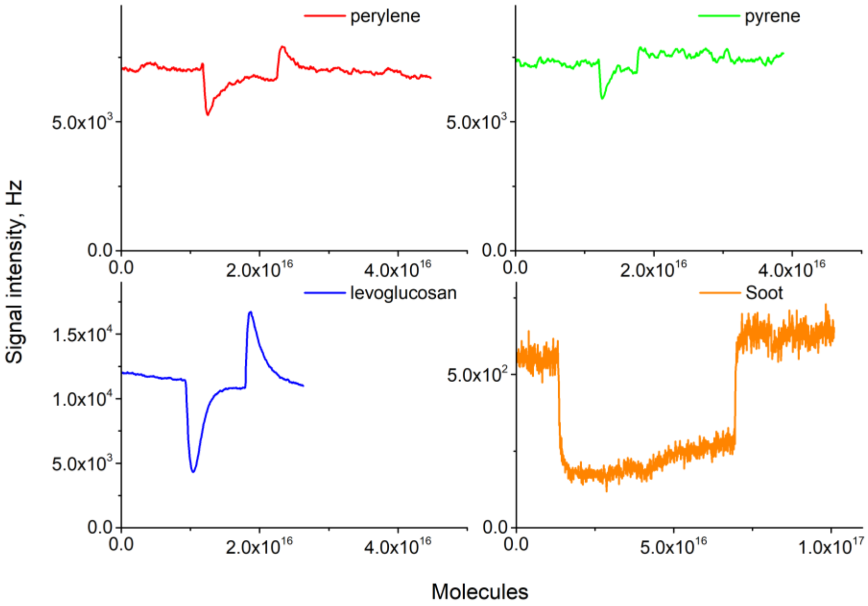

Figure 3.19 Uptake of $HgCl_2$ on surfaces of primary aerosol surrogates. The exposure distance for soot is 2 cm, and others are 5 cm.

Among four surfaces of primary aerosols origin, soot has the most lasting drop of signal but the lowest uptake coefficient (1.2×10^{-4}), which was calculated using its BET surface area (~79 m^2/g) (Khalizov et al., 2010). Uptake coefficients and surface capacities for other organics were calculated based on their geometric surface areas. Within four surfaces representing primary aerosols, levoglucosan was the most reactive surface, with reactivity comparable to ammonium sulfate in Section 3.5.2. In the case of PAHs, pyrene and perylene showed some uptake, corresponding to uptake coefficients of 2.1×10^{-3} and 3.0×10^{-3}. In terms of surface capacity, perylene had ~20 times higher surface capacity than pyrene for the uptake of $HgCl_2$

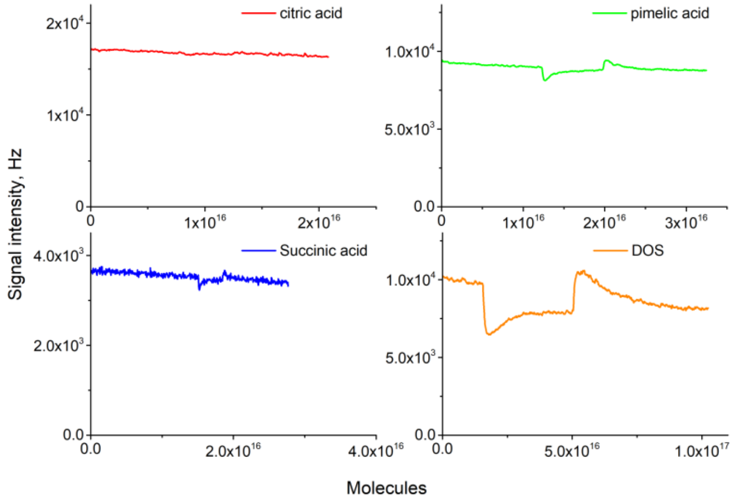

Figure 3.20 Uptake of $HgCl_2$ on organic surfaces of secondary aerosol surrogates. The exposure distance for DOS is 1 cm, other organic acids are 5 cm.

Figure 3.20 shows the uptake curves of $HgCl_2$ on the surfaces of secondary aerosol representatives. The uptake of $HgCl_2$ on the surface coated with citric acid was almost non-detectable, giving less than the detectable values of the uptake coefficient ($<1.2\times10^{-4}$), which was calculated based on the signal error. On the other hand, DOS corresponded to the highest uptake coefficient (2.6×10^{-2}) and surface capacity (5.8×10^{15}). DOS is liquid at room temperature and acts as a liquid layer whose behavior was described in Section 3.5.3. The uptake of $HgCl_2$ on three undissociated acids is in the order of pimelic acid > succinic acid > citric acid.

The overall reactivity varied significantly between different surfaces, with uptake probability decreasing from 2.6×10^{-2} to 1.2×10^{-4} in the series: DOS > levoglucosan > perylene > pyrene > undissociated organic acids (pimelic acid > succinic acid) > soot > undissociated citric acid, as shown by the values of the uptake coefficients along with surface capacities given in Table 3.5.

Table 3.5 Uptake Coefficients and Surface Capacities for Organics

Chemicals	Chemical structure	Uptake coefficient	Surface capacity, molecules/cm^2
Levoglucosan	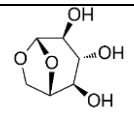	1.1×10^{-2}	4.8×10^{13}
Pyrene	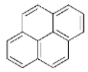	2.1×10^{-3}	8.0×10^{11}
Perylene	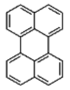	3.0×10^{-3}	1.6×10^{13}
Soot [a]		1.2×10^{-4}	1.4×10^{13}
Citric acid	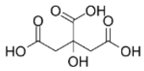	$< 1.2\times10^{-4}$, [c]	- [b]
Pimelic acid	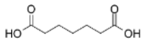	1.1×10^{-3}	- [b]
Succinic acid	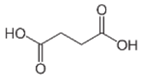	9.3×10^{-4}	- [b]
DOS [d]	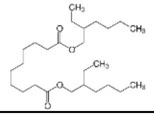	2.6×10^{-2}	5.8×10^{15}

[a] Calculation of soot used BET surface area; others used geometric surface area upon 5 cm exposure distance
[b] Too small for accurate evaluation
[c] The number is calculated based on the error of the measurement
[d] DOS: 1 cm exposure distance

In some cases, the reaction time had to be varied by changing the velocity of the gas flow or exposed length of the salt surface to improve measurement accuracy, e.g., the exposed length was reduced to 1 cm when using the most reactive DOS, the exposure distance for soot was 2 cm. Previous studies have reported that carboxylic acids could bind with metal ions such as Hg(II), and the sorption capability of metal ions would be varied by changing the carboxylic groups (Kılıç et al., 2008; Lin & Pehkonen, 1999; Zhang et al., 2006). Succinic acid and pimelic acid hold two carboxylic groups had comparable uptake coefficients, which were ten times larger than citric acid with three carboxylic groups, where the intermolecular hydrogen bonds may form (Table 3.5). The binding of Hg(II) with humic substances has been reported as pH-dependent (Matthiessen, 1996; Matthiessen, 1998), we hypothesized that the uptake of $HgCl_2$ by carboxylic acids was also pH-dependent.

3.6.2 The pH Dependence of Reactivity of Organic Acid Surfaces

Many studies have shown that the reactive uptake of atmospheric gases, such as isoprene and primary organic aerosols, is influenced by the acidity of aerosols particles (Jang et al., 2002; Limbeck et al., 2003; Surratt et al., 2007). The pH of aerosol particles is determined by their compositions, locations, seasons, and the particles' size (Pye et al., 2020; Song et al., 2018). Up to 64% of the adicity in atmospheric precipitation is contributed by carboxylic acids which are mainly produced from the oxidation of olefins and other volatile organic compounds in the atmosphere and combustion sources (Keene et al., 1983). The protonation states of acids are proportional to the pH, where carboxylic acids would deprotonate and become more soluble at higher pH (Chowhan, 1978; Křůmal et al., 2009). To test the influence of the carboxylic acids with short chains ($C \leq 5$) and different numbers of carboxylic acid groups in various degrees of dissociation on the reactivities towards $HgCl_2$, we performed a series of uptake experiments using surfaces made of citric acid, pimelic acid, and succinic acid. The pH was adjusted according to the dissociation constant, K_a, which is expressed commonly in pK_a=-log K_a, and measured in the solution, which then was applied onto a frosted glass tube and dried as described earlier in Section 3.3.1.

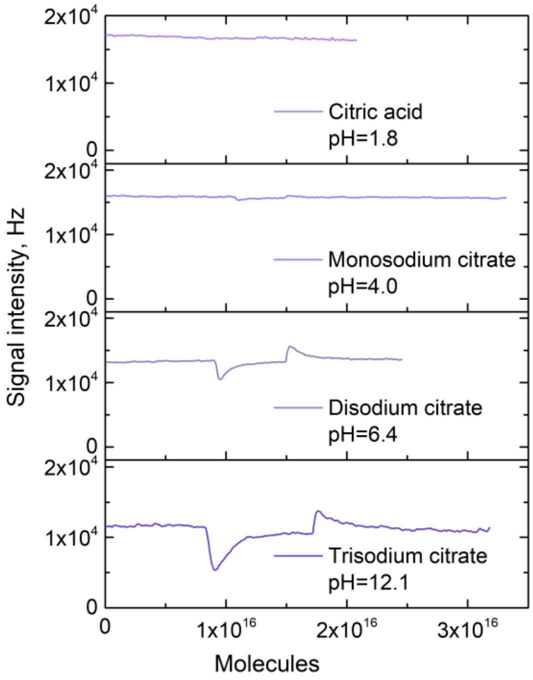

Figure 3.21 Uptake of gas-phase $HgCl_2$ on citric acid, monosodium citrate, disodium citrate, and trisodium citrate surfaces (RH=5%), where the pH values were obtained in aqueous solutions.

Figure 3.21 shows the uptake curves of gas-phase $HgCl_2$ on citric acid, monosodium citrate, disodium citrate, and trisodium citrate surfaces. The uptake curves demonstrated that the uptakes of $HgCl_2$ would increase gradually from nearly no uptake to significant uptake with increasing pH from 1.8 to 4.0, 6.4, and 12.1, which was associated with the deprotonation degree. As pH increased, the citric acid deprotonated, the binding between deprotonated carboxylic groups on the surfaces and gaseous $HgCl_2$ increased as well, in agreement with a previous study of the adsorption of Hg(II) enhanced by citric acid at different pH levels (Singh et al., 1996).

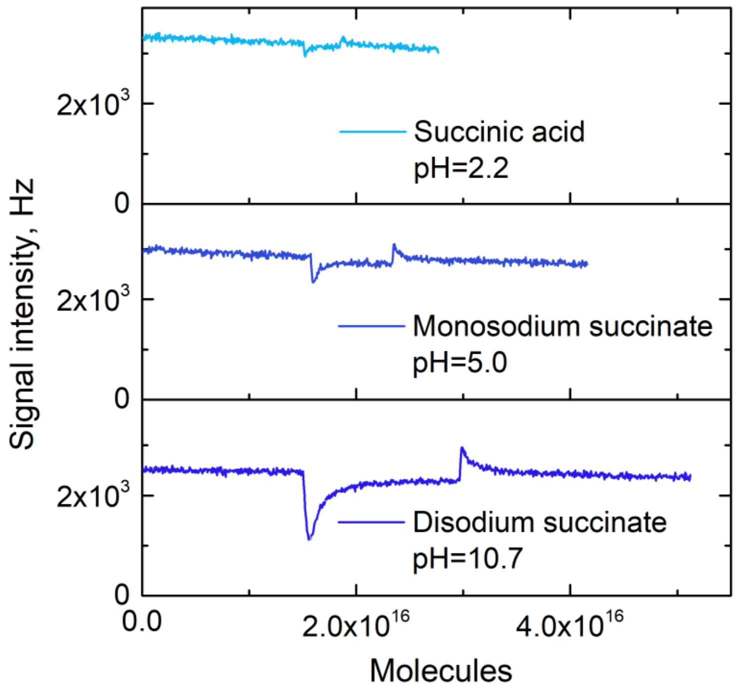

Figure 3.22 Uptake of gas-phase $HgCl_2$ on succinic acid, monosodium succinate, and disodium succinate surfaces (RH=5%), where the pH values were obtained in aqueous solutions.

Uptake curves for succinic acid and pimelic acid surfaces at different pH levels are shown in Figures 3.22 and 3.23. They both have two carboxylic groups and comparable pKa values, resulting in nearly the same uptake of $HgCl_2$ at the same deprotonated forms. The pH-dependent uptake was probably due to the deprotonated carboxylic groups and the coordination between $HgCl_2$ and the carboxylic groups.

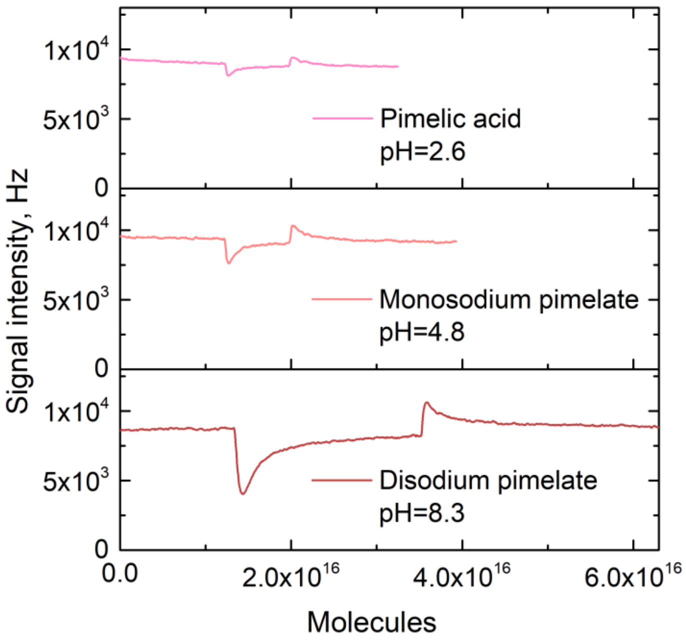

Figure 3.23 Uptake of gas-phase $HgCl_2$ on pimelic acid, monosodium pimelate, and disodium pimelate surfaces (RH=5%), where the pH values were obtained in aqueous solutions.

Table 3.6 shows that both uptake coefficients and surface capacities for these three individual acids increased significantly with the pH chosen based on the pK_a values. Among these three acids, pimelic acid had the largest uptake coefficient (1.1×10^{-3}), whereas the uptake coefficient of citric acid is almost negligible, in agreement with their uptake curves. In fully deprotonated forms, these three carboxylic acids had comparable uptake coefficients ($\sim8\times10^{-3}$) and significant differentiation in surface capacities (from 2.9×10^{13} to 6.4×10^{14} molecules/cm^2). There is a need for a more basic environment for citric acid with three carboxylic groups than other acids with only two carboxylic groups to achieve the same uptake coefficient ($\sim2\times10^{-3}$).

Table 3.6 Uptake Coefficients and Surface Capacities for Organic Acids with Different pH

	pK_a	pH	Uptake coefficient	Surface capacity, molecules/cm^2
Citric acid		1.8	$< 1.2\times10^{-4}$, [a]	- [b]
Monosodium citrate	3.13 (pK_{a1})	4	6.9×10^{-5}	1.0×10^{12}
Disodium citrate	4.76 (pK_{a2})	6.5	2.4×10^{-3}	4.8×10^{12}
Trisodium citrate	11.6 (pK_{a3})	12.1	8.4×10^{-3}	2.9×10^{13}
Pimelic acid		2.6	1.1×10^{-3}	- [b]
Monosodium pimelate	4.49 (pK_{a1})	4.8	2.2×10^{-3}	4.6×10^{12}
Disodium pimelate	5.43 (pK_{a2})	8.3	8.2×10^{-3}	6.1×10^{13}
Succinic acid		2	9.3×10^{-4}	- [b]
Monosodium succinate	4.21 (pK_{a1})	5	2.0×10^{-3}	- [b]
Disodium succinate	5.64 (pK_{a2})	10.7	8.3×10^{-3}	6.4×10^{14}

[a] The number is calculated based on the error of the measurement

[b] No visible change

[c] The pK_a values of the diacids are available for citric acid, succinic acid, and pimelic acid at ionic strength zero

Source: (Martell et al., 1974)

3.7 Atmospheric Implications

We used the $HgCl_2$ uptake coefficients obtained in our study to estimate the lifetime of GOM with respect to removal by atmospheric particles, assuming that particle reactivity could be represented by individual constituents: for inorganics, ammonium sulfate and sodium chloride, which contribute 30-50% and 98-99% of the particle mass in urban (Heintzenberg, 1989; Jimenez et al., 2009) and marine (Athanasopoulou et al., 2008; Day, 2014) environments, respectively; for organics, soot, levoglucosan, PAHs and organic acids represent primary and secondary organic aerosols, respectively. We also assumed that the reactivity of $HgCl_2$ with these salts in multicomponent particles is unaffected by other particle constituents. This simplification is necessary due to lack of uptake data for organic and mixed composition surfaces, which are representative of atmospheric aerosols (Jimenez et al., 2009). We used initial uptake coefficients γ_i because the particle surface coverage by GOM molecules is expected to remain low over the entire aerosol lifetime. Indeed, considering typical atmospheric concentrations of GOM (~10^5 molecules cm^{-3}) and aerosol surface area (10^{-7}–10^{-6} cm^2 cm^{-3}), surface coverage after complete consumption of GOM would not exceed 0.1–0.01%, and hence the reactivity of particles will remain nearly unchanged. Although the concentration of $HgCl_2$ in our experiments was significantly higher than that of atmospheric GOM, the use of experimental uptake coefficients for atmospheric lifetime evaluations is still appropriate. Not only gas-surface uptake is a first-order process with respect to GOM, but also in all experiments measuring the initial uptake, the surface coverage remained below few percent, resulting in a relatively shallow concentration dependence. Hence, extrapolating towards the zero $HgCl_2$ concentration would not significantly change the value of γ_i.

The lifetime (Ammann et al., 1998) of GOM was estimated using Equation (3.11a), which was adopted based on the equation for the gas-particle mass-transfer coefficient introduced in previous work (Holmes et al., 2009; Sander, 1999; Schwartz, 1986),

$$\tau = \left[\sum 4\pi r^2 \left(\frac{\Delta N}{\Delta \log r}\right) \Delta \log r \left(\frac{r}{D_g} + \frac{4}{\gamma_{\mathrm{i}} \omega_{GOM}}\right)\right]^{-1} \tag{3.11a}$$

this equation accounts for both interfacial and diffusion-limited mass-transport, corresponding roughly to submicron and supermicron aerosol particles, respectively. The summation is over the binned particle size distribution, $\Delta N/\Delta \log r$. The term $4\pi r^2 \Delta N$ corresponds to the surface area concentration (Ammann et al., 1998) of aerosol particles of a radius r. The mean thermal velocity and diffusivity of GOM in air were taken as

ω_{GOM}=1.5×10^4 cm s^{-1} and D_g=0.1 cm^2 s^{-1}, respectively, following the modeling study of Holmes et al. (2009)

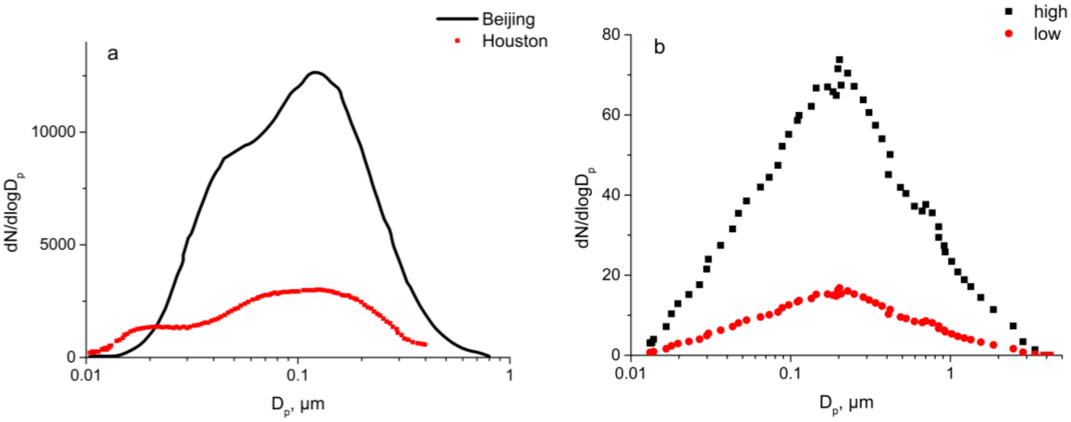

Figure 3.24 Scaled particle size distributions: (a) urban aerosols in Houston, TX (red) and Beijing, China (black); (b) marine aerosols of a lower (red) and higher (black) concentration.

Sources for (a) (Cheng et al., 2009; Levy et al., 2013) and for (b) (Quinn et al., 2015).

Table 3.7 Particle Number, Surface, and Mass Concentration, along with Calculated GOM Lifetimes Corresponding to Different Scenarios (Urban and Marine, Lower and Higher Aerosol Loading)

Scenario	Number concentration, cm^{-3}	Surface concentration, μm^2 cm^{-3}	Mass concentration, μg m^{-3}	GOM lifetime, hr
Houston, TX	2.9×10^3	163	12.7	2.1
Beijing, China	10.6×10^3	815	82.5	0.4
Sea salt (low)	19.0	18.8	10.2	19.0
Sea salt (high)	83.5	82.4	44.9	4.3

For urban aerosol, we selected moderately polluted (Houston, TX) (Levy et al., 2013) and highly polluted (Beijing, China) (Cheng et al., 2009) scenarios with average particle mass concentrations of 12.7 and 82.5 µg m^{-3} (Jimenez et al., 2009). The size distributions from Levy et al. (2013) and Cheng et al. (2009) were scaled to obtain the target mass concentrations (Figure 3.24a), using a 1.55 g cm^{-3} particle density, which corresponds to a mixture of ammonium sulfate, organics, and other minor constituents (Levy et al., 2013). At both locations, the particle mass fraction of $(NH_4)_2SO_4$ was ~50% (Jimenez et al., 2009). For marine aerosol, we selected low (3 m s^{-1}) and moderate (15 m s^{-1}) wind velocity scenarios, corresponding to globally averaged 10 and 45 μg m^{-3} sea salt aerosol mass concentrations, respectively (Lewis et al., 2004). The size distribution of sea salt was taken from Quinn et al. (2015) and scaled to obtain the target mass concentrations (Figure 3.24b). The input parameters used in calculations are summarized in Table 3.7 along with the resulting GOM lifetimes, which range between 0.4 – 2.1 hours for $(NH_4)_2SO_4$ and 4.3 – 19 hours for NaCl. Based on these values, we conclude that urban aerosols may represent a major sink of GOM. Furthermore, even dry sea salt aerosols, alongside deliquesced sea salt droplets, may contribute to the rapid loss of GOM in marine environment, as proposed in modeling and field studies (Holmes et al., 2009; Laurier et al., 2007; Laurier, 2003; Selin et al., 2007). Our measured uptake coefficients can be used to account for GOM removal by effloresced particles in atmospheric models and also in evaluating the efficiency of salt-coated denuders.

For primary organic aerosol, we selected a highly polluted (Beijing, China) scenario for levoglucosan and soot with average particle mass concentrations of 3.3 and 7.6 μg m^{-3} as representatives (Sun et al., 2016), corresponding to GOM lifetime of 1 day and 13 days, respectively. For the secondary organic aerosols, we used succinic acid with an average mass concentration of 0.5 μg m^{-3} (Fresno, CA) as an example to calculate GOM lifetime (Ge et al., 2012), which varied from 68 days to 8 days as pH increased from 2 to 10.7.

Assuming the aerosol particle diameters are 0.4 μm, the lifetime was calculated using Equation (3.11b),

$$\tau = \frac{4}{\gamma_i \omega_{GOM} n_s} \tag{3.11b}$$

where n_s represents the total surface area of aerosol particles. The input parameters used in calculations are summarized in Table 3.8 and the resulting GOM lifetimes, which range between 1 – 13 days for primary organic aerosols and 8 – 68 days for secondary organic aerosols at different pHs. Based on these values, we conclude that the role of organic acids in the removal of GOM will be highly dependent on particle acidity, increasing on going from urban to marine aerosols. Compared with our previous kinetic data on dry marine and urban aerosol surfaces (lifetime varies from half an hour to a day), we conclude that carbonaceous aerosols are less important for GOM removal. Further research should focus on the interaction of $HgCl_2$ with surfaces made of mixtures of inorganics and organics to better quantify the contribution of multicomponent atmospheric aerosols to GOM removal.

Table 3.8 Lifetime Estimations of $HgCl_2$ on the Surfaces of Primary and Secondary Carbonaceous Aerosol Surrogates, Assuming Aerosol Particle Diameters are 0.4 μm

Surface	Number concentration, cm^{-3}	Surface concentration, $\mu m^2\ cm^{-3}$	Mass concentration, $\mu g\ m^{-3}$	GOM lifetime, day
Succinic acid	9.6	4.8	0.5	68
Disodium succinate	9.6	4.8	0.5	8
Levoglucosan	58	29.3	3.3	1
Soot	113	57.0	7.6	13

CHAPTER 4

EXCHANGE REACTIONS OF GASEOUS OXIDIZED MERCURY ON SURFACES

4.1 Introduction

To predict the transport and deposition of mercury in the atmosphere, the knowledge of its speciation and chemical mechanisms is paramount. This need has led to a steady stream of field, laboratory, and computational studies, whose number increased every time a critical discovery was made, such as the observation of the fast mercury depletion events in ground Arctic air upon Polar sunrise (Schroeder et al., 1998a) or ruling out the direct gas-phase oxidation of GEM by atmospheric ozone (Calvert & Lindberg, 2005; Shepler et al., 2003; Tossell, 2003). However, despite the intense research, our knowledge of *molecular* speciation of mercury and its *chemical* mechanisms in the atmosphere is still limited and based primarily on the results of computational studies, and to a lesser extent on experimental work. We now know that the oxidation of GEM is initiated by free radicals, most probably by atomic bromine, as shown in experimental (Ariya et al., 2002; Donohoue et al., 2006), theoretical (Balabanov et al., 2003; Cremer et al., 2008; Dibble et al., 2012; Goodsite et al., 2004; Khalizov et al., 2003; Shepler et al., 2007), and modeling (Holmes et al., 2010; Holmes et al., 2006) studies. The resulting HgBr radical is relatively short-lived and must be stabilized via reactions with atmospheric species that are sufficiently reactive yet abundant, such as NO_2 and HO_2, forming gaseous oxidized mercury (GOM) molecules like BrHgONO and BrHgOOH (Jiao & Dibble, 2015, 2017b; Lam et al., 2019a; Shepler et al., 2007). Recently, the first experimental study of the HgBr + NO_2 reaction kinetics has been reported (Wu et al., 2020), and future experiments must focus on measuring accurate rate constants and identifying reaction intermediates and products (Jaffe et al., 2014). Meanwhile, the major focus of field studies has been to improve the limit of detection, accuracy, and temporal resolution of methods for the quantification of different forms of mercury in the atmosphere (Jaffe et al., 2014). By necessity, those forms are operationally defined even today, including GEM, GOM, particle bound mercury (PBM), reactive mercury (RM = GOM + PBM), and total gaseous mercury (TGM = GEM + RM), but recently there have been efforts to establish molecular speciation of those operationally defined forms.

The analytical techniques described in the introduction speciate atmospheric mercury only operationally, where the principal difference between the individual species is either the oxidation state (e.g., GEM versus GOM) or phase state (e.g., GOM versus PBM), and with some notable exceptions they are unable to provide any molecular (or chemical) speciation. One such exception involves the use of nylon membranes in RMAS (Lyman et al., 2020c). Although inferior to CEM in collection efficiency (Huang et al., 2015), nylon membranes can be thermally desorbed without interfering with CVAFS analysis, providing an opportunity to get a glimpse of the chemical speciation of GOM and RM (Huang et al., 2013). Using temperature programming with subsequent pyrolysis of the thermally evolving GOM and by detecting it as GEM, this method relies on the characteristic peak desorption temperatures of the atmospheric sample, comparing them against a set of standards through a deconvolution procedure. It is assumed that the collected GOM can be represented by a set of commercially available chemicals (such as $HgBr_2$, $HgCl_2$, HgO, $Hg(NO_3)_2$, $HgSO_4$, and CH_3HgCl), which is a major limitation. Thus, there have been attempts to exclude pyrolysis and use mass spectrometry instead to analyze the gaseous chemicals evolving during thermal desorption (Deeds et al., 2015; Jones et al., 2016). For instance, Deeds et al (Deeds et al., 2015) were able to detect $HgCl_2$ and $HgBr_2$ in laboratory samples, using a commercial atmospheric pressure chemical ionization mass spectrometer, but they observed a significant interference due to co-adsorbed contaminants in atmospheric samples. Similarly, Jones et al (Jones et al., 2016) using gas chromatography with cryo-focusing and mass spectrometry detection, were able to show the presence of $HgCl_2$ and $HgBr_2$ in laboratory samples, but not RM in atmospheric samples. Notably, in both studies, HgBrCl has been detected and its formation was rationalized by two different mechanisms: exchange in solution / on quartz wool surface (Jones et al., 2016) versus an artifact of chemical ionization (Deeds et al., 2015). Failure to detect any chemicals other than the volatile mercury (II) halides raises two crucial questions: (1) Are atmospheric GOM molecules sufficiently stable and volatile to be thermally desorbed from adsorbents? (2) Do these molecules maintain their original chemical form on adsorbents against possible reactions with other GOM molecules, co-adsorbed non-mercury species, and adsorbent surfaces?

Our major goal was to investigate the exchange reactions occurring *on surfaces* during interaction with different *gaseous* GOM (Figure 4.1c), but we began our study by first considering a set of simpler cases, including exchange reactions in *aqueous solutions* (Figure 4.1a) and exchange reactions between *gaseous* chemicals and *surface-bound* chemicals (Figure 4.1b). As appropriate, reaction products formed in these systems were analyzed in solid phase (Raman spectroscopy), aqueous phase (ESI-MS), and gaseous phase (ID-CIMS). The principle questions our study aimed to address were: can volatilizable mercuric compounds form during the interactions between (1) different *covalent mercuric* compounds (e.g., $HgCl_2$ and $HgBr_2$), (2) a *covalent mercuric* compound and an *ionic non-mercury* compound (e.g., $HgBr_2$ and HCl or KCl), and (3) an *ionic mercuric* compound and an *ionic non-mercury* compound (e.g., $Hg(NO_3)_2$ and KCl). If occurring, either on aerosols in the atmosphere or on substrates upon collection and analysis, such reactions would scramble the original chemical composition of GOM formed during the photochemical oxidation of GEM in the atmosphere.

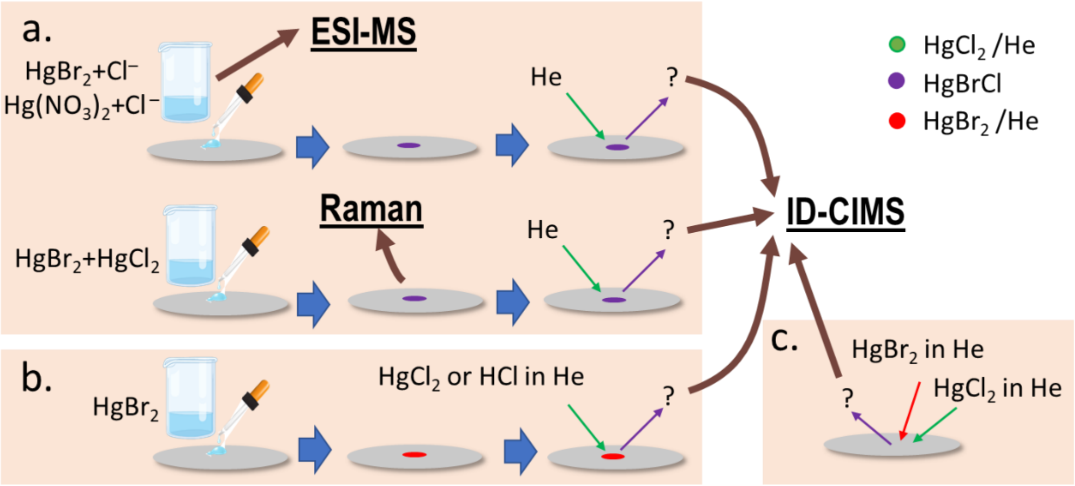

Figure 4.1 The overall approach and detection methods used to study exchange reactions: (a) reactions of $HgBr_2$ and $Hg(NO_3)_2$ with $HgCl_2$ and Cl^- in aqueous solution, (b) reactions of gaseous $HgCl_2$ and HCl with the surface-bound $HgBr_2$, and (c) reaction of gaseous $HgCl_2$ and $HgBr_2$ in the presence of different surfaces.

4.2 Experimental

We used commercial mercuric chloride ($HgCl_2$, Honeywell, >99.5%), mercuric bromide ($HgBr_2$, Sigma Aldrich, >99.0%), and mercuric nitrate monohydrate ($Hg(NO_3)_2 \cdot H_2O$, Sigma Aldrich, >98.0%) as proxies for GOM. Ammonium chloride (NH_4Cl, Supelco, ≥99.8%), potassium chloride (KCl, Acros Organics, >99%), and hydrogen chloride (HCl, Sigma-Aldrich, 37%) served as non-mercury co-adsorbing chemicals or substrates. Polyethersulfone cation exchange membranes (PES, Cole-Parmer, 90 mm Diameter, pore size of 0.45 μm), nylon membranes (Cole-Parmer, 90 mm Diameter, pore size of 0.45 μm), and the deactivated borosilicate glass (Pyrex) were used as surfaces. Cation exchange membranes (CEM) and nylon membranes trap GOM with high efficiency and are thus commonly utilized in field studies as collection substrates (Dunham-Cheatham et al., 2020; Gustin et al., 2019; Marusczak et al., 2017). On the contrary, the smooth surface of the borosilicate glass is relatively inert towards $HgCl_2$ (Mao et al., 2021). In our experiments, the glass was deactivated with dimethyldichlorosilane (DMDC, Sigma-Aldrich, ≥98.5%), as described previously (Mao et al., 2021).

Aqueous solutions of $HgCl_2$ (140 mM), $HgBr_2$ (16 mM), $Hg(NO_3)_2 \cdot H_2O$ (16 mM), KCl (33 mM), and NH_4Cl (1.2 mM) were prepared by dissolving the corresponding solids in distilled water. The 6% HCl solution was prepared by diluting the concentrated HCl with distilled water. The HgBrCl solution (32 mM) was prepared by mixing aqueous $HgCl_2$ and $HgBr_2$ in a 1:1 molar ratio, and a crystalline HgBrCl was obtained by evaporating this solution. Surfaces were either pretreated with various chemicals by applying a small aliquot (0.1 mL) of solution and then drying (CEM/nylon membranes and frosted borosilicate glass) or directly exposed to gas-phase chemicals in situ (CEM/nylon membranes, deactivated borosilicate glass, and PTFE). Gaseous $HgCl_2$ and $HgBr_2$ were introduced in a flow of helium from glass injectors. An injector was a 0.25-inch outer diameter borosilicate tube with a 5-cm-long column of crystalline powder of the corresponding mercuric halide packed between two plugs of deactivated glass wool (Khalizov et al., 2020; Mao et al., 2021). Gaseous HCl was introduced in a flow of helium from a vial equipped with a PTFE stopcock and containing 6% HCl solution in water.

4.2.1 Analysis of Solid Samples

Solid samples were analyzed by Raman microscopy, using a high-resolution confocal dispersive DXRxi Raman Microscope (Thermo Scientific). A slide holding a small amount of the solid sample was placed on a high-precision motorized stage under the 10× or 50× microscopic objective. After testing various magnification levels, we collected Raman spectra at 1 cm^{-1} per CCD pixel resolution using high-resolution grating (range 50-1800 cm^{-1}). The samples were excited by a diode-pumped solid state (DPSS) laser with a 532 nm wavelength, using a 5.0-10.0 mW laser power. The spectral acquisition time was 5−50 s, depending on the signal strength.

4.2.2 Analysis in Solutions

Solutions were analyzed by Electrospray Ionization Mass Spectrometry (ESI-MS), using a TSQ Quantum Classic triple-quadrupole mass spectrometer (Thermo Scientific) equipped with an ESI source. Samples (e.g., 44 μM $HgBr_2$ and 30 μM $Hg(NO_3)_2$) were spiked with NH_4Cl (1.2 mM), injected with a syringe (Hamilton, 50 μL) into a 10 μL sample loop connected to a multi-port valve, and then flushed into the ESI capillary continuously with a flow of solvent (3 μL/min, methanol:water = 50:50, 1.2 mM NH_4Cl) delivered by a programmable syringe pump (New Era, syringe volume 5 mL). The analysis was performed in the negative ion mode, using spray voltage of -3 kV, nitrogen sheath of 2 relative units (supply pressure 90 psi), ion transfer tube temperature of 270 ºC, mass spectral resolution of 0.7 amu, and a typical scan range of 290-400 amu.

4.2.3 Analysis in Gas Phase

Volatile mercury compounds were analyzed in the gas phase using the Ion Drift - Chemical Ionization Mass Spectrometry (ID-CIMS) (Fortner et al., 2004; Khalizov et al., 2020). In ID-CIMS, neutral molecules are converted to ions through ion-molecule reactions in a drift tube and then detected using an Extrel CMS quadrupole mass spectrometer equipped with a counting electron multiplier. In this study, the reagent ion was SF_6^-, produced by corona discharge in N_2 spiked with a trace amount of SF_6. This reagent ion reacts with mercuric halides via fluoride transfer (Equation 2.4) (Khalizov et al., 2020).

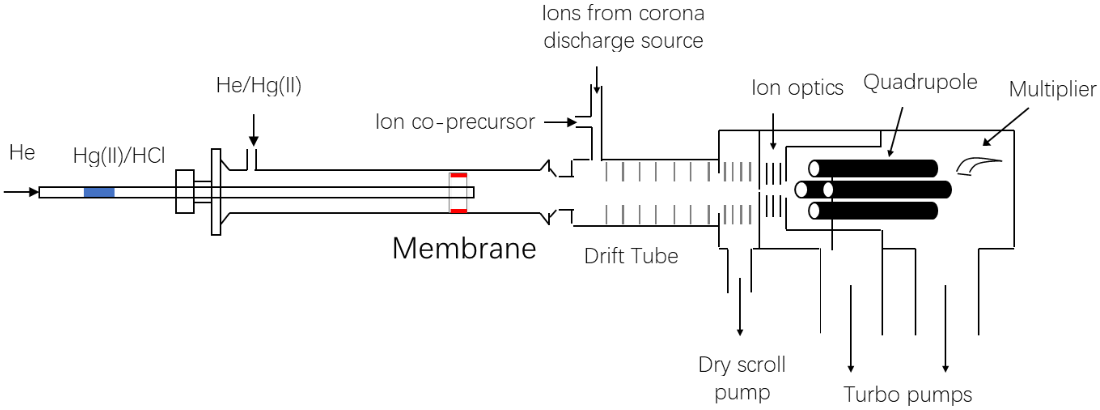

Figure 4.2 Ion drift – chemical ionization mass spectrometer coupled to a fast flow reactor. The reactor could be either 1 cm radius and 30 cm length or 0.64 cm radius and 5 cm length, giving an average flow velocity of 3 or 8 m s^{-1}, corresponding to a contact time of 3-98 or 6-7 ms, respectively, depending on the exposed surface length. Typical helium carrier flow was 140 sccm, and the reactor pressure was 2 Torr.

Gaseous mercuric compounds entered the drift tube from a deactivated-wall glass reactor (1 cm radius 30 cm length, or 0.64 cm radius 5 cm length maintained at a 2 Torr pressure, same as in the drift tube). In the experiments with CEM membranes, a rectangular piece of membrane (untreated or pre-treated with chemicals) was rolled to form a cylinder and inserted coaxially into reactor (Figure 4.2).

Gaseous chemicals released by the membrane were swept by a carrier helium flow, which was supplied through a side inlet at the back of the reactor, and delivered into the drift tube for analysis. In some experiments, the sample was heated to a temperature up to 120 °C, using a heating tape wrapped around the reactor. In exposure studies, gaseous $HgCl_2$, $HgBr_2$, or both were introduced from movable glass injectors described above. The injector tip could be positioned either upstream or downstream of the membrane to begin or terminate the exposure, and the flow through the injector could be turned on or off. The total flow of helium in the reactor had an average velocity of 3–8 m s^{-1}, corresponding to a contact time of 3–98 or 6–7 milliseconds, respectively, depending on the contact surface length.

4.3 Results and Discussion

4.3.1 Exchange Reactions in Aqueous Solutions

Our first step was to synthesize HgBrCl through the exchange reaction between $HgCl_2$ and $HgBr_2$ in an aqueous solution, isolate this chemical in crystalline form, and explore its analysis using different analytical methods (Figure 4.3a). Like other mixed mercuric halides, HgBrCl can readily form upon mixing the individual halides in vapor and liquid phases.(Beattie et al., 1970; Givan et al., 1976a; Givan et al., 1976b; Janz et al., 1963) Our synthesis was carried out by reacting the saturated solutions of $HgBr_2$ (16 mM) and $HgCl_2$ (140 mM) in a 1:1 molar ratio (Equation 4.1).

$$HgBr_{2(aq)} + HgCl_{2(aq)} \rightarrow 2HgBrCl_{(aq)} \quad (4.1)$$

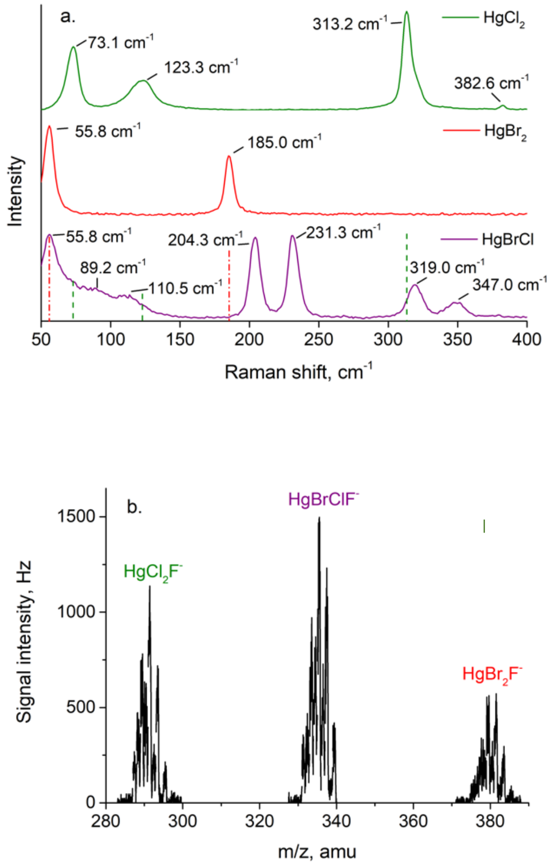

Figure 4.3 Identification of HgBrCl formed during the exchange between two covalent mercury compounds, $HgCl_2$ and $HgBr_2$, in an aqueous solution, using a 1:1 molar ratio: (a) Raman spectra of individual reactants ($HgCl_2$ and $HgBr_2$) and their crystalline reaction product and (b) ID-CIMS analysis of the vapor released by the crystalline reaction product. In the HgBrCl spectrum, peaks corresponding to $HgCl_2$ and $HgBr_2$ are marked as dashed green lines and red dash-dot lines, respectively.

We analyzed the reaction mixture by ESI-MS, using the positive and negative ion modes with formic acid and ammonium formate as electrolytes, respectively, but detected neither the reactants nor the product. This is in agreement with the previous report on the low proton affinity of mercuric halides (Dibble et al., 2014) and their weak binding with organic acids (Rutter & Schauer, 2007). Accordingly, subsequent analysis was performed on a solid crystalline sample obtained by crystallization of the aqueous reaction mixture.

Table 4.1 Raman Shifts (cm^{-1}) of $HgCl_2$, $HgBr_2$, and HgBrCl[a,b]

Chemical	Our measurement	Literature		
	solid state	molten state(Janz & James, 1963)	matrix isolation(Givan & Loewenschuss, 1976a; Givan & Loewenschuss, 1976b)	solid state(Janz & James, 1963)
$HgCl_2$	73.1 (s)			
	123.3 (m)			116
	313.2 (vs)	313 (p)	345 (m)	314
	382.6 (vw)	376 (dp)	353.3 (vs)	375
			358.4 (vs)	
$HgBr_2$	55.8 (vs)			
	185.0 (vs)	195 (p)		184
			219	
			222.5-225	
		271 (p)		
HgBrCl	55.8 (vs)			
	89.2 (m)		91	
	110.5 (m)	111 (vw)		
	204.3 (vs)	203 (vw)		
	231.3 (vs)	236 (m.)	253.6 (vs)	
			255.5(vs)	
	319.0 (m)	319 (vw)		
	347.0 (w)	335 (m)	363.7(w)	
			369.3(w)	
			378.8(vs)	
			386.5 (vs)	

[a] Produced by mixing $HgCl_2$ and $HgBr_2$ solutions in a 1:1 molar ratio

[b] vs, very strong; s, strong; m, medium; w, weak; vw, very weak; p, polarized, dp, depolarized

Figure 4.3a shows the observed Raman spectra of crystalline $HgCl_2$, $HgBr_2$, and HgBrCl. The corresponding Raman shifts are listed in Table 4.1, along with the literature data. Our spectral data for reactants are in fair agreement with previous studies (Givan & Loewenschuss, 1976a; Givan & Loewenschuss, 1976b; Janz & James, 1963) of the solid state samples, with additional peaks in the low-frequency region (50-200 cm^{-1}) that were not reported previously. For instance, $HgCl_2$ has two strong peaks (73.1 and 313.2 cm^{-1}), a medium peak (123.3 cm^{-1}), and a very weak peak (382.6 cm^{-1}). The last three peaks are somewhat shifted relative to previous observations (Givan & Loewenschuss, 1976a; Givan & Loewenschuss, 1976b; Janz & James, 1963), and a new feature at 73.1 cm^{-1} is observed in the low-frequency region. The solid $HgBr_2$ has two strong peaks in our instrument's range (55.8 and 185 cm^{-1}), where the latter peak matches previous observation made on a solid sample (Table 4.1). On the basis of the spectrum obtained for the reaction product, we conclude that the reactants were nearly fully converted into HgBrCl ($\log K$ 1.10-2.0 (Marcus, 1957; Spiro & Hume, 1961)). The spectrum shows three strong peaks (55.8, 204.3, and 231.3 cm^{-1}), two medium strength peaks (89.2, 110.5, and 319.0 cm^{-1}) and a weak peak (347.0 cm^{-1}). Since there is no spectral information on HgBrCl in the solid state and below 91 cm^{-1}, we can only compare our experimental data against the literature values obtained for HgBrCl in an argon matrix and molten state (Table 4.1). Among all those spectral lines, 55.8 cm^{-1} in HgBrCl matches the low-frequency region in $HgBr_2$ and 89.2 cm^{-1} matches the peak at 91 cm^{-1} in argon matrix. In addition, the peaks at 110.5, 204.3, 231.3, and 319.0 cm^{-1} match closely to the peaks at 111, 203, 236, and 319 cm^{-1} in the molten state, although the peak strength often is different, probably due to the difference in the phase state. Finally, the peak at 347 cm^{-1} may correspond to the peak at 335 cm^{-1} in the molten state and a group of peaks at 363.7–386.5 cm^{-1} in the argon matrix.

Figure 4.3b shows a mass spectrum of the volatile components of the solid reaction product. The mass spectrum was obtained by ID-CIMS on a sample prepared by depositing the solution with reaction mixture on a CEM membrane, drying, and placing the membrane inside the reactor under a flow of helium at ambient temperature. Three groups of peaks can be clearly seen, corresponding to gas-phase $HgCl_2$, $HgBr_2$, and HgBrCl in the form of their complexes with F^-. It should be noted that normally CEM membranes require heating to release the trapped GOM and the observed evaporation at room temperature was due to membrane being overloaded, resulting in a layer of a solid product over the membrane. The peak intensity does not necessarily reflect the composition of the solid material on the membrane, as several effects must be taken into account, including the mass discrimination of the instrument, the difference in ion-molecule reaction rate constants, the difference in volatility of these three chemicals, and possible disproportionation of HgBrCl upon evaporation off the sample surface. Nevertheless, based on the Raman and mass spectra, we conclude that in an aqueous solution a significant fraction of the original $HgCl_2$ and $HgBr_2$ was converted to a mixed halide product HgBrCl.

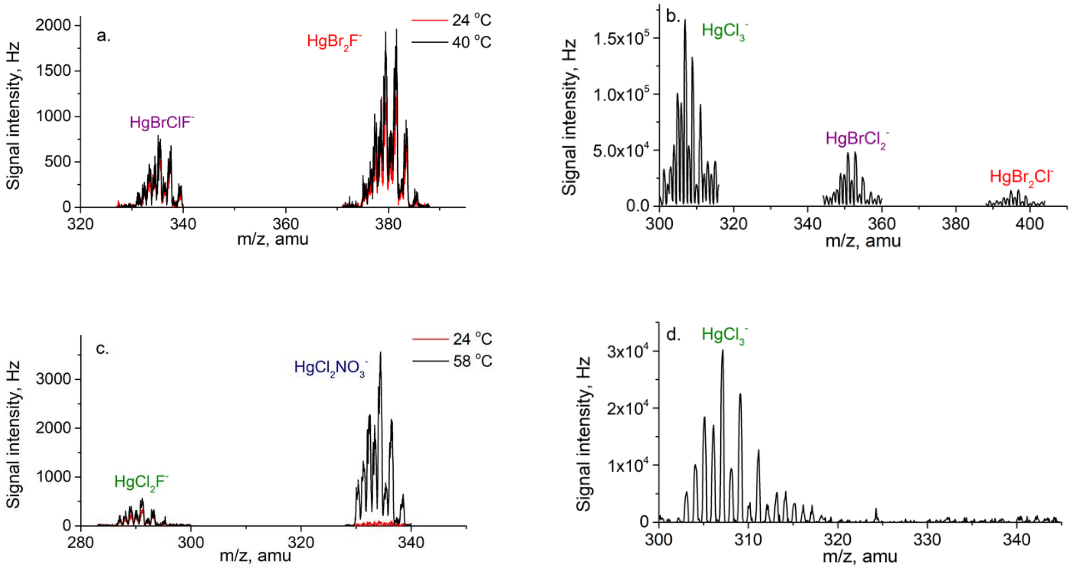

Figure 4.4 Identification of products formed in aqueous solutions through the exchange reactions involving a covalent mercury compound ($HgBr_2$), an ionic mercury compound ($Hg(NO_3)_2$), and ionic non-mercury compounds (KCl and NH_4Cl): (a) ID-CIMS analysis of vapor above crystalline product of the reaction between $HgBr_2$ (16 mM) and KCl (33 mM); (b) ESI-MS analysis of a mixture of $HgBr_2$ (44 μM) and NH_4Cl (1.2 mM) in water:methanol (50:50) solution; (c) ID-CIMS analysis of vapor above the crystalline product produced in the reaction between aqueous $Hg(NO_3)_2$ (16 mM) and KCl (33 mM); and (d) ESI-MS analysis of a mixture of $Hg(NO_3)_2$ (30 μM) and NH_4Cl (1.2 mM) in water:methanol (50:50) solution.

Our next step was to test if the exchange can occur readily when one or both reactants are ionic rather than covalent substances. Figure 4.4a and 4.4b demonstrate the formation of HgBrCl and $HgCl_2$ through a stepwise exchange of $HgBr_2$ with Cl^- in an aqueous phase (Equations 4.3 and 4.4).

$$HgBr_{2(aq)} + Cl^-_{(aq)} \rightarrow HgBrCl_{(aq)} + Br^-_{(aq)} \tag{4.3}$$

$$HgBrCl_{(aq)} + Cl^-_{(aq)} \rightarrow HgCl_{2(aq)} + Br^-_{(aq)} \tag{4.4}$$

Reaction products were analyzed in the gas and in solution, using ID-CIMS and ESI-MS, respectively. The sample for the gas-phase analysis was prepared by treating a cation exchange membrane with an aqueous solution containing $HgBr_2$ and KCl (16 mM and 33 mM, respectively) and drying. Then, the volatile constituents were detected by ID-CIMS in a flow of 140 standard cubic centimeters per minute (sccm) helium at 2 Torr. Figure 4.4a shows the presence of an unreacted $HgBr_2$, along with the newly formed HgBrCl, in vapor released by the overloaded membrane even at room temperature. The signal of desorbed chemicals increased when the membrane was heated up to 40 ºC. The analysis in the aqueous phase was performed on a mixture of 44 μM $HgBr_2$ and 1.12 mM NH_4Cl, using ESI-MS. In these experiments, a semivolatile NH_4Cl was used instead of KCl as both an electrolyte and a source of Cl^-, to eliminate the interference from K^+ ions on the electrospray performance. Figure 4.4b shows that when present in a great excess, Cl^- could replace up to two Br^- in $HgBr_2$, forming HgBrCl and $HgCl_2$ (Equations 4.3 and 4.4), which complexed further with Cl^- (Equations 4.6 and 4.7) in the electrospray to generate $HgBrCl_2^-$ and $HgCl_3^-$ (Sjoberg, 1977), as observed in the mass spectrum. A similar complexation reaction with Cl^- (Equation 4.5) occurred to $HgBr_2$, which was detected as $HgBr_2Cl^-$.

$$HgBr_{2(spray)} + Cl^-_{(spray)} \rightarrow HgBr_2Cl^-_{(spray)} \quad (4.5)$$

$$HgBrCl_{(spray)} + Cl^-_{(spray)} \rightarrow HgBrCl_2^-{}_{(spray)} \quad (4.6)$$

$$HgCl_{2(spray)} + Cl^-_{(spray)} \rightarrow HgCl_3^-{}_{(spray)} \quad (4.7)$$

Using similar approaches, we also investigated the exchange between two ionic compounds, $Hg(NO_3)_2$ and KCl (or NH_4Cl), in an aqueous solution. The ID-CIMS analysis of vapor of the solid product at room temperature (Figure 4.4c) showed the presence of $HgCl_2$ (as $HgCl_2F^-$), which was formed via Equation (4.8), below. Heating the sample to 58 ºC resulted in the disproportionation of the solid $Hg(NO_3)_2{\cdot}H_2O$, generating a large concentration of gas-phase nitric acid (Equation 4.9), which then reacted with SF_6^- in the ion drift tube to form a strong peak of $HF{\cdot}NO_3^-$ (Equation 4.11) (Huey et al., 1995). The latter acted as a secondary reagent ion, converting $HgCl_2$ to $HgCl_2NO_3^-$ (Equation 4.10). However, $Hg(NO_3)_2$ itself was not volatile under conditions of our experiment, as we could not detect any mercury-related signals upon heating of the pure crystalline $Hg(NO_3)_2{\cdot}H_2O$ to about 100 °C.

$$Hg^{2+}_{(aq)} + 2Cl^-_{(aq)} \rightarrow HgCl_{2(aq)} \quad (4.8)$$

$$Hg(NO_3)_2{\cdot}H_2O_{(s)} \rightarrow Hg(OH)NO_{3(s)} + HNO_{3(g)} \tag{4.9}$$

$$HgCl_{2(g)} + HF{\cdot}NO_3^-{}_{(g)} \rightarrow HgCl_2{\cdot}NO_3^-{}_{(g)} + HF \tag{4.10}$$

$$HNO_{3(g)} + SF_6^-{}_{(g)} \rightarrow HF{\cdot}NO_3^-{}_{(g)} + SF_{5\ (g)} \tag{4.11}$$

$$HgCl_{2\ (spray)} + Cl^-{}_{(spray)} \rightarrow HgCl_3^-{}_{(spray)} \tag{4.12}$$

Upon the analysis in the aqueous phase, injecting the solution containing 30 μM $Hg(NO_3)_2$ and 1.12 mM NH_4Cl into ESI-MS showed $HgCl_3^-$ as the only ion product (Figure 4.4d). Based on the reported Hg^{2+} + Cl^- equilibria (Sjoberg, 1977), at this concentration of aqueous chloride most of Hg(II) would exist as $HgCl_2$, and the observed trichloride ion most probably was formed when the concentration of chloride increased dramatically upon evaporation of the electrospray droplets (Equation 4.12).

Thus, we conclude that in aqueous solutions, Hg(II) can readily exchange ligands with itself and other compounds containing halide ions to form simple or mixed mercury halides, depending on the reactant ratios. Volatile mercury halides can readily desorb off the solid samples prepared by crystallization of the above solutions.

4.3.2 Exchange Reactions Between Chemicals Present in Gas and on Surface

Having understood the interactions of mercuric species and non-mercury species in solution, we could investigate the interactions between gaseous and surface-bound chemicals. The surface-bound $HgBr_2$ was prepared by treating the cation exchange membrane with 16 mM $HgBr_2$ solution and drying. The membrane was then exposed to gaseous $HgCl_2$ or HCl inside a reactor connected to ID-CIMS (Figure 4.2b). In an additional experiment, the membrane was exposed to a 50 μM KCl solution to obtain less than a monolayer KCl coverage, dried, and then exposed to gaseous $HgBr_2$ in the flow reactor.

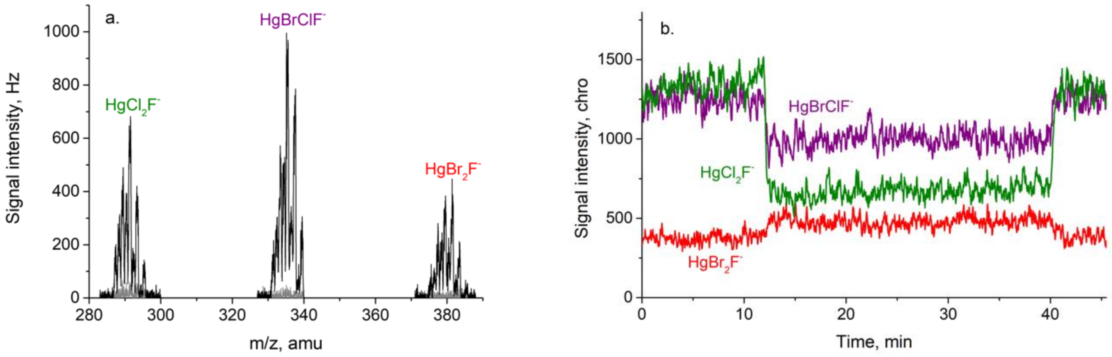

Figure 4.5 Exchange reaction of gaseous $HgCl_2$ with the surface-bound $HgBr_2$: (a) mass spectrum taken during exposure at ~20 min and (b) selected ion traces of $HgCl_2$ (291 amu, as $HgCl_2F^-$), $HgBr_2$ (381 amu, as $HgBr_2F^-$), and HgBrCl (335 amu, as $HgBrClF^-$). The surface-bound $HgBr_2$ was prepared by treating the cation exchange membrane with an aqueous $HgBr_2$ solution (16 mM) and drying. Gaseous $HgCl_2$ was introduced in helium flow at room temperature (295 K) at 2 Torr and volatile products were analyzed by ID-CIMS. The $HgCl_2$ injector was retracted at 12 min to begin exposure and moved to its original position at 40 min to stop exposure. The background signal with the reactor disconnected from the ID-CIMS is shown as a grey trace in (a).

Figure 4.5b shows selected ion traces of the reactants and product for the case involving the exposure of the membrane-bound $HgBr_2$ to $HgCl_2$. At 0–12 min, $HgCl_2$ was flowing (7.7×10^{10} molecule cm^{-3} in the reactor), but the injector tip was positioned downstream of the membrane, hence preventing its direct exposure to $HgCl_2$. Nevertheless, HgBrCl was produced and in a large amount, as indicated by its strong signal compared to the signal of $HgCl_2$. The signal of $HgBr_2$ desorbing off the membrane can also be seen because the membrane was overloaded with $HgBr_2$, as discussed above. The presence of a large concentration of HgBrCl under conditions of no membrane exposure to $HgCl_2$ indicates that the exchange between $HgCl_2$ and $HgBr_2$ was occurring not on the membrane (Equation 4.13), but on the deactivated reactor wall downstream (Equation 4.14) with surface coverages of under a single monolayer, as described in detail in Section 4.3.3.

$$HgCl_{2(g)} + HgBr_{2(membrane)} \rightarrow 2HgBrCl_{(membrane)} \tag{4.13}$$

$$HgCl_{2(g)} + HgBr_{2(g)} \xrightarrow{Pyrex} 2HgBrCl_{(g)} \tag{4.14}$$

When at 12 min, the injector was retracted, the concentration of $HgCl_2$ decreased, mostly due to its uptake by the untreated portion of the membrane. The concentration of HgBrCl decreased as well, indicating that most of HgBrCl produced on the membrane remained there in the adsorbed state at room temperature. The concentration of $HgBr_2$ increased because less of it was converted to HgBrCl on the reactor wall downstream when the concentration of $HgCl_2$ was lowered. Figure 4.5a shows the mass spectrum of the reactants and the product at approximately 20 min. Upon returning the injector to its original position downstream the membrane at ~39 min, signals of the reactants and exchange product returned to their initial levels.

It is instructive to compare this case against an experiment where the exchange reaction was studied between gaseous $HgBr_2$ and solid $HgCl_2$ deposited on the surface of a frosted borosilicate (Pyrex) tube, similar as in our recently reported uptake experiments (Mao et al., 2021). Not only $HgCl_2$ is more volatile than $HgBr_2$ (Bernard et al., 1997; Ruf et al., 1954; Stull, 1947; Trimble, 1987), but also its binding with the frosted tube is weaker than with the membrane. Hence, a significant amount of $HgCl_2$ was continuously desorbed into the helium flow and carried into ID-CIMS, producing a $HgCl_2F^-$ signal approximately 100 times stronger than the signal of $HgBr_2F^-$ (Figure 4.6). The $HgCl_2F^-$ product ion was so abundant that it acted as a secondary reagent ion along with SF_6^-, initiating secondary ion-molecule reactions in the drift tube to form $HgCl_3^-$ and $HgBrCl_2^-$ (Equations 4.15 and 4.16).

$$HgCl_2F^- + HgCl_2 \rightarrow HgCl_3^- + HgClF \tag{4.15}$$

$$HgCl_2F^- + HgBr_2 \rightarrow HgBrClF^- + HgBrCl \tag{4.16}$$

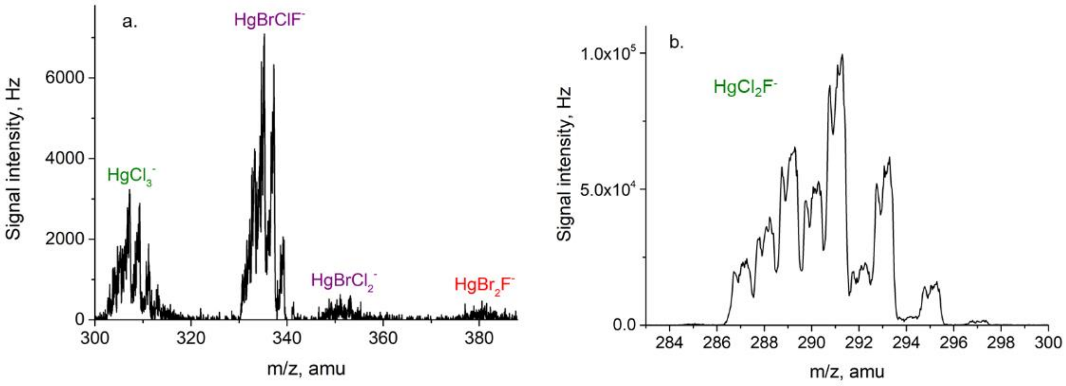

Figure 4.6 Mass spectra of gaseous chemicals released upon the interaction between gaseous $HgBr_2$ and surface-bound $HgCl_2$: (a) species of a lower abundance and (b) highly abundant $HgCl_2F^-$ ion product. The surface-bound $HgCl_2$ was prepared by treating the frosted borosilicate glass tube with a 140 mM aqueous $HgCl_2$ solution and drying. Gaseous $HgBr_2$ was introduced in a flow of helium at room temperature (295 K) and volatile products were analyzed by ID-CIMS.

When the membrane loaded with nearly a monolayer of KCl was exposed to gaseous $HgBr_2$, no HgBrCl was released at room temperature, confirming the previously reported high collection efficiency of CEM (Lyman et al., 2020c). However, upon heating up of the exposed membrane, both the unreacted $HgBr_2$ and the newly formed HgBrCl were released, as shown in Figure 4.7, confirming that the exchange can occur even on a membrane with a monolayer surface coverage.

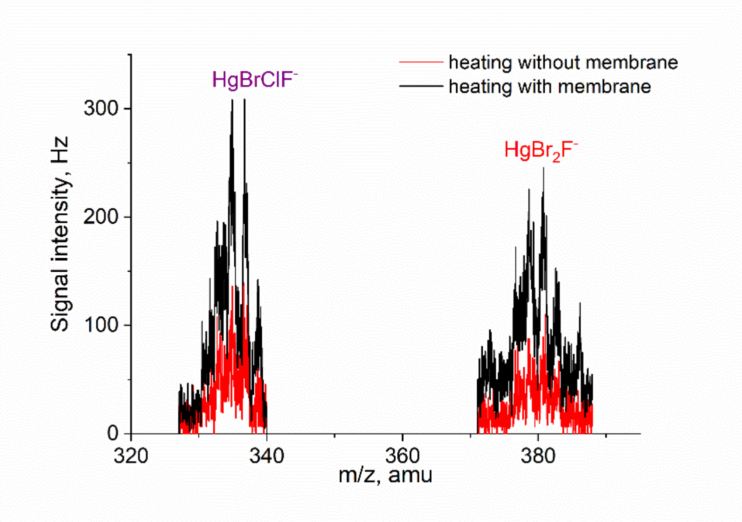

Figure 4.7 Exchange reaction between gaseous $HgBr_2$ and a monolayer of KCl on a cation exchange membrane. The coated membrane was prepared by placing a droplet of a 50 µM KCl solution on a new membrane and drying. Gaseous $HgBr_2$ was introduced in helium over 5 min, then its flow was stopped and the membrane was heated to 72 ºC to desorb the reactant and product (black trace). The mass spectrum obtained with the reactor heated to 72 ºC without the membrane is shown by the red trace.

We also conducted experiments by exposing $HgBr_2$ deposited on a CEM membrane to gaseous HCl, which was introduced through a movable injector similar to the experiment with gaseous $HgCl_2$. By adjusting the stopcock of the vial holding the HCl solution, the concentration of gaseous HCl in the reactor could be varied between 10^{12}–5×10^{13} molecule

cm^{-3}, as estimated from the signal of its product ion $HFCl^-$ formed via Equation (4.17) (Huey et al., 1995) (Figure 4.8 inset).

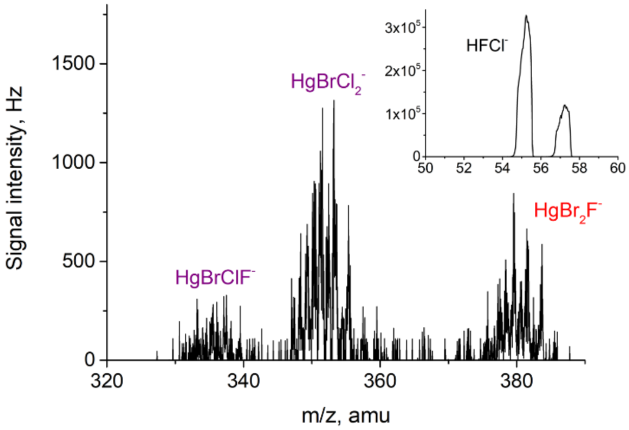

Figure 4.8 Exchange reactions of surface-bound $HgBr_2$ with gaseous HCl. The surface-bound $HgBr_2$ was prepared by treating a cation exchange membrane with the aqueous $HgBr_2$ solution (16 mM) and drying. Gaseous HCl was exposed to the surface-bound $HgBr_2$ in a helium flow at room temperature (295 K) and volatile products were analyzed by ID-CIMS. The inset shows the mass spectrum of the $HFCl^-$ ion product produced in a large concentration in the ion-molecule reaction of HCl with SF_6^-.

$$HCl + SF_6^- \rightarrow HFCl^- + SF_5 \tag{4.17}$$

$$HCl_{(g)} + HgBr_{2(\text{frosted pyrex})} \rightarrow HgBrCl + HBr \tag{4.18}$$

$$HgBrCl + HFCl^- \rightarrow HgBrCl_2^- + HF \tag{4.19}$$

The signal of $HFCl^-$ was nearly 300 times stronger than that of $HgBr_2F^-$. Hence, the mixed halide HgBrCl that was produced in the exchange Equation (4.18) could be detected not only as $HgBrClF^-$ through the reaction with SF_6^-, but also as $HgBrCl_2^-$ through the reaction with $HFCl^-$ (Equation 4.19), as shown in Figure 4.8.

Here we can conclude that mercuric halides can readily engage in exchange reactions with other mercuric halides, hydrogen chloride, and chloride ion, where one of the chemicals is present in the gas phase and the other one is sorbed on membranes or on frosted borosilicate glass. Furthermore, these exchange reactions can occur even on deactivated borosilicate glass or at a surface coverage corresponding to a single monolayer.

4.3.3 Exchange Reactions of Gaseous Oxidized Mercury Catalyzed by the Surface

In this section, we present the results of experiments where exchange reactions between $HgCl_2$ and $HgBr_2$ were studied by delivering both mercuric halides in flow of gas. Two types of surfaces were selected: a relatively inert deactivated borosilicate glass and highly adsorptive cation exchange and nylon membranes. As shown in the previous section, our experiments involving the interaction between the gaseous and sorbed chemicals indicated the occurrence of a rapid exchange on the deactivated glass, and hence we present those experiments first.

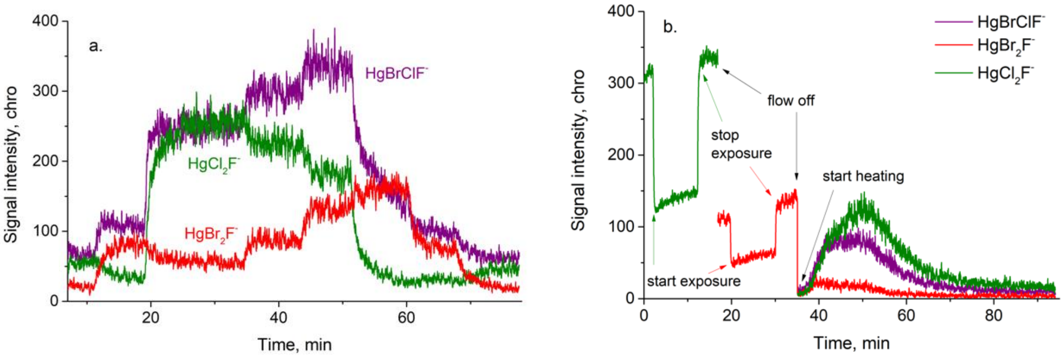

Figure 4.9 Exchange reaction between two gaseous covalent mercury compounds, $HgCl_2$ and $HgBr_2$ in the presence of (a) inert surface (deactivated borosilicate glass) and (b) highly adsorptive surface of the cation exchange membrane. Gaseous reactants were introduced stepwise from individual injectors, using helium as a carrier gas at 2 Torr pressure. The total flow velocity was 8 and 3 m s^{-1} in (a) and (b), corresponding to contact times of 6-7 and 3-4 ms, respectively. Also, in case (b) the supply of reactants was cut off at 38 min and the membrane was thermally desorbed by heating from room temperature to 114 °C in a flow of helium (140 sccm). Detection was performed in real-time by ID-CIMS, using selected ion traces at *m*/*z* 291 amu ($HgCl_2F^-$), 381 amu ($HgBr_2F^-$), and 335 amu ($HgBrClF^-$).

In the experiments with deactivated glass, the inner wall of the flow reactor was used as the surface for exchange. Gaseous $HgCl_2$ was introduced through a movable injector while gaseous $HgBr_2$ was admixed into the main helium flow, which entered through a side inlet at the back of the 0.64 cm radius and 5 cm length reactor (Figure 4.1). The reaction was initiated by starting or stopping the flows of $HgCl_2$ and $HgBr_2$, and the reaction time (of the order of 1-10 milliseconds) could be controlled by moving the $HgCl_2$ injector forward or backward while the signals of the reactants and exchange product were recorded in real-time by ID-CIMS. In Figure 4.9a, only the helium carrier flow was turned on initially, whereas $HgCl_2$ and $HgBr_2$ flows were kept off. However, both halides and the exchange product could be detected because even in the absence of the injector flows, small amounts of halide vapors emerged from the injectors by diffusion, which was further aided by the Bernoulli effect due to the fast carrier flow velocity (8 m s^{-1}). At 11 min, the $HgBr_2$

flow was turned on (2 sccm), leading to an increase in the HgBrCl signal and a decrease in $HgCl_2$. At 19 min, the $HgCl_2$ flow was also turned on (2 sccm), leading to a more significant increase in HgBrCl and a decrease in $HgBr_2$, as expected from the reaction stoichiometry (Equation 4.14). The change in signals due to varying of the $HgCl_2$ flow was larger than when varying the $HgBr_2$ flow because $HgCl_2$ has a higher saturation vapor pressure than $HgBr_2$, resulting in a higher concentration for the same injector flow rate. Later, when the $HgBr_2$ flow was increased stepwise to 4 and 8 sccm at 35 and 44 min, respectively, the signal of HgBrCl increased and the signal of $HgCl_2$ decreased, accordingly. At 51 min, the $HgCl_2$ flow was turned off, its signal dropped and the signal of HgBrCl followed (although lagging behind $HgCl_2$), but the signal of $HgBr_2$ increased because less of it was now consumed through the exchange with $HgCl_2$. Finally, the flow of $HgBr_2$ was decreased to 2 sccm and 0 sccm at 61 and 67 min, respectively, which resulted in a decrease in HgBrCl, but an increase in $HgCl_2$.

At any given reaction time for any ratio of concentrations, the ratio of the signals $S_{\mathrm{HgBrCl}}^2/(S_{\mathrm{HgCl_2}} \times S_{\mathrm{HgBr_2}})$ remained around 4.5 and the signal of HgBrCl was approximately equal to the sum of signals of $HgCl_2$ and $HgBr_2$, for instance, $S_{\mathrm{HgBrCl}} \approx S_{\mathrm{HgCl2}} + S_{\mathrm{HgBr2}}$. The latter observation is in agreement with the reaction stoichiometry (Equation 4.14) and also indicates that the contributions from the ion mass discrimination and different ion-molecule reactivities in ID-CIMS were of minor importance. Thus, the former ratio can be treated as the equilibrium constant for Equation (4.14) on a deactivated Pyrex surface, where log*K* = 0.65. This value is somewhat outside of the range reported previously (log*K* = 1.1–2.0 (Marcus, 1957; Spiro & Hume, 1961)), which is not surprising, as those previous values were measured in solutions and vapors (although surface catalysis is expected in the latter case). Time dependent ion traces show that the exchange was fast and occurred on a timescale of the adsorption-desorption process (Figure 4.9a). When the concentration of one reactant was changed abruptly, the other reactant and product adjusted at a comparable rate. Moving the injector forward or backward to change the reaction time by several milliseconds had a minor effect on the signals magnitude, confirming that the reaction was at equilibrium due to the fast exchange. In addition, we discovered that placing a PTFE sleeve inside the reactor to replace the surface of silylated borosilicate with fluoropolymer had no significant effect on the extent of exchange, indicating that even minor surface adsorption was sufficient to drive the exchange reaction at 10^{10}–10^{11} molecules cm^{-3} reactant concentrations.

Before we move to the next case, it is important to rule out the contribution of gas-phase processes in the formation of HgBrCl, i.e., we need to establish that this reaction indeed occurred on the surface and not as an interaction between two gas-phase neutrals or a neutral and an ion. It can be readily shown that these gas-phase reactions are simply not fast enough to explain the observed degree of conversion of the reactants. Indeed, assuming the gas-phase reaction between neutrals as bimolecular barrierless process occurring at a collision limit ($k_{bi} \sim 10^{-10}$ cm^3 $molecule^{-1}$ s^{-1}), the characteristic time for the HgBrCl formation $\tau = (k_{bi} \times [HgCl_2])^{-1}$ is about 0.1 second, which is at least 10 times longer than the typical residence time in the reactor. Ion-molecule reactions are about ten times faster than the collision limit for neutrals, but in order for the secondary ionization reaction to occur, e.g., $HgCl_2F^- + HgBr_2 \rightarrow HgBrClF^- + HgBrCl$, a large concentration of the $HgCl_2F^-$ ion product is required. For instance, in the previous section we show cases where 100–300 times higher concentrations of product ions $HgCl_2F^-$ and $HFCl^-$ were needed to serve as secondary reagent ions and produce comparable signals of additional ions. Also, in those reactions only a single atom was exchanged during the collision, whereas in the above reaction two atoms from different moieties would have to be exchanged, which is not feasible entropically.

Finally, we also conducted an experiment where an untreated cation exchange membrane was exposed to gaseous $HgCl_2$ and $HgBr_2$ similar as during atmospheric GOM sampling, albeit using significantly higher concentrations of gaseous chemicals. In this experiment, the membrane was cut into a 4×1 cm rectangle, rolled into a cylinder, placed inside the reactor, and exposed first to $HgCl_2$ and then to $HgBr_2$. As the reactor allows for only one movable injector at a time, the $HgCl_2$ injector had to be replaced with the $HgBr_2$ injector in the middle of the experiment, and during this time, the valve separating the flow reactor from ID-CIMS was kept closed.

Figure 4.9b shows such an experiment, where the membrane was sequentially exposed to $HgCl_2$ and $HgBr_2$, and then heated to 114 °C while monitoring the reactants and products in real-time by ID-CIMS. At zero time, $HgCl_2$ was being introduced into the reactor in a flow of helium (2 sccm), but the tip of the injector was positioned downstream the membrane, preventing exposure. At about 2 min, the injector was retracted behind the membrane to start the exposure, resulting in a significant drop in the $HgCl_2$ signal. After about 10 min, the exposure was terminated by returning the injector to its original position and the signal recovered to its initial value. The increasing trend in the signal before, during, and after exposure was caused by the drift in the $HgCl_2$ and reagent ion concentrations. When accounted for the drift, the signal recovery with the retracted injector was negligible, indicating that no desorption was taking place and hence the membrane surface was below saturation by $HgCl_2$. At 18 min, the $HgCl_2$ injector was replaced with the $HgBr_2$ injector, and a 4 sccm flow of gaseous $HgBr_2$ was introduced in a flow of helium. The exposure began at 20 minutes and continued for 10 minutes, and then all flows were stopped except for the main helium carrier. During this time, no significant desorption occurred from the membrane at room temperature, confirming previous reports of the CEM effectiveness as a collecting medium (Lyman et al., 2020c). When at 38 min the membrane was heated from room temperature to 114 °C to desorb the trapped GOM, the release of $HgCl_2$, $HgBr_2$, and the exchange product HgBrCl occured (Equation 4.20).

$$HgCl_{2(g)} + HgBr_{2(g)} \xrightarrow{Membrane} 2HgBrCl \qquad (4.20)$$

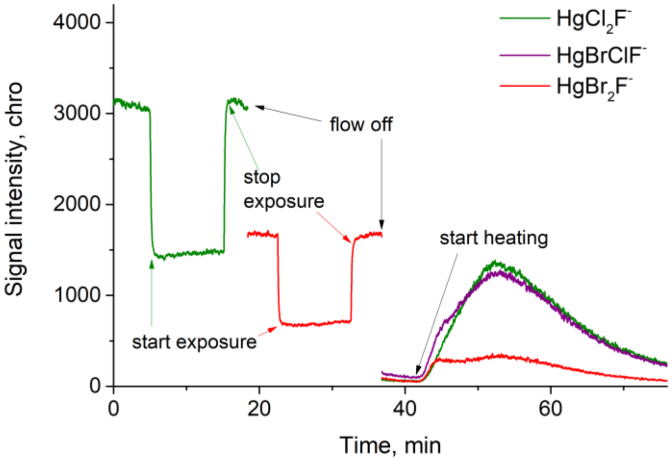

Figure 4.10 Exchange reaction between two gaseous covalent mercury compounds, $HgCl_2$ and $HgBr_2$ in the presence of a highly adsorptive surface of the nylon membrane. Gaseous reactants were introduced stepwise from individual injectors, using helium as a carrier gas at 2 Torr pressure. The total flow velocity was 3 m s^{-1}, corresponding to a contact time of 3-4 ms. The supply of reactants was cut off at 36 min and the membrane was thermally desorbed by heating from room temperature to 114 °C in a flow of helium (140 sccm). Detection was performed in real-time by ID-CIMS, using selected ion traces at *m*/*z* 291 amu ($HgCl_2F^-$), 381 amu ($HgBr_2F^-$), and 335 amu ($HgBrClF^-$).

Repeating the experiment with nylon a membrane showed a nearly identical exchange pattern (Figure 4.10). In both experiments the membranes were placed close to the reactor exit to minimize the interaction with the reactor wall, but we cannot exclude that some additional exchange may have occurred on Pyrex after desorption downstream of the membranes. To verify if the wall exchange reaction could be limited by gas transport, we repeated the experiment in an empty reactor in nitrogen carrier, but observed an identical behavior (Figure 4.11). Based on these experiments, we conclude that exchange between gaseous mercuric compounds is rapid and may occur not only on highly adsorptive membranes but also on relatively inert surfaces, such as the deactivated borosilicate glass.

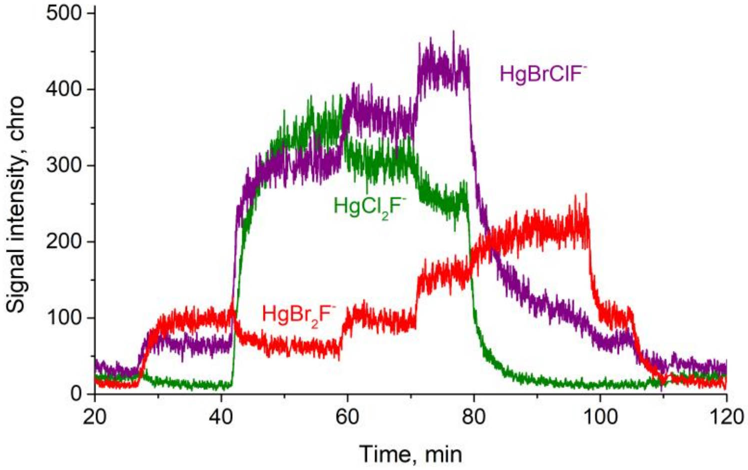

Figure 4.11 Exchange reaction between two gaseous covalent mercury compounds, $HgCl_2$ and $HgBr_2$ in the presence of inert surface (deactivated borosilicate glass), using nitrogen as a carrier gas. Gaseous reactants were introduced stepwise from individual injectors at 2 Torr pressure. The total flow velocity was 8 m s^{-1}, corresponding to contact times of 6-7 ms, respectively. Detection was performed in real-time by ID-CIMS, using selected ion traces at *m*/*z* 291 amu ($HgCl_2F^-$), 381 amu ($HgBr_2F^-$), and 335 amu ($HgBrClF^-$).

4.4 Conclusions and Atmospheric Implications

We investigated mutual interactions of mercuric compounds and other chemicals under conditions that simulate the processing of GOM by atmospheric aerosols and the collection of GOM during speciation analysis, and found occurrences of a rapid exchange in solutions, on surfaces, and in the gas phase in the presence of surfaces. Depending on the relative concentrations of chemicals, this exchange can either modify or even completely scramble the molecular speciation of mercuric compounds under our experimental conditions. In our study, limited by the current detection limit of ID-CIMS, the experiments were conducted using concentrations of mercuric compounds (10^{10}–10^{11} molecules cm^{-3}) that were significantly higher than in the atmosphere (~10^5 molecules cm^{-3}). Thus, in the following, we extrapolate our results towards typical atmospheric conditions to make predictions.

First, we evaluate the potential for GOM to undergo exchange when it is converted to PBM via partitioning to atmospheric particulate matter (PM), such as the sea salt. Assuming the PM and PBM concentrations of 10 $\mu g\ m^{-3}$ and 5-100 pg m^{-3}, respectively (Lewis & Schwartz, 2004; Lyman et al., 2020a), and a relative humidity of 60%, the concentrations of NaCl and PBM in the particle phase will be ~5 M and 0.5-10 uM, respectively. The latter PBM concentrations are comparable to the concentration used in the experiments shown in Figure 4.4 (b,d), while the particulate NaCl concentration greatly exceeds the concentration used in those experiments. Thus, as shown previously by thermodynamic evaluations (Lin et al., 2006), GOM species taken by atmospheric aerosols can indeed undergo a rapid exchange. In the presence of abundant particle-phase chloride, a significant fraction of GOM produced by photooxidation may be converted to $HgCl_2$ and then evaporate back to the gas phase, in agreement with the report that $HgCl_2$ behaved similarly to atmospheric GOM with respect to capture by denuders (Malcolm et al., 2009). Exchange can also occur in the water and soil environments, e.g., it has been reported previously that the spiked ^{198}Hg(II) exchanged with the Hg(II) bound to minerals within hours and with the Hg(II) pre-equilibrated with thiols and dissolved organic matter in minutes (Zhang et al., 2021). Furthermore, a rapid spontaneous isotope exchange (under one hour) was observed even for mercury in different oxidation states, such as between dissolved elemental mercury ^{202}Hg(0)$_{aq}$ and ^{201}Hg(II) bound to chloride and several organic ligands (Wang et al., 2020).

Next, we extrapolate our results towards the concentrations encountered under typical GOM sampling conditions. During field measurements, for the standard sample flow of 1 L min^{-1} and collection time of 2 weeks, and assuming a GOM concentration of 35 pg m^{-3} (Lyman et al., 2020a), a total of 1.4×10^{12} GOM molecules would be accumulated, corresponding to a 8×10^{10} molecules cm^{-2} surface coverage on a 4.7 cm diameter membrane. On the same membrane, 5×10^{17} molecules of HCl would deposit over the same sampling time, with the surface coverage of 3×10^{16} molecule cm^{-2}, assuming a 1 ppb mixing ratio of HCl in the air (Appel et al., 1991; Crisp et al., 2014; Harrison et al., 1990). These ambient sample coverages can be compared against the coverages obtained in two types of our experiments. In the first type (Figures 4.9b and 4.8), 2.4×10^{15} $HgCl_2$ molecules and 3×10^{18} HCl molecules were deposited on the 1-cm and 2-cm-long rolled CEM membrane cylinders, corresponding to 8×10^{14} and 4×10^{17} molecule cm^{-2} surface coverages, respectively. In the second type (Figures 4.9a and 4.11), 9.5×10^{12} $HgCl_2$ molecules were deposited on a 5-cm length of deactivated borosilicate, corresponding to a 4×10^{11} molecule cm^{-2} surface coverage. By comparing these values, one can see that the membrane coverage by HCl in our experiments was only 10 times higher than during field sampling. Considering that our experiments occurred on a time scale of minutes while atmospheric sampling typically takes 1-2 weeks, it is highly probable that the contribution from the exchange reactions with HCl and other non-mercury chemicals on membranes will be significant in atmospheric GOM analyses. The surface coverage by $HgCl_2$ and $HgBr_2$ on CEM and nylon membranes exceeded the coverage expected during atmospheric sampling by nearly four orders of magnitude. However, in the experiments with exchange on deactivated borosilicate, the surface coverage was only a factor of four higher than that expected on membranes during atmospheric collection. Thus, cross-interactions between sorbed GOM species may be also possible during atmospheric analysis.

To summarize, based on our current results, a rapid exchange (under one minute) can occur on surfaces with GOM coverages of over $\sim 10^{11}$ molecule cm^{-2} and in solutions with concentrations of over 40 μM of GOM species. Under typical atmospheric conditions, such coverages cannot be achieved on fluoropolymers (e.g., tubing and filters), but may be possible on quartz and glass, especially at elevated relative humidities (Ambrose et al., 2013). Also, one should keep in mind that PTFE filters used to split RM into PBM and GOM (Gustin et al., 2021b) would also trap significant amounts of other particulate matter, with masses ranging from hundreds to thousands micrograms, depending on the PM pollution level. Hence, the exchange of RM (as both PBM and GOM) with the chemical constituents of deposited particles becomes possible, especially at higher humidities, when the particles absorb water and liquefy. In fact, the processes occurring in the latter case will be similar to the ones in the thin film vapor method of the particle composition analysis (Bigg et al., 1974; Yamato et al., 1994), where aerosol particles are captured on screens pre-coated with a suitable reagent and then exposed to a suitable vapor to induce chemical reactions with the reagent, leading to changes in the particle appearance that can be observed by Transmission Electron Microscopy. Further careful studies using lower concentrations levels are needed to elucidate and quantify interferences that can lead to the mutual exchange between GOM species, as well as cross-exchanges between GEM, GOM, and PBM species in the presence of surfaces and condensed phases.

CHAPTER 5

KINETICS AND MECHANISM OF GAS-PHASE OXIDATION OF ELEMENTAL MERCURY

5.1 Introduction

The **goal** is to find the appropriate reagent ions to detect the intermediate products of gas-phase elemental mercury oxidation: (1) HgBr, formed through the reaction of elemental mercury with bromine radical, and (2) HgBrONO, formed via the reaction of HgBr with atmospheric abundant species (NO_2) using ID-CIMS.

5.2 Experimental

5.2.1 Schematics of the Experimental Setup

The bromine-initiated oxidation was carried by a two-step mechanism, where GEM reacts with atomic Br to produce an unstable product HgBr then reacts with NO_2 (Jiao & Dibble, 2017a; Wang et al., 2014; Wu et al., 2020). Here, atomic bromine could be generated through thermal dissociation of Br_2 (Bierbach et al., 1996) by a microwave discharge (MWD) (Equation 5.1).

$$Br_2 \rightarrow 2Br\cdot \qquad (5.1)$$

$$Hg + Br\cdot \rightarrow HgBr \qquad (5.2)$$

Atomic bromine can react with Hg(0) to form HgBr (Equation 5.2), which we are trying to detect using appropriate reagent ions (SF_6^- or CH_3COO^-) in ID-CIMS. The mercury vapor was from a heated elemental mercury source (see details in Section 2.5).

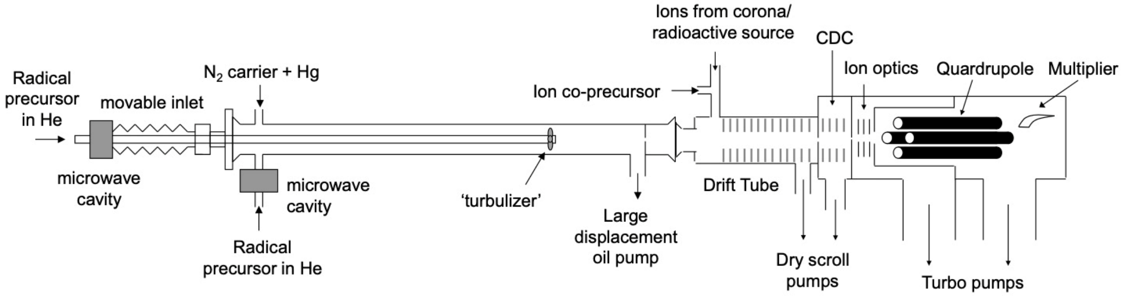

Figure 5.1 Turbulent flow reactor coupled to ID-CIMS for investigation of gas-phase mercury chemistry.

The detection of Br, reaction product HgBr and HgBrONO was achieved by ID-CIMS (Figure 5.1). The Br_2 was introduced into the reactor through the microwave cavity from the side, generating Br radical to react with Hg(0) from the other side. The formed HgBr may react with NO_2 via Equation (5.3) to form $BrHgNO_2$, which we expected to detect using SF_6^- or CH_3COO^-.

$$\mathrm{HgBr} + \mathrm{NO_2} \xrightarrow{M} \mathrm{BrHgNO_2} \qquad (5.3)$$

5.2.2 Generation of Br Radicals by Thermal Dissociation of Br_2

The microwave discharge apparatus consists of a microwave generator, a Beenakker cavity, and discharge tubes. At a frequency of 2.45 GHz, the microwave generator produces microwaves, which are transmitted into a cavity through a cable. The cavity has a shape of a pillbox in which a low-losses dielectric tube (quartz or alumina, also called a "discharge tube") is placed axially in the center to obtain a maximum electric field. A high purity inert gas such as He or Ar is used as a support gas for effective plasma and to avoid the background in mass spectra. The plasma was ignited with a homemade ignitor and then absorbed the energy of microwaves to become a hot plasma that can dissociate the bonds of Br_2 molecules (Equation 5.1).

5.2.3 Preparation of Br_2 in Bulb

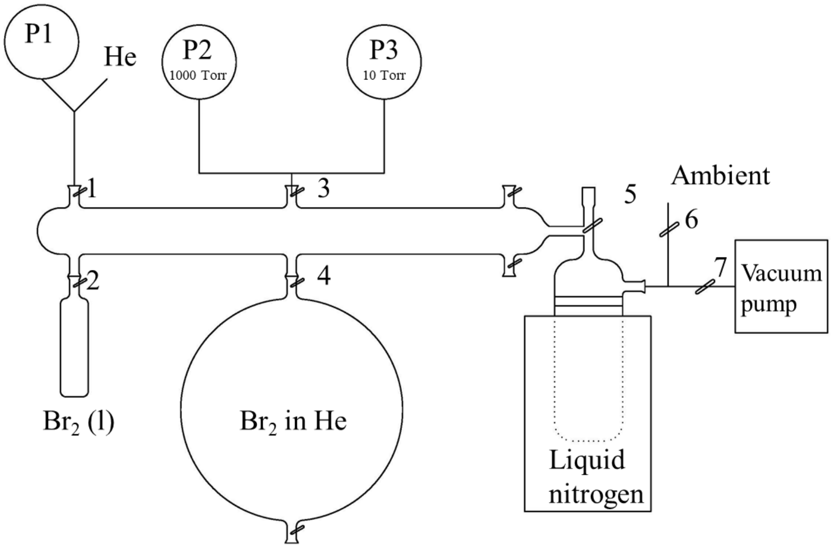

Figure 5.2 Schematic of bromine gas mixture preparation device along with Br_2 (g) glass bulb.

The bromine gas mixture could be prepared by a two-step dilution of bromine vapor at room temperature using a gas mixture preparation manifold, as shown in Figure 5.2. The liquid nitrogen was used to trap gases traveling into the pump from the system. After evacuating the preparation system, Br_2 vapor from the Br_2 (l) bubbler was introduced into a 10-inch diameter glass bulb to ~1.3 Tor, then diluted Br_2 to 750 Torr by helium gas. The glass bulb was covered by black foil to prevent Br_2 photodissociation. In the second step, pump the Br_2-He mixture from 750 Torr to ~100 Torr, then dilution follows a similar procedure, diluting ~100 Torr Br_2-He mixture to 750 using He. The final Br_2 gas concentration could be calculated in the following,

$$C_{Br_2} = \frac{1.3}{750}\frac{100}{750} \times 10^6 ppm = 231 \text{ ppm} \tag{5.4}$$

5.2.4 Calibration of NO_2 Using SF_6^- as Reagent Ion in ID-CIMS

The product ion, NO_2^-, is generated from NO_2/N_2 in reaction with SF_6^- via electron transfer,

$$NO_2 + SF_6^- \rightarrow NO_2^- + SF_6 \tag{5.5}$$

to determine the sensitivity of ID-CIMS towards NO_2 using SF_6^-, the calibration was conducted in the drift tube under 1.78 - 1.81 Torr pressure and 298 K. The NO_2 concentration range is 6.8×10^8–6.8×10^{10} molecule cm^{-3} (**method 2**) in the drift tube, corresponding to 12–1185 ppbv mixing ratios, where 1 part per billion by volume (ppbv) corresponds to 5.7×10^7 molecule cm^{-3}.

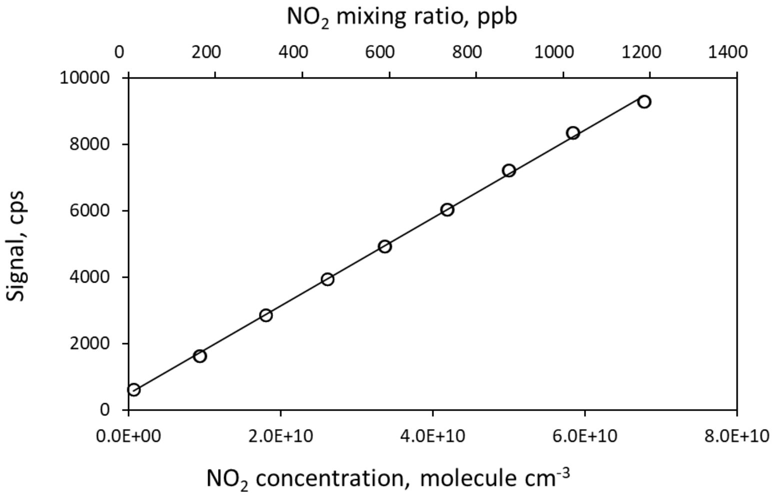

Figure 5.3 Dependence of the product ion signal on the calculated concentration of NO_2 in the drift tube measured using **method 2** and SF_6^-.

The NO_2 calibration plot for its concentration range of 6.8×10^8–6.8×10^{10} is shown in Figure 5.3. The experimental sensitivity was obtained of 7.59 Hz ppbv^{-1} using the slope and accounting for the sample dilution by the reagent ion carrier. The normalized sensitivities (i.e., at a 1 MHz reagent ion signal) was 1.9 Hz ppbv^{-1}. The LOD was 2.7 ppbv, corresponding to 6.7×10^9 molecule cm^{-3}, for a 10 s integration time and assuming a signal to noise ratio $S/N = 2$.

5.3 Detection of the Reaction Products of Hg+Br

Around 250 ppm of Br_2 in He was introduced through the microwave discharge cavity, generating ~3×10^{10} molecule cm^{-3} of Br radicals in the reactor. In our preliminary results, the observations of Br^- along with Br_2^- were confirmed using both SF_6^- and CH_3COO^- reagent ions (X^-) via electron transfer (Equations 5.6 and 5.7). Figure 5.4 shows the spectra of Br^- and Br_2^- obtained using CH_3COO^- as the reagent ions.

$$Br + X^- \rightarrow Br^- \quad (5.6)$$

$$Br_2 + X^- \rightarrow Br_2^- \quad (5.7)$$

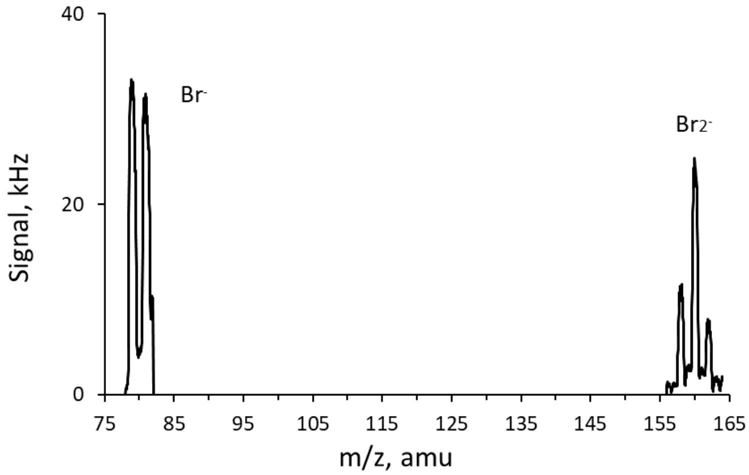

Figure 5.4 The spectra of Br^- and Br^{2-} using SF_6^- and CH_3COO^- as the reagent ions.

Then Br radical was expected to react with Hg(0) to form 6×10^9 molecule cm^{-3} of HgBr, whose concentration was calculated according to the previously reported rate constant from a Pulsed Laser Photolysis - Pulsed Laser Induced Fluorescence (PLP-PLIF) study (Donohoue et al., 2006). The ionogram of Br^- shows that no Br^- drop when the flow of Hg(0) was introduced. The reason could be that the concentration of Hg(0) introduced into the reactor was too low because no full saturation of Hg(0) was achieved in the impinger, which is the source of Hg(0).

We expected that by varying the initial concentration of bromine atoms and total gas pressure in the turbulent flow reactor, either HgBr or $HgBr_2$ could be predominantly produced. In the presence of Br radical and Hg(0), we tried to detect the product, HgBr, in the forms of $HgBr^-$ or $HgBrF^-$ (Equations 5.8 and 5.9).

$$\mathrm{HgBr} + \mathrm{SF_6^-} \rightarrow \mathrm{HgBr^-} + \mathrm{SF_6} \tag{5.8}$$

$$\mathrm{HgBr} + \mathrm{SF_6^-} \rightarrow \mathrm{HgBrF^-} + \mathrm{SF_5} \tag{5.9}$$

However, only $HgBr_2F^-$ was observed (Figure 5.5), which indicates that $HgBr_2$ is formed in the reaction. The formation of $HgBr_2$ cannot occur via Equation (5.10) because the rate constant is too slow, 1.2×10^{-16} cm^3 $molecule^{-1}$ s^{-1} (Ariya et al., 2002).

$$\mathrm{Hg} + \mathrm{Br_2} \rightarrow \mathrm{HgBr_2} \tag{5.10}$$

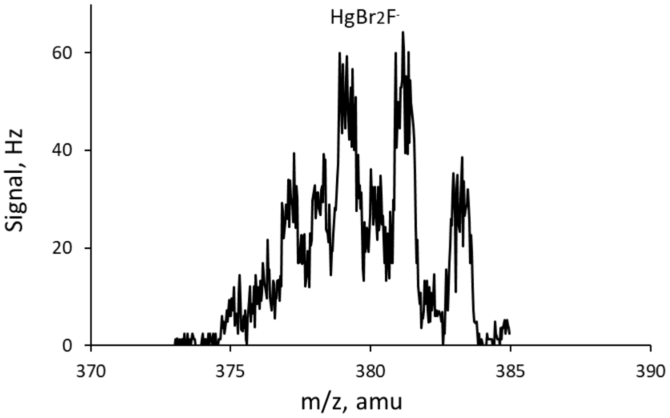

Figure 5.5 The spectrum of $HgBr_2F^-$ detected using SF_6^-.

The ionogram of $HgBr_2F^-$ indicated that $HgBr_2F^-$ signal decreased when reducing the Br_2 and disappeared when turning off the microwave discharge, which means that the $HgBr_2$, which was detected as $HgBr_2F^-$, was formed through the reaction of HgBr in the presence of excess Br (Equations 5.11 and 5.12). We did not observe HgBr using SF_6^-

which may because of the strong electric field (~40 V/cm) in the focusing part of the drift tube, breaking down the intermediate product ion, $HgBr^-$ or $HgBrF^-$. Without such a strong electric field, we cannot obtain sufficient signals for detection.

$$HgBr + Br \overset{M}{\rightarrow} HgBr_2 \tag{5.11}$$

$$HgBr_2 + SF_6^- \rightarrow HgBr_2F^- + SF_5 \tag{5.12}$$

Quantum chemical calculations showed that CH_3COO^- could bind with mercury compounds stronger than SF_6^-, as shown using $HgCl_2$ to check the stability of the product ion in the current electric field (see Section 2.4.5). We found that $HgCl_2$ clustered strongly with CH_3COO^- to form $HgCl_2{\cdot}CH_3COO^-$, which was stable for the detection. Figure 5.6 shows the spectra of $HgBr{\cdot}CH_3COO^-$, $HgBr_2{\cdot}CH_2CO^-$, and $HgBr_2{\cdot}CH_3COO^-$, which were detected during the reaction of Br radical with Hg, using CH_3COO^- as the reagent ion (Equations 5.13-5.15).

$$HgBr + CH_3COO^- \rightarrow HgBr{\cdot}CH_3COO^- \tag{5.13}$$

$$HgBr_2 + CH_3COO^- \rightarrow HgBr_2{\cdot}CH_3COO^- \tag{5.14}$$

$$HgBr_2 + CH_2CO^- \rightarrow HgBr_2{\cdot}CH_2CO^- \tag{5.15}$$

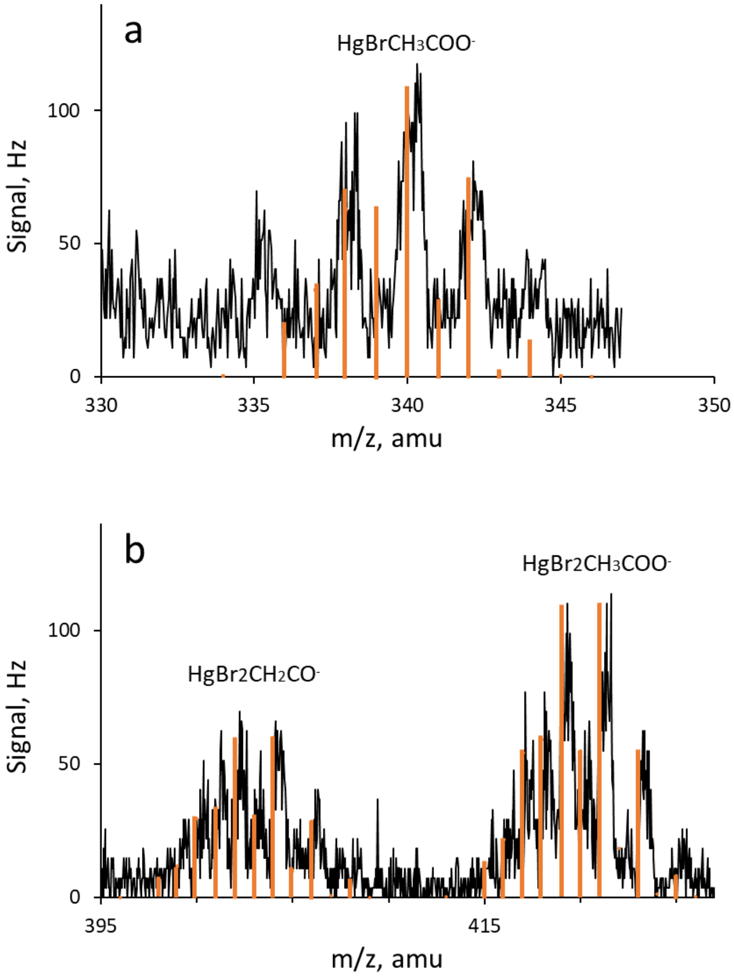

Figure 5.6 The spectra of the reaction product: a) HgBr with CH_3COO^-; and b) $HgBr_2{\cdot}CH_2CO^-$ and $HgBr_2{\cdot}CH_3COO^-$. The orange sticks represent the theoretical spectra.

Future research is to reduce the electric field in the drift tube without compromising the signal intensity, optimize the detection of the intermediate products, determine the rate constant of the reactions of HgBr with atmospherically abundant species, and study the complete mechanism of gas-phase oxidation of elemental mercury.

CHAPTER 6

CONCLUSIONS AND FUTURE WORK

A chemical ionization-mass spectrometry-based technique for the direct detection of gaseous oxidized mercury and the gaseous elemental mercury was developed and utilized to study atmospheric mercury chemistry, including the gas-phase oxidation of GEM, heterogeneous reactions of GOM with both inorganic and organic surfaces, and exchange reactions that can occur during GOM preconcentration.

One of the main results of this dissertation is the introduction of ID-CIMS for the direct detection of GOM and GEM, including the exploration of reagent ions to select the ions appropriate for the detection of $HgCl_2$ and Hg^0. Another important finding of this dissertation is that current detection methods based on preconcentration of GOM cannot provide its molecular speciation because of rapid exchange reactions on the surface of sorbents. A similar scrambling of molecular speciation occurs on the atmospheric aerosols. Moreover, the removal of GOM by both inorganic and organic surfaces was studied, and we concluded that aerosols present a significant sink of GOM. The efficiency of removal depends on the level of particle hydration and particle acidity. Finally, the gas phase oxidation intermediate, HgBr, could be detected using CH_3COO^- and hence its kinetics and mechanism can be studied using ID-CIMS. Overall, the results obtained in this dissertation improve the understanding of the atmospheric mercury chemistry cycle.

The future work will focus on the following: (1) improving the sensitivity of GOM detection by switching to atmospheric pressure chemical ionization; (2) studying the heterogeneous uptake of GOM by the mixed inorganic-organic surfaces and on airborne particles; (3) optimizing the detection of the reaction intermediate HgBr and determining the rate constant of the reactions of HgBr with atmospherically relevant chemical species; (4) studying the complete mechanism of gas-phase oxidation of elemental mercury.

REFERENCES

Ambrose, J. L., Gratz, L. E., Jaffe, D. A., Campos, T., Flocke, F. M., Knapp, D. J., Stechman, D. M., Stell, M., Weinheimer, A. J., & Cantrell, C. A. (2015). Mercury emission ratios from coal-fired power plants in the Southeastern United States during NOMADSS. *Environmental Science & Technology, 49*(17), 10389-10397.

Ambrose, J. L., Lyman, S. N., Huang, J., Gustin, M. S., & Jaffe, D. A. (2013). Fast time resolution oxidized mercury measurements during the Reno Atmospheric Mercury Intercomparison Experiment (RAMIX). *Environmental Science & Technology, 47*(13), 7285-7294.

Amelynck, C., Fussen, D., & Arijs, E. (1994). Reactions of nitric acid with di- and trichloride ions, di- and tri-iodide ions and with CO−4 in the gas phase. *International Journal of Mass Spectrometry and Ion Processes, 133*(1), 13-28. doi:http://dx.doi.org/10.1016/0168-1176(94)03950-X

Ammann, M., Kalberer, M., Jost, D. T., Tobler, L., Rossler, E., Piguet, D., Gaggeler, H. W., & Baltensperger, U. (1998). Heterogeneous production of nitrous acid on soot in polluted air masses. *Nature, 395*(6698), 157-160.

Ammann, M., & Pöschl, U. (2007). Kinetic model framework for aerosol and cloud surface chemistry and gas-particle interactions – Part 2: Exemplary practical applications and numerical simulations. *Atmospheric Chemistry and Physics, 7*(23), 6025-6045. doi:10.5194/acp-7-6025-2007

Ammlung, R., & Brill, T. (1974). The nature of the mixed halides of mercury (II). *Inorganica Chimica Acta, 11*, 201-205.

Amos, H. M., Jacob, D. J., Holmes, C. D., Fisher, J. A., Wang, Q., Yantosca, R. M., Corbitt, E. S., Galarneau, E., Rutter, A. P., Gustin, M. S., Steffen, A., Schauer, J. J., Graydon, J. A., Louis, V. L. S., Talbot, R. W., Edgerton, E. S., Zhang, Y., & Sunderland, E. M. (2012). Gas-particle partitioning of atmospheric Hg(II) and its effect on global mercury deposition. *Atmospheric Chemistry and Physics, 12*(1), 591-603. doi:10.5194/acp-12-591-2012

Appel, B. R., Tokiwa, Y., Povard, V., & Kothny, E. L. (1991). The measurement of atmospheric hydrochloric acid in southern California. *Atmospheric Environment. Part A. General Topics, 25*(2), 525-527. doi:https://doi.org/10.1016/0960-1686(91)90325-2

Arijs, E., Barassin, A., Kopp, E., Amelynck, C., Catoire, V., Fink, H. P., Guimbaud, C., Jenzer, U., Labonnette, D., Luithardt, W., Neefs, E., Nevejans, D., Schoon, N., & Van Bavel, A. M. (1998). Stratospheric chemical ionization mass spectrometry: nitric acid detection by different ion molecule reaction schemes. *International Journal of Mass Spectrometry, 181*, 99-111.

Ariya, P. A., Khalizov, A., & Gidas, A. (2002). Reactions of Gaseous Mercury with Atomic and Molecular Halogens: Kinetics, Product Studies, and Atmospheric Implications. *Journal of Physical Chemistry A, 106*(32), 7310-7320.

Arnold, S. T., Morris, R. A., Viggiano, A. A., & Jayne, J. T. (1995). Ion chemistry relevant for chemical ionization detection of SO3. *Journal of Geophysical Research: Atmospheres, 100*(D7), 14141-14146. doi:10.1029/95jd01004

Arnold, S. T., & Viggiano, A. A. (2001). Turbulent Ion Flow Tube Study of the Cluster-Mediated Reactions of SF6- with H2O, CH3OH, and C2H5OH from 50 to 500 Torr. *The Journal of Physical Chemistry A, 105*(14), 3527-3531. doi:10.1021/jp003967y

Athanasopoulou, E., Tombrou, M., Pandis, S. N., & Russell, A. G. (2008). The role of sea-salt emissions and heterogeneous chemistry in the air quality of polluted coastal areas. *Atmospheric Chemistry and Physics, 8*(19), 5755-5769. doi:10.5194/acp-8-5755-2008

Aubin, D. G., & Abbatt, J. P. D. (2007). Interaction of NO_2 with hydrocarbon soot: Focus on HONO yield, surface modification, and mechanism. *Journal of Physical Chemistry A 111*(28), 6263-6273. doi:10.1021/jp068884h

Balabanov, N. B., & Peterson, K. A. (2003). Mercury and reactive halogens: The thermochemistry of Hg+{Cl-2, Br-2, BrCl, ClO, and BrO}. *Journal of Physical Chemistry A, 107*(38), 7465-7470.

Beattie, I. R., & Horder, J. R. (1970). Gas-phase Raman spectra of some dihalides of zinc and mercury, of ‘GaCl2’ and of GaCl2Br and GaBr2Cl. *Journal of the Chemical Society A: Inorganic, Physical, Theoretical*(0), 2433-2435. doi:10.1039/J19700002433

Bernard, L., Awitor, K., Badaud, J., Bonnin, O., Coupat, B., Fournier, J., & Verdier, P. (1997). Détermination de la pression de vapeur de HgCl2 par la méthode d'effusion de Knudsen. *Journal de Physique III, 7*(2), 311-319.

Bianchi, F., Kurtén, T., Riva, M., Mohr, C., Rissanen, M. P., Roldin, P., Berndt, T., Crounse, J. D., Wennberg, P. O., Mentel, T. F., Wildt, J., Junninen, H., Jokinen, T., Kulmala, M., Worsnop, D. R., Thornton, J. A., Donahue, N., Kjaergaard, H. G., & Ehn, M. (2019). Highly Oxygenated Organic Molecules (HOM) from Gas-Phase Autoxidation Involving Peroxy Radicals: A Key Contributor to Atmospheric Aerosol. *Chemical Reviews*. doi:10.1021/acs.chemrev.8b00395

Bierbach, A., Barnes, I., & Becker, K. (1996). Rate coefficients for the gas - phase reactions of bromine radicals with a series of alkenes, dienes, and aromatic hydrocarbons at 298 ± 2 K. *International Journal of Chemical Kinetics, 28*(8), 565-577.

Bigg, E. K., Ono, A., & Williams, J. A. (1974). Chemical tests for individual submicron aerosol particles. *Atmospheric Environment (1967), 8*(1), 1-13. doi:https://doi.org/10.1016/0004-6981(74)90107-3

Brophy, P., & Farmer, D. K. (2016). Clustering, methodology, and mechanistic insights into acetate chemical ionization using high-resolution time-of-flight mass spectrometry. *Atmospheric Measurement Techniques, 9*(8), 3969-3986.

Brosset, C., & Lord, E. (1995). Methylmercury in ambient air. Method of determination and some measurement results. *Water, Air, and Soil Pollution, 82*(3), 739-750.

Bruno, M., Aquilano, D., Pastero, L., & Prencipe, M. (2008). Structures and Surface Energies of (100) and Octopolar (111) Faces of Halite (NaCl): an Ab initio Quantum-Mechanical and Thermodynamical Study. *Crystal Growth & Design, 8*(7), 2163-2170. doi:10.1021/cg8000027

Butt, H., Graf, K., & Kappl, M. (2003). *Physics and Chemistry of Interfaces*. Weinheim, Germany: Wiley-VCH.

Calvert, J. G., & Lindberg, S. E. (2003). A modeling study of the mechanism of the halogen–ozone–mercury homogeneous reactions in the troposphere during the polar spring. *Atmospheric Environment, 37*(32), 4467-4481.

Calvert, J. G., & Lindberg, S. E. (2005). Mechanisms of mercury removal by O3 and OH in the atmosphere. *Atmospheric Environment, 39*(18), 3355-3367.

Cheng, Y. F., Berghof, M., Garland, R. M., Wiedensohler, A., Wehner, B., Muller, T., Su, H., Zhang, Y. H., Achtert, P., Nowak, A., Poschl, U., Zhu, T., Hu, M., & Zeng, L. M. (2009). Influence of soot mixing state on aerosol light absorption and single scattering albedo during air mass aging at a polluted regional site in northeastern China. *Journal of Geophysical Research, 114*, 10.1029/2008JD010883. doi:10.1029/2008JD010883

Choi, H., Huang, J., Mondal, S., & Holsen, T. M. (2013). Variation in concentrations of three mercury (Hg) forms at a rural and a suburban site in New York State. *Science of the Total Environment, 448*, 96-106.

Chowhan, Z. (1978). pH ‐ solubility profiles of organic carboxylic acids and their salts. *Journal of Pharmaceutical Sciences, 67*(9), 1257-1260.

Colosimo, M., Caponecchi, G., & Brancaleoni, E. (1985). Proton and methyl cation attack during CIMS of bromocyclopropane. *International Journal of Mass Spectrometry and Ion Processes, 65*(3), 263-271.

Cotton, F. A., & Wilkinson, G. (1980). *Advanced inorganic chemistry: a comprehensive text* (4th ed.). New York, USA: Wiley.

Cremer, D., Kraka, E., & Filatov, M. (2008). Bonding in Mercury Molecules Described by the Normalized Elimination of the Small Component and Coupled Cluster Theory. *Chemphyschem, 9*(17), 2510-2521. doi:10.1002/cphc.200800510

Crisp, T. A., Lerner, B. M., Williams, E. J., Quinn, P. K., Bates, T. S., & Bertram, T. H. (2014). Observations of gas phase hydrochloric acid in the polluted marine boundary layer. *Journal of Geophysical Research: Atmospheres, 119*(11), 6897-6915. doi:https://doi.org/10.1002/2013JD020992

Davidovits, P., Kolb, C. E., Williams, L. R., Jayne, J. T., & Worsnop, D. R. (2006). Mass accommodation and chemical reactions at gas− liquid interfaces. *Chemical Reviews, 106*(4), 1323-1354.

Davidovits, P., Kolb, C. E., Williams, L. R., Jayne, J. T., & Worsnop, D. R. (2011). Update 1 of: Mass Accommodation and Chemical Reactions at Gas−Liquid Interfaces. *Chemical Reviews 111*(4), PR76– PR109. doi:10.1021/cr100360b

Day, T. (2014). *Ecosystems: Oceans*. London, UK: Routledge.

de Gouw, J., Warneke, C., Karl, T., Eerdekens, G., van der Veen, C., & Fall, R. (2003). Sensitivity and specificity of atmospheric trace gas detection by proton-transfer-reaction mass spectrometry. *International Journal of Mass Spectrometry, 223-224*, 365-382. doi:https://doi.org/10.1016/S1387-3806(02)00926-0

De Haan, D. O., Brauers, T., Oum, K., Stutz, J., Nordmeyer, T., & Finlayson-Pitts, B. J. (1999). Heterogeneous chemistry in the troposphere: Experimental approaches and applications to the chemistry of sea salt particles. *International Reviews in Physical Chemistry*, *18*(3), 343-385. doi:10.1080/014423599229910

Deeds, D. A., Ghoshdastidar, A., Raofie, F., Guerette, E. A., Tessier, A., & Ariya, P. A. (2015). Development of a particle-trap preconcentration-soft ionization mass spectrometric technique for the quantification of mercury halides in air. *Analytical Chemistry, 87*(10), 5109-5116. doi:10.1021/ac504545w

Deng, C., Tong, Y., Chen, L., Yuan, W., Sun, Y., Li, J., Wang, X., Zhang, W., Lin, H., Xie, H., & Bu, X. (2019). Impact of particle chemical composition and water content on the photolytic reduction of particle-bound mercury. *Atmospheric Environment*, *200*, 24-33. doi:https://doi.org/10.1016/j.atmosenv.2018.11.054

Dibble, T. S., Zelie, M. J., & Jiao, Y. (2014). Quantum Chemistry Guide to PTRMS Studies of As-Yet Undetected Products of the Bromine-Atom Initiated Oxidation of Gaseous Elemental Mercury. *The Journal of Physical Chemistry A, 118*(36), 7847-7854. doi:10.1021/jp5041426

Dibble, T. S., Zelie, M. J., & Mao, H. (2012). Thermodynamics of reactions of ClHg and BrHg radicals with atmospherically abundant free radicals. *Atmospheric Chemistry and Physics 12*(21), 10271-10279. doi:10.5194/acp-12-10271-2012

Donohoue, D. L., Bauer, D., Cossairt, B., & Hynes, A. J. (2006). Temperature and pressure dependent rate coefficients for the reaction of Hg with Br and the reaction of Br with Br: A pulsed laser photolysis-pulsed laser induced fluorescence study. *Journal of Physical Chemistry A, 110*(21), 6623-6632.

Donohoue, D. L., Bauer, D., & Hynes, A. J. (2005). Temperature and pressure dependent rate coefficients for the reaction of Hg with Cl and the reaction of Cl with Cl: A pulsed laser photolysis-pulsed laser induced fluorescence study. *Journal of Physical Chemistry A, 109*(34), 7732-7741.

Dunham-Cheatham, S. M., Lyman, S., & Gustin, M. S. (2020). Evaluation of sorption surface materials for reactive mercury compounds. *Atmospheric Environment, 242*, 117836.

Ebinghaus, R., Jennings, S., Schroeder, W., Berg, T., Donaghy, T., Guentzel, J., Kenny, C., Kock, H., Kvietkus, K., & Landing, W. (1999). International field intercomparison measurements of atmospheric mercury species at Mace Head, Ireland. *Atmospheric Environment, 33*(18), 3063-3073.

Ebinghaus, R., Kock, H. H., Temme, C., Einax, J. W., Löwe, A. G., Richter, A., Burrows, J. P., & Schroeder, W. H. (2002). Antarctic springtime depletion of atmospheric mercury. *Environmental Science & Technology, 36*(6), 1238-1244.

Edgerton, E. S., Hartsell, B. E., & Jansen, J. J. (2006). Mercury Speciation in Coal-fired Power Plant Plumes Observed at Three Surface Sites in the Southeastern U.S. *Environmental Science & Technology, 40*(15), 4563-4570. doi:10.1021/es0515607

Ehn, M., Thornton, J. A., Kleist, E., Sipilä, M., Junninen, H., Pullinen, I., Springer, M., Rubach, F., Tillmann, R., Lee, B., Lopez-Hilfiker, F., Andres, S., Acir, I.-H., Rissanen, M., Jokinen, T., Schobesberger, S., Kangasluoma, J., Kontkanen, J., Nieminen, T., Kurtén, T., Nielsen, L. B., Jørgensen, S., Kjaergaard, H. G., Canagaratna, M., Maso, M. D., Berndt, T., Petäjä, T., Wahner, A., Kerminen, V.-M., Kulmala, M., Worsnop, D. R., Wildt, J., & Mentel, T. F. (2014). A large source of low-volatility secondary organic aerosol. *Nature, 506*, 476. doi:10.1038/nature13032

Eisele, F. L., & Hanson, D. R. (2000). First measurement of prenucleation molecular clusters. *Journal of Physical Chemistry A 104*(4), 830-836.

Eisele, F. L., & Tanner, D. J. (1991). Ion-assisted tropospheric OH measurements. *Journal of Geophysical Research: Atmosphere, 96*(D5), 9295-9308.

Eisele, F. L., & Tanner, D. J. (1993). Measurement of the gas-phase concentration of H2SO4 and methane sulfonic-acid and estimates of H2SO4 production and loss in the atmosphere. *Journal of Geophysical Research: Atmosphere, 98*(D5), 9001-9010.

Ernest, C., Donohoue, D., Bauer, D., Schure, A., & Hynes, A. (2014). Programmable Thermal Dissociation of Reactive Gaseous Mercury, a Potential Approach to Chemical Speciation: Results from a Field Study. *Atmosphere, 5*(3), 575.

Feng, X., Sommar, J., Gårdfeldt, K., & Lindqvist, O. (2000). Improved determination of gaseous divalent mercury in ambient air using KCl coated denuders. *Fresenius' Journal of Analytical Chemistry, 366*(5), 423-428.

Ferguson, E. E., Fehsenfeld, F. C., & Schmeltekopf, A. L. (1969). Flowing Afterglow Measurements of Ion-Neutral Reactions. In Bates, D. R. & Estermann, I. (Eds.), *Advances in Atomic and Molecular Physics* (Vol. 5, pp. 1-56): Academic Press.

Fortner, E. C., Zhao, J., & Zhang, R. (2004). Development of ion drift-chemical ionization mass spectrometry. *Analytical Chemistry, 76*(18), 5436-5440.

Francés-Monerris, A., Carmona-García, J., Acuña, A. U., Dávalos, J. Z., Cuevas, C. A., Kinnison, D. E., Francisco, J. S., Saiz-Lopez, A., & Roca-Sanjuán, D. (2020). Photodissociation Mechanisms of Major Mercury(II) Species in the Atmospheric Chemical Cycle of Mercury. *Angewandte Chemie International Edition, 59*(19), 7605-7610. doi:10.1002/anie.201915656

Ge, X., Setyan, A., Sun, Y., & Zhang, Q. (2012). Primary and secondary organic aerosols in Fresno, California during wintertime: Results from high resolution aerosol mass spectrometry. *Journal of Geophysical Research: Atmospheres, 117*(D19).

Gershenzon, Y. M., Grigorieva, V. M., Ivanov, A. V., & Remorov, R. G. (1995). O_3 and OH Sensitivity to heterogeneous sinks of HO and CH_3O_2 on aerosol particles. *Faraday Discussions, 100*(0), 83-100. doi:10.1039/FD9950000083

Givan, A., & Loewenschuss, A. (1976a). The infrared and Raman spectra of matrix isolated binary and mixed mercury halides. *The Journal of Chemical Physics, 64*(5), 1967-1972.

Givan, A., & Loewenschuss, A. (1976b). The infrared and Raman spectra of matrix isolated binary and mixed mercury halides. II. Extension to low frequencies. *The Journal of Chemical Physics, 65*(5), 1851-1853.

Goodsite, M. E., Plane, J. M. C., & Skov, H. (2004). A theoretical study of the oxidation of Hg-0 to HgBr2 in the troposphere. *Environmental Science & Technology, 38*(6), 1772-1776.

Gustin, M. S., Amos, H. M., Huang, J., Miller, M. B., & Heidecorn, K. (2015). Measuring and modeling mercury in the atmosphere: a critical review. *Atmospheric Chemistry and Physics, 15*(10), 5697-5713. doi:10.5194/acp-15-5697-2015

Gustin, M. S., Dunham-Cheatham, S. M., Huang, J., Lindberg, S. E., & Lyman, S. N. (2021a). Development of an Understanding of Reactive Mercury in Ambient Air: A Review. *Atmosphere, 12*(1), 73.

Gustin, M. S., Dunham-Cheatham, S. M., & Zhang, L. (2019). Comparison of 4 Methods for Measurement of Reactive, Gaseous Oxidized, and Particulate Bound Mercury. *Environmental Science & Technology, 53*(24), 14489-14495. doi:10.1021/acs.est.9b04648

Gustin, M. S., Dunham-Cheatham, S. M., Zhang, L., Lyman, S., Choma, N., & Castro, M. (2021b). Use of membranes and detailed HYSPLIT analyses to understand atmospheric particulate, gaseous oxidized, and reactive mercury chemistry. *Environmental Science & Technology, 55*(2), 893-901.

Gustin, M. S., Huang, J., Miller, M. B., Peterson, C., Jaffe, D. A., Ambrose, J., Finley, B. D., Lyman, S. N., Call, K., Talbot, R., Feddersen, D., Mao, H., & Lindberg, S. E. (2013). Do We Understand What the Mercury Speciation Instruments Are Actually Measuring? Results of RAMIX. *Environmental Science & Technology, 47*(13), 7295-7306. doi:10.1021/es3039104

Gustin, M. S., Pierce, A. M., Huang, J., Miller, M. B., Holmes, H. A., & Loria-Salazar, S. M. (2016). Evidence for Different Reactive Hg Sources and Chemical Compounds at Adjacent Valley and High Elevation Locations. *Environmental Science & Technology, 50*(22), 12225-12231. doi:10.1021/acs.est.6b03339

Hall, B. (1995). The gas phase oxidation of elemental mercury by ozone. In *Mercury as a Global Pollutant* (pp. 301-315): Springer.

Hanson, D. R., Greenberg, J., Henry, B. E., & Kosciuch, E. (2003). Proton transfer reaction mass spectrometry at high drift tube pressure. *International Journal of Mass Spectrometry, 223–224*(0), 507-518. doi:http://dx.doi.org/10.1016/S1387-3806(02)00924-7

Hanson, D. R., Koppes, M., Stoffers, A., Harsdorf, R., & Edelen, K. (2009). Proton transfer mass spectrometry at 11 hPa with a circular glow discharge: Sensitivities and applications. *International Journal of Mass Spectrometry, 282*(1-2), 28-37.

Hanson, D. R., McMurry, P. H., Jiang, J., Tanner, D., & Huey, L. G. (2011). Ambient Pressure Proton Transfer Mass Spectrometry: Detection of Amines and Ammonia. *Environmental Science & Technology, 45*(20), 8881-8888. doi:10.1021/es201819a

Harrison, R. M., & Allen, A. G. (1990). Measurements of atmospheric HNO3, HCl and associated species on a small network in eastern England. *Atmospheric Environment. Part A. General Topics, 24*(2), 369-376. doi:https://doi.org/10.1016/0960-1686(90)90116-5

Heintzenberg, J. (1989). Fine particles in the global troposphere A review. *Tellus B, 41*(2), 149-160.

Holmes, C. D., Jacob, D. J., Corbitt, E. S., Mao, J., Yang, X., Talbot, R., & Slemr, F. (2010). Global atmospheric model for mercury including oxidation by bromine atoms. *Atmospheric Chemistry and Physics, 10*(24), 12037-12057. doi:10.5194/acp-10-12037-2010

Holmes, C. D., Jacob, D. J., Mason, R. P., & Jaffe, D. A. (2009). Sources and deposition of reactive gaseous mercury in the marine atmosphere. *Atmospheric Environment 43*(14), 2278-2285.

Holmes, C. D., Jacob, D. J., & Yang, X. (2006). Global lifetime of elemental mercury against oxidation by atomic bromine in the free troposphere. *Geophysical Research Letters, 33*(20), L20808. doi:10.1029/2006GL027176

Horowitz, H. M., Jacob, D. J., Zhang, Y., Dibble, T. S., Slemr, F., Amos, H. M., Schmidt, J. A., Corbitt, E. S., Marais, E. A., & Sunderland, E. M. (2017). A new mechanism for atmospheric mercury redox chemistry: implications for the global mercury budget. *Atmospheric Chemistry and Physics, 17*(10), 6353-6371. doi:10.5194/acp-17-6353-2017

Howard, C. J. (1979). Kinetic measurements using flow tubes. *Journal of Physical Chemistry, 83*(1), 3-9.

Huang, J., & Gustin, M. S. (2015). Uncertainties of gaseous oxidized mercury measurements using KCl-coated denuders, cation-exchange membranes, and nylon membranes: Humidity influences. *Environmental Science & Technology, 49*(10), 6102-6108.

Huang, J., Lyman, S. N., Hartman, J. S., & Gustin, M. S. (2014). A review of passive sampling systems for ambient air mercury measurements. *Environmental Science: Processes & Impacts, 16*(3), 374-392. doi:10.1039/C3EM00501A

Huang, J., Miller, M. B., Weiss-Penzias, P., & Gustin, M. S. (2013). Comparison of Gaseous Oxidized Hg Measured by KCl-Coated Denuders, and Nylon and Cation Exchange Membranes. *Environmental Science & Technology, 47*(13), 7307-7316. doi:10.1021/es4012349

Huey, L. G. (2007). Measurement of trace atmospheric species by chemical ionization mass spectrometry: Speciation of reactive nitrogen and future directions. *Mass Spectrometry Reviews 26*(2), 166-184. doi:10.1002/mas.20118

Huey, L. G., Hanson, D. R., & Howard, C. J. (1995). Reactions of SF6- and I- with Atmospheric Trace Gases. *The Journal of Physical Chemistry, 99*(14), 5001-5008. doi:10.1021/j100014a021

Hyttinen, N., Kupiainen-Määttä, O., Rissanen, M. P., Muuronen, M., Ehn, M., & Kurtén, T. (2015). Modeling the Charging of Highly Oxidized Cyclohexene Ozonolysis Products Using Nitrate-Based Chemical Ionization. *The Journal of Physical Chemistry A, 119*(24), 6339-6345. doi:10.1021/acs.jpca.5b01818

Impey, G., Shepson, P., Hastie, D., Barrie, L., & Anlauf, K. (1997). Measurements of photolyzable chlorine and bromine during the Polar Sunrise Experiment 1995. *Journal of Geophysical Research: Atmospheres, 102*(D13), 16005-16010.

Inomata, S., & Hirokawa, J. (2017). Non-radioactive Chemical Ionization Mass Spectrometry Using Acetic Acid–Acetate Cluster as a Reagent Ion for the Real-time Measurement of Acids and Hydroperoxides. *Chemistry Letters, 46*(1), 38-41.

Jaffe, D. A., Lyman, S., Amos, H. M., Gustin, M. S., Huang, J., Selin, N. E., Levin, L., ter Schure, A., Mason, R. P., Talbot, R., Rutter, A., Finley, B., Jaeglé, L., Shah, V., McClure, C., Ambrose, J., Gratz, L., Lindberg, S., Weiss-Penzias, P., Sheu, G.-R., Feddersen, D., Horvat, M., Dastoor, A., Hynes, A. J., Mao, H., Sonke, J. E., Slemr, F., Fisher, J. A., Ebinghaus, R., Zhang, Y., & Edwards, G. (2014). Progress on Understanding Atmospheric Mercury Hampered by Uncertain Measurements. *Environmental Science & Technology, 48*(13), 7204-7206. doi:10.1021/es5026432

Jang, M., Czoschke, N. M., Lee, S., & Kamens, R. M. (2002). Heterogeneous atmospheric aerosol production by acid-catalyzed particle-phase reactions. *Science, 298*(5594), 814-817.

Janz, G. J., & James, D. W. (1963). Vibrational Spectra of Molten Halides of Mercury. I. Mercuric Chloride, Mercuric Bromide, and Mercury Chlorobromide. *The Journal of Chemical Physics, 38*(4), 902-905.

Jiang, S., Cai, L., Yang, J., Peng, H., Liu, H., & Li, H. (2020). HgCl2 reduction under a low-temperature selective catalytic reduction atmosphere. *Energy & Fuels, 34*(2), 2417-2424.

Jiao, Y., & Dibble, T. S. (2015). Quality Structures, Vibrational Frequencies, and Thermochemistry of the Products of Reaction of BrHg• with NO2, HO2, ClO, BrO, and IO. *The Journal of Physical Chemistry A, 119*(42), 10502-10510. doi:10.1021/acs.jpca.5b04889

Jiao, Y., & Dibble, T. S. (2017a). First kinetic study of the atmospherically important reactions BrHg+ NO 2 and BrHg+ HOO. *Physical Chemistry Chemical Physics, 19*(3), 1826-1838.

Jiao, Y., & Dibble, T. S. (2017b). Structures, Vibrational Frequencies, and Bond Energies of the BrHgOX and BrHgXO Species Formed in Atmospheric Mercury Depletion Events. *The Journal of Physical Chemistry A, 121*(41), 7976-7985. doi:10.1021/acs.jpca.7b06829

Jimenez, J. L., Canagaratna, M. R., Donahue, N. M., Prevot, A. S. H., Zhang, Q., Kroll, J. H., DeCarlo, P. F., Allan, J. D., Coe, H., Ng, N. L., Aiken, A. C., Docherty, K. S., Ulbrich, I. M., Grieshop, A. P., Robinson, A. L., Duplissy, J., Smith, J. D., Wilson, K. R., Lanz, V. A., Hueglin, C., Sun, Y. L., Tian, J., Laaksonen, A., Raatikainen, T., Rautiainen, J., Vaattovaara, P., Ehn, M., Kulmala, M., Tomlinson, J. M., Collins, D. R., Cubison, M. J., E., Dunlea, J., Huffman, J. A., Onasch, T. B., Alfarra, M. R., Williams, P. I., Bower, K., Kondo, Y., Schneider, J., Drewnick, F., Borrmann, S., Weimer, S., Demerjian, K., Salcedo, D., Cottrell, L., Griffin, R., Takami, A., Miyoshi, T., Hatakeyama, S., Shimono, A., Sun, J. Y., Zhang, Y. M., Dzepina, K., Kimmel, J. R., Sueper, D., Jayne, J. T., Herndon, S. C., Trimborn, A. M., Williams, L. R., Wood, E. C., Middlebrook, A. M., Kolb, C. E., Baltensperger, U., & Worsnop, D. R. (2009). Evolution of Organic Aerosols in the Atmosphere. *Science, 326*(5959), 1525-1529. doi:10.1126/science.1180353

Jones, C. P., Lyman, S. N., Jaffe, D. A., Allen, T., & O'Neil, T. L. (2016). Detection and quantification of gas-phase oxidized mercury compounds by GC/MS. *Atmospheric Measurement Techniques*, *9*(5), 2195-2205. doi:10.5194/amt-9-2195-2016

Jordan, A., Haidacher, S., Hanel, G., Hartungen, E., Märk, L., Seehauser, H., Schottkowsky, R., Sulzer, P., & Märk, T. (2009). A high resolution and high sensitivity proton-transfer-reaction time-of-flight mass spectrometer (PTR-TOF-MS). *International Journal of Mass Spectrometry, 286*(2-3), 122-128.

Jost, C., Sprung, D., Kenntner, T., & Reiner, T. (2003). Atmospheric pressure chemical ionization mass spectrometry for the detection of tropospheric trace gases: the influence of clustering on sensitivity and precision. *International Journal of Mass Spectrometry*, *223-224*, 771-782. doi:https://doi.org/10.1016/S1387-3806(02)00963-6

Keene, W. C., Galloway, J. N., & Holden Jr, J. D. (1983). Measurement of weak organic acidity in precipitation from remote areas of the world. *Journal of Geophysical Research: Oceans, 88*(C9), 5122-5130.

Khalizov, A. F., Cruz-Quinones, M., & Zhang, R. (2010). Heterogeneous reaction of NO2 on fresh and coated soot surfaces. *The Journal of Physical Chemistry A, 114*(28), 7516-7524.

Khalizov, A. F., Guzman, F. J., Cooper, M., Mao, N., Antley, J., & Bozzelli, J. (2020). Direct detection of gas-phase mercuric chloride by ion drift - chemical ionization mass spectrometry. *Atmospheric Environment*, *238*, 117687. doi:https://doi.org/10.1016/j.atmosenv.2020.117687

Khalizov, A. F., Viswanathan, B., Larregaray, P., & Ariya, P. A. (2003). A theoretical study on the reactions of Hg with halogens: Atmospheric implications. *Journal of Physical Chemistry A, 107*(33), 6360-6365.

Kılıç, M., Keskin, M. E., Mazlum, S., & Mazlum, N. (2008). Hg (II) and Pb (II) adsorption on activated sludge biomass: effective biosorption mechanism. *International Journal of Mineral Processing, 87*(1-2), 1-8.

Kirkby, J., Duplissy, J., Sengupta, K., Frege, C., Gordon, H., Williamson, C., Heinritzi, M., Simon, M., Yan, C., Almeida, J., Tröstl, J., Nieminen, T., Ortega, I. K., Wagner, R., Adamov, A., Amorim, A., Bernhammer, A.-K., Bianchi, F., Breitenlechner, M., Brilke, S., Chen, X., Craven, J., Dias, A., Ehrhart, S., Flagan, R. C., Franchin, A., Fuchs, C., Guida, R., Hakala, J., Hoyle, C. R., Jokinen, T., Junninen, H., Kangasluoma, J., Kim, J., Krapf, M., Kürten, A., Laaksonen, A., Lehtipalo, K., Makhmutov, V., Mathot, S., Molteni, U., Onnela, A., Peräkylä, O., Piel, F., Petäjä, T., Praplan, A. P., Pringle, K., Rap, A., Richards, N. A. D., Riipinen, I., Rissanen, M. P., Rondo, L., Sarnela, N., Schobesberger, S., Scott, C. E., Seinfeld, J. H., Sipilä, M., Steiner, G., Stozhkov, Y., Stratmann, F., Tomé, A., Virtanen, A., Vogel, A. L., Wagner, A. C., Wagner, P. E., Weingartner, E., Wimmer, D., Winkler, P. M., Ye, P., Zhang, X., Hansel, A., Dommen, J., Donahue, N. M., Worsnop, D. R., Baltensperger, U., Kulmala, M., Carslaw, K. S., & Curtius, J. (2016). Ion-induced nucleation of pure biogenic particles. *Nature, 533*(7604), 521-526. doi:10.1038/nature17953

Knop, G., & Arnold, F. (1985). Nitric acid vapour measurements in the troposphere and lower stratosphere by chemical ionisation mass spectrometry. *Planetary and Space Science, 33*(8), 983-986. doi:https://doi.org/10.1016/0032-0633(85)90111-4

Kroll, J. H., Donahue, N. M., Jimenez, J. L., Kessler, S. H., Canagaratna, M. R., Wilson, K. R., Altieri, K. E., Mazzoleni, L. R., Wozniak, A. S., & Bluhm, H. (2011). Carbon oxidation state as a metric for describing the chemistry of atmospheric organic aerosol. *Nature Chemistry, 3*(2), 133.

Křůmal, K., Mikuška, P., & Večeřa, Z. (2009). Sources, Occurrence and Analysis of Carboxylic Acids in Atmosphere. *Chemické Listy, 103*(4).

Lam, K. T., Wilhelmsen, C. J., & Dibble, T. S. (2019a). BrHgO• + C2H4 and BrHgO• + HCHO in Atmospheric Oxidation of Mercury: Determining Rate Constants of Reactions with Prereactive Complexes and Bifurcation. *The Journal of Physical Chemistry A, 123*(28), 6045-6055. doi:10.1021/acs.jpca.9b05120

Lam, K. T., Wilhelmsen, C. J., Schwid, A. C., Jiao, Y., & Dibble, T. S. (2019b). Computational Study on the Photolysis of BrHgONO and the Reactions of BrHgO• with CH_4, C_2H_6, NO, and NO_2: Implications for Formation of Hg(II) Compounds in the Atmosphere. *The Journal of Physical Chemistry A, 123*(8), 1637-1647. doi:10.1021/acs.jpca.8b11216

Landis, M. S., Ryan, J. V., ter Schure, A. F. H., & Laudal, D. (2014). Behavior of Mercury Emissions from a Commercial Coal-Fired Power Plant: The Relationship between Stack Speciation and Near-Field Plume Measurements. *Environmental Science & Technology, 48*(22), 13540-13548. doi:10.1021/es500783t

Landis, M. S., Stevens, R. K., Schaedlich, F., & Prestbo, E. M. (2002). Development and Characterization of an Annular Denuder Methodology for the Measurement of Divalent Inorganic Reactive Gaseous Mercury in Ambient Air. *Environmental Science & Technology, 36*(13), 3000-3009. doi:10.1021/es015887t

Laurier, F., & Mason, R. (2007). Mercury concentration and speciation in the coastal and open ocean boundary layer. *Journal of Geophysical Research: Atmospheres, 112*(D6). doi:https://doi.org/10.1029/2006JD007320

Laurier, F. J. G. (2003). Reactive gaseous mercury formation in the North Pacific Ocean's marine boundary layer: A potential role of halogen chemistry. *Journal of Geophysical Research, 108*(D17), 4529. doi:10.1029/2003jd003625

Levy, M., Zhang, R., Zheng, J., Zhang, A. L., Xu, W., Gomez-Hernandez, M., Wang, Y., & Olaguer, E. (2014). Measurements of nitrous acid (HONO) using ion drift-chemical ionization mass spectrometry during the 2009 SHARP field campaign. *Atmospheric Environment, 94*, 231-240. doi:https://doi.org/10.1016/j.atmosenv.2014.05.024

Levy, M. E., Zhang, R., Khalizov, A. F., Zheng, J., Collins, D. R., Glen, C. R., Wang, Y., Yu, X.-Y., Luke, W., Jayne, J. T., & Olaguer, E. (2013). Measurements of submicron aerosols in Houston, Texas during the 2009 SHARP field campaign. *Journal of Geophysical Research: Atmospheres, 118*(18), 10,518-510,534. doi:10.1002/jgrd.50785

Lewis, E. R., & Schwartz, S. E. (2004). *Sea salt aerosol production : mechanisms, methods, measurements and models : a critical review*. Washington, DC: American Geophysical Union.

Li, J., Forrester, S. M., & Knopf, D. A. (2020). Heterogeneous oxidation of amorphous organic aerosol surrogates by O3, NO3, and OH at typical tropospheric temperatures. *Atmospheric Chemistry and Physics, 20*(10), 6055-6080. doi:10.5194/acp-20-6055-2020

Limbeck, A., Kulmala, M., & Puxbaum, H. (2003). Secondary organic aerosol formation in the atmosphere via heterogeneous reaction of gaseous isoprene on acidic particles. *Geophysical Research Letters, 30*(19).

Lin, C., & Pehkonen, S. O. (1999). The chemistry of atmospheric mercury: a review. *Atmospheric Environment, 33*(13), 2067-2079.

Lin, C., Pongprueksa, P., Lindberg, S. E., Pehkonen, S. O., Byun, D., & Jang, C. (2006). Scientific uncertainties in atmospheric mercury models I: Model science evaluation. *Atmospheric Environment, 40*(16), 2911-2928. doi:http://dx.doi.org/10.1016/j.atmosenv.2006.01.009

Lindberg, Brooks, S., Lin, C.-J., Scott, K. J., Landis, M. S., Stevens, R. K., Goodsite, M., & Richter, A. (2002). Dynamic oxidation of gaseous mercury in the Arctic troposphere at polar sunrise. *Environmental Science & Technology, 36*(6), 1245-1256.

Lindberg, Bullock, R., Ebinghaus, R., Engstrom, D., Feng, X., Fitzgerald, W., Pirrone, N., Prestbo, E., & Seigneur, C. (2007). A synthesis of progress and uncertainties in attributing the sources of mercury in deposition. *Ambio,* 19-32.

Lindberg, S. E., & Stratton, W. (1998). Atmospheric mercury speciation: Concentrations and behavior of reactive gaseous mercury in ambient air. *Environmental Science & Technology, 32*(1), 49-57.

Lindinger, W., Hansel, A., & Jordan, A. (1998). On-line monitoring of volatile organic compounds at pptv levels by means of proton-transfer-reaction mass spectrometry (PTR-MS) medical applications, food control and environmental research. *International Journal of Mass Spectrometry and Ion Processes, 173*(3), 191-241.

Lindqvist, O., & Rodhe, H. (1985). Atmosphere mercury - a review. *TELLUS, 37 B*(3), 136-159.

Luippold, A., Gustin, M. S., Dunham-Cheatham, S. M., & Zhang, L. (2020). Improvement of quantification and identification of atmospheric reactive mercury. *Atmospheric Environment, 224*, 117307.

Lyman, Cheng, I., Gratz, L. E., Weiss-Penzias, P., & Zhang, L. (2020a). An updated review of atmospheric mercury. *Science of the Total Environment, 707,* 135575. doi:10.1016/j.scitotenv.2019.135575

Lyman, S. N., Cheng, I., Gratz, L. E., Weiss-Penzias, P., & Zhang, L. (2020b). An updated review of atmospheric mercury. *Science of The Total Environment, 707*, 135575. doi:https://doi.org/10.1016/j.scitotenv.2019.135575

Lyman, S. N., Gratz, L. E., Dunham-Cheatham, S. M., Gustin, M. S., & Luippold, A. (2020c). Improvements to the Accuracy of Atmospheric Oxidized Mercury Measurements. *Environmental Science & Technology, 54*(21), 13379-13388. doi:10.1021/acs.est.0c02747

Lyman, S. N., & Jaffe, D. A. (2012). Formation and fate of oxidized mercury in the upper troposphere and lower stratosphere. *Nature Geoscience*, *5*(2), 114-117.

Lyman, S. N., Jaffe, D. A., & Gustin, M. S. (2010). Release of mercury halides from KCl denuders in the presence of ozone. *Atmospheric Chemistry and Physics, 10*(17), 8197-8204. doi:10.5194/acp-10-8197-2010

Malcolm, E. G., Ford, A. C., Redding, T. A., Richardson, M. C., Strain, B. M., & Tetzner, S. W. (2009). Experimental investigation of the scavenging of gaseous mercury by sea salt aerosol. *Journal of Atmospheric Chemistry, 63*(3), 221-234. doi:10.1007/s10874-010-9165-y

Manura, J., & Manura, D. (1996-2009). Isotope distribution calculator and mass spec plotter (https://www.sisweb.com/mstools/isotope.htm). Retrieved from https://www.sisweb.com/mstools/isotope.htm

Mao, N., Antley, J., Cooper, M., Shah, N., Kadam, A., & Khalizov, A. (2021). Heterogeneous Chemistry of Mercuric Chloride on Inorganic Salt Surfaces. *The Journal of Physical Chemistry A, 125*(18), 3943-3952.

Marcus, Y. (1957). Mercury(II) halide mixed complexes in solution. I. The experimental method and the distribution of the neutral complex. *Acta Chemica Scandinavica, 11*, 329-339. doi:10.3891/acta.chem.scand.11-0329

Martell, A. E., & Smith, R. M. (1974). *Critical stability constants* (Vol. 1). New. York, London: Springer.

Marusczak, N., Sonke, J. E., Fu, X., & Jiskra, M. (2017). Tropospheric GOM at the Pic du Midi Observatory Correcting Bias in Denuder Based Observations. *Environmental Science & Technology, 51*(2), 863-869.

Matthiessen, A. (1996). Kinetic aspects of the reduction of mercury ions by humic substances. *Fresenius' Journal of Analytical Chemistry, 354*(5), 747-749.

Matthiessen, A. (1998). Reduction of divalent mercury by humic substances—kinetic and quantitative aspects. *Science of the Total Environment, 213*(1-3), 177-183.

Maya, J. (1977). Ultraviolet absorption cross sections of HgI2, HgBr2, and tin (II) halide vapors. *The Journal of Chemical Physics, 67*(11), 4976-4980. doi:10.1063/1.434681

McCabe, J., & Abbatt, J. P. D. (2009). Heterogeneous Loss of Gas-Phase Ozone on n-Hexane Soot Surfaces: Similar Kinetics to Loss on Other Chemically Unsaturated Solid Surfaces. *Journal of Physical Chemistry C, 113*(6), 2120-2127. doi:10.1021/jp806771q

McClure, C. D., Jaffe, D. A., & Edgerton, E. S. (2014). Evaluation of the KCl denuder method for gaseous oxidized mercury using HgBr2 at an in-service AMNet site. *Environmental Science & Technology, 48*(19), 11437-11444.

Mount, G. H., & Eisele, F. L. (1992). An Intercomparison of Tropospheric OH Measurements at Fritz Peak Observatory, Colorado. *Science, 256*(5060), 1187. doi:10.1126/science.256.5060.1187

Munthe, J., Wängberg, I., Pirrone, N., Iverfeldt, Å., Ferrara, R., Ebinghaus, R., Feng, X., Gårdfeldt, K., Keeler, G., & Lanzillotta, E. (2001). Intercomparison of methods for sampling and analysis of atmospheric mercury species. *Atmospheric Environment, 35*(17), 3007-3017.

Naharro, R., Esbrí, J. M., Amorós, J. Á., García-Navarro, F. J., & Higueras, P. (2019). Assessment of mercury uptake routes at the soil-plant-atmosphere interface. *Geochemistry: Exploration, Environment, Analysis, 19*(2), 146-154.

National Institute of Standards and Technology XPS database. (2012). http://srdata.nist.gov/xps/).

Obrist, D., Agnan, Y., Jiskra, M., Olson, C. L., Colegrove, D. P., Hueber, J., Moore, C. W., Sonke, J. E., & Helmig, D. (2017). Tundra uptake of atmospheric elemental mercury drives Arctic mercury pollution. *Nature, 547*(7662), 201-204. doi:10.1038/nature22997

Obrist, D., Kirk, J. L., Zhang, L., Sunderland, E. M., Jiskra, M., & Selin, N. E. (2018). A review of global environmental mercury processes in response to human and natural perturbations: Changes of emissions, climate, and land use. *Ambio, 47*(2), 116-140.

Pandey, S. K., Kim, K.-H., & Brown, R. J. C. (2011). Measurement techniques for mercury species in ambient air. *TrAC Trends in Analytical Chemistry, 30*(6), 899-917. doi:https://doi.org/10.1016/j.trac.2011.01.017

Parrella, J., Jacob, D. J., Liang, Q., Zhang, Y., Mickley, L. J., Miller, B., Evans, M., Yang, X., Pyle, J., & Theys, N. (2012). Tropospheric bromine chemistry: implications for present and pre-industrial ozone and mercury. *Atmospheric Chemistry and Physics, 12*(15), 6723-6740.

Pöschl, U. (2005). Atmospheric aerosols: composition, transformation, climate and health effects. *Angewandte Chemie International Edition, 44*(46), 7520-7540.

Pöschl, U., Canagaratna, M., Jayne, J. T., Molina, L. T., Worsnop, D. R., Kolb, C. E., & Molina, M. J. (1998). Mass Accommodation Coefficient of H_2SO_4 Vapor on Aqueous Sulfuric Acid Surfaces and Gaseous Diffusion Coefficient of H_2SO_4 in N_2/H_2O. *The Journal of Physical Chemistry A, 102*(49), 10082-10089. doi:10.1021/jp982809s

Pöschl, U., Rudich, Y., & Ammann, M. (2007). Kinetic model framework for aerosol and cloud surface chemistry and gas-particle interactions – Part 1: General equations, parameters, and terminology. *Atmospheric Chemistry and Physics, 7*(23), 5989-6023. doi:10.5194/acp-7-5989-2007

Pye, H. O., Nenes, A., Alexander, B., Ault, A. P., Barth, M. C., Clegg, S. L., Collett Jr, J. L., Fahey, K. M., Hennigan, C. J., & Herrmann, H. (2020). The acidity of atmospheric particles and clouds. *Atmospheric Chemistry and Physics, 20*(8), 4809-4888.

Qiu, C., Wang, L., Lal, V., Khalizov, A. F., & Zhang, R. (2011). Heterogeneous Reactions of Alkylamines with Ammonium Sulfate and Ammonium Bisulfate. *Environmental Science & Technology, 45*(11), 4748-4755. doi:10.1021/es1043112

Quinn, P. K., Collins, D. B., Grassian, V. H., Prather, K. A., & Bates, T. S. (2015). Chemistry and Related Properties of Freshly Emitted Sea Spray Aerosol. *Chemical Reviews, 115*(10), 4383-4399. doi:10.1021/cr500713g

Radenović, N., Kaminski, D., van Enckevort, W., Graswinckel, S., Shah, I., in 't Veld, M., Algra, R., & Vlieg, E. (2006). Stability of the polar {111} NaCl crystal face. *The Journal of Chemical Physics, 124*(16), 164706. doi:10.1063/1.2185621

Rice, K. M., Walker Jr, E. M., Wu, M., Gillette, C., & Blough, E. R. (2014). Environmental mercury and its toxic effects. *Journal of Preventive Medicine and Public Health, 47*(2), 74.

Ruf, R., & Treadwell, W. (1954). Zur Kenntnis des Dampfdrucks von Quecksilber (II) - chlorid. *Helvetica Chimica Acta, 37*(7), 1941-1948.

Rutter, & Schauer, J. J. (2007). The impact of aerosol composition on the particle to gas partitioning of reactive mercury. *Environmental Science & Technology, 41*(11), 3934-3939. doi:10.1021/es062439i

Rutter, Schauer, J. J., Shafer, M. M., Creswell, J. E., Olson, M. R., Robinson, M., Collins, R. M., Parman, A. M., Katzman, T. L., & Mallek, J. L. (2011). Dry deposition of gaseous elemental mercury to plants and soils using mercury stable isotopes in a controlled environment. *Atmospheric Environment, 45*(4), 848-855.

Saiz-Lopez, A., Sitkiewicz, S. P., Roca-Sanjuán, D., Oliva-Enrich, J. M., Dávalos, J. Z., Notario, R., Jiskra, M., Xu, Y., Wang, F., Thackray, C. P., Sunderland, E. M., Jacob, D. J., Travnikov, O., Cuevas, C. A., Acuña, A. U., Rivero, D., Plane, J. M. C., Kinnison, D. E., & Sonke, J. E. (2018). Photoreduction of gaseous oxidized mercury changes global atmospheric mercury speciation, transport and deposition. *Nature Communications, 9*(1), 4796. doi:10.1038/s41467-018-07075-3

Saiz-Lopez, A., Travnikov, O., Sonke, J. E., Thackray, C. P., Jacob, D. J., Carmona-García, J., Francés-Monerris, A., Roca-Sanjuán, D., Acuña, A. U., & Dávalos, J. Z. (2020). Photochemistry of oxidized Hg (I) and Hg (II) species suggests missing mercury oxidation in the troposphere. *Proceedings of the National Academy of Sciences, 117*(49), 30949-30956.

Sakamoto, Y., Inomata, S., & Hirokawa, J. (2013). Oligomerization reaction of the Criegee intermediate leads to secondary organic aerosol formation in ethylene ozonolysis. *The Journal of Physical Chemistry A, 117*(48), 12912-12921.

Salcedo, D., Villalta, P. W., Varutbangkul, V., Wormhoudt, J. C., Miake-Lye, R. C., Worsnop, D. R., Ballenthin, J. O., Thorn, W. F., Viggiano, A. A., Miller, T. M., Flagan, R. C., & Seinfeld, J. H. (2004). Effect of relative humidity on the detection of sulfur dioxide and sulfuric acid using a chemical ionization mass spectrometer. *International Journal of Mass Spectrometry, 231*(1), 17-30. doi:10.1016/j.ijms.2003.09.005

Sander, R. (1999). Modeling Atmospheric Chemistry: Interactions between Gas-Phase Species and Liquid Cloud/Aerosol Particles. *Surveys in Geophysics, 20*(1), 1-31. doi:10.1023/A:1006501706704

Sather, M. E., Mukerjee, S., Smith, L., Mathew, J., Jackson, C., Callison, R., Scrapper, L., Hathcoat, A., Adam, J., Keese, D., Ketcher, P., Brunette, R., Karlstrom, J., & Van der Jagt, G. (2013). Gaseous oxidized mercury dry deposition measurements in the Four Corners area and Eastern Oklahoma, U.S.A. *Atmospheric Pollution Research, 4*(2), 168-180. doi:https://doi.org/10.5094/APR.2013.017

Schoon, N., Amelynck, C., Bultinck, P., & Arijs, E. (2002). Study of ion/molecule reactions of atmospherically important negative ions with methane sulfonic acid. *International Journal of Mass Spectrometry, 221*(3), 209-218. doi:https://doi.org/10.1016/S1387-3806(02)00998-3

Schroeder, W. H., Anlauf, K. G., Barrie, L. A., Lu, J. Y., Steffen, A., Schneeberger, D. R., & Berg, T. (1998a). Arctic springtime depletion of mercury. *Nature, 394*(6691), 331-332. doi:10.1038/28530

Schroeder, W. H., & Munthe, J. (1998b). Atmospheric mercury—an overview. *Atmospheric Environment, 32*(5), 809-822.

Schwartz, S. E. (1986). Mass-transport considerations pertinent to aqueous phase reactions of gases in liquid-water clouds. In Jaeschke, W. (Ed.), Chemistry of Multiphase Atmospheric Systems, NATO ASI Series (Vol. G6, pp. 415-471).

Selin, N. E., & Jacob, D. J. (2008). Seasonal and spatial patterns of mercury wet deposition in the United States: Constraints on the contribution from North American anthropogenic sources. *Atmospheric Environment, 42*(21), 5193-5204. doi:https://doi.org/10.1016/j.atmosenv.2008.02.069

Selin, N. E., Jacob, D. J., Park, R. J., Yantosca, R. M., Strode, S., Jaeglé, L., & Jaffe, D. (2007). Chemical cycling and deposition of atmospheric mercury: Global constraints from observations. *Journal of Geophysical Research: Atmospheres, 112*(D2), D02308. doi:10.1029/2006jd007450

Shah, V., Jacob, D. J., Thackray, C. P., Wang, X., Sunderland, E. M., Dibble, T. S., Saiz-Lopez, A., Černušák, I., Kellö, V., & Castro, P. J. (2021). Improved mechanistic model of the atmospheric redox chemistry of mercury. *Environmental Science & Technology, 55*(21), 14445-14456.

Shepler, B. C., Balabanov, N. B., & Peterson, K. A. (2007). Hg plus Br -> HgBr recombination and collision-induced dissociation dynamics. *Journal of Chemical Physics 127*(16). doi:164304

Shepler, B. C., & Peterson, K. A. (2003). Mercury monoxide: A systematic investigation of its ground electronic state. *Journal of Physical Chemistry A, 107*(11), 1783-1787.

Singh, J., Huang, P., Hammer, U., & Liaw, W. (1996). Influence of citric acid and glycine on the adsorption of mercury (II) by kaolinite under various pH conditions. *Clays and Clay Minerals, 44*(1), 41-48.

Sjoberg, S. (1977). Metal complexes with mixed ligands. 11. The formation of ternary mononuclear and polynuclear mercury(II) complexes in the system mercury(2+) ion-chloride ion-hydroxide ion. A potentiometric study in 3.0 M sodium perchlorate, chlorine media. *Acta Chemica Scandinavica, Ser. A, A31*(9), 705-717.

Sommar, J., Gårdfeldt, K., Strömberg, D., & Feng, X. (2001). A kinetic study of the gas-phase reaction between the hydroxyl radical and atomic mercury. *Atmospheric Environment, 35*(17), 3049-3054.

Sommar, J., Hallquist, M., Ljungström, E., & Lindqvist, O. (1997). On the gas phase reactions between volatile biogenic mercury species and the nitrate radical. *Journal of Atmospheric Chemistry, 27*(3), 233-247.

Song, S., Gao, M., Xu, W., Shao, J., Shi, G., Wang, S., Wang, Y., Sun, Y., & McElroy, M. B. (2018). Fine-particle pH for Beijing winter haze as inferred from different thermodynamic equilibrium models. *Atmospheric Chemistry and Physics, 18*(10), 7423-7438.

Spiro, T. G., & Hume, D. N. (1961). The Uncharged Mixed Halides of Mercury(II). Equilibrium Constants and Ultraviolet Spectra1. *Journal of the American Chemical Society, 83*(21), 4305-4310. doi:10.1021/ja01482a001

Stamenkovic, J., & Gustin, M. S. (2009). Nonstomatal versus stomatal uptake of atmospheric mercury. *Environmental Science & Technology, 43*(5), 1367-1372.

Stratton, W., & Lindberg, S. (1995). Use of a refluxing mist chamber for measurement of gas-phase mercury (II) species in the atmosphere. In *Mercury as a Global Pollutant* (pp. 1269-1278): Springer.

Stull, D. R. (1947). Inorganic compounds. *Industrial & Engineering Chemistry, 39*(4), 540-550.

Sun, Y., Jiang, Q., Xu, Y., Ma, Y., Zhang, Y., Liu, X., Li, W., Wang, F., Li, J., & Wang, P. (2016). Aerosol characterization over the North China Plain: Haze life cycle and biomass burning impacts in summer. *Journal of Geophysical Research: Atmospheres, 121*(5), 2508-2521.

Surratt, J. D., Lewandowski, M., Offenberg, J. H., Jaoui, M., Kleindienst, T. E., Edney, E. O., & Seinfeld, J. H. (2007). Effect of acidity on secondary organic aerosol formation from isoprene. *Environmental Science & Technology, 41*(15), 5363-5369.

Swartzendruber, P., Jaffe, D., & Finley, B. (2009). Development and first results of an aircraft-based, high time resolution technique for gaseous elemental and reactive (oxidized) gaseous mercury. *Environmental Science & Technology, 43*(19), 7484-7489.

Tacey, S. A., Szilvási, T., Xu, L., Schauer, J. J., & Mavrikakis, M. (2018a). The role of iron-oxide aerosols and sunlight in the atmospheric reduction of Hg(II) species: A DFT+U study. *Applied Catalysis B: Environmental, 234*, 347-356. doi:https://doi.org/10.1016/j.apcatb.2018.04.049

Tacey, S. A., Xu, L., Mavrikakis, M., & Schauer, J. J. (2016). Heterogeneous Reduction Pathways for Hg(II) Species on Dry Aerosols: A First-Principles Computational Study. *The Journal of Physical Chemistry A, 120*(13), 2106-2113. doi:10.1021/acs.jpca.5b12769

Tacey, S. A., Xu, L., Szilvási, T., Schauer, J. J., & Mavrikakis, M. (2018b). Quantum chemical calculations to determine partitioning coefficients for $HgCl_2$ on iron-oxide aerosols. *Science of the Total Environment, 636*, 580-587. doi:https://doi.org/10.1016/j.scitotenv.2018.04.289

Tang, I. N. (1996). Chemical and size effects of hygroscopic aerosols on light scattering coefficients. *J. Geophys. Res.-Atmos., 101*(D14), 19245-19250.

Tong, X., Barat, R. B., & Poulos, A. T. (1999). Detection of Mercuric Bromide in a Gas Phase Flow Cell by Laser Photofragment Fluorescence Spectroscopy. *Environmental Science & Technology, 33*(18), 3260-3263. doi:10.1021/es9813461

Tong, Y., Eichhorst, T., Olson, M. R., McGinnis, J. E., Turner, I., Rutter, A. P., Shafer, M. M., Wang, X., & Schauer, J. J. (2013). Atmospheric photolytic reduction of Hg(ii) in dry aerosols. *Environmental Science: Processes & Impacts, 15*(10), 1883-1888. doi:10.1039/C3EM00249G

Tossell, J. A. (2003). Calculation of the energetics for oxidation of gas-phase elemental Hg by Br and BrO. *Journal of Physical Chemistry A, 107*(39), 7804-7808.

Travnikov, O., Angot, H., Artaxo, P., Bencardino, M., Bieser, J., D'Amore, F., Dastoor, A., De Simone, F., Diéguez, M. D. C., Dommergue, A., Ebinghaus, R., Feng, X. B., Gencarelli, C. N., Hedgecock, I. M., Magand, O., Martin, L., Matthias, V., Mashyanov, N., Pirrone, N., Ramachandran, R., Read, K. A., Ryjkov, A., Selin, N. E., Sena, F., Song, S., Sprovieri, F., Wip, D., Wängberg, I., & Yang, X. (2017). Multi-model study of mercury dispersion in the atmosphere: atmospheric processes and model evaluation. *Atmospheric Chemistry and Physics, 17*(8), 5271-5295. doi:10.5194/acp-17-5271-2017

Trimble, V. (1987). *CRC Handbook of Chemistry and Physics* (Vol. 1). Cleveland, Ohio: Boca Raton.

Tröstl, J., Chuang, W. K., Gordon, H., Heinritzi, M., Yan, C., Molteni, U., Ahlm, L., Frege, C., Bianchi, F., Wagner, R., Simon, M., Lehtipalo, K., Williamson, C., Craven, J. S., Duplissy, J., Adamov, A., Almeida, J., Bernhammer, A.-K., Breitenlechner, M., Brilke, S., Dias, A., Ehrhart, S., Flagan, R. C., Franchin, A., Fuchs, C., Guida, R., Gysel, M., Hansel, A., Hoyle, C. R., Jokinen, T., Junninen, H., Kangasluoma, J., Keskinen, H., Kim, J., Krapf, M., Kürten, A., Laaksonen, A., Lawler, M., Leiminger, M., Mathot, S., Möhler, O., Nieminen, T., Onnela, A., Petäjä, T., Piel, F. M., Miettinen, P., Rissanen, M. P., Rondo, L., Sarnela, N., Schobesberger, S., Sengupta, K., Sipilä, M., Smith, J. N., Steiner, G., Tomè, A., Virtanen, A., Wagner, A. C., Weingartner, E., Wimmer, D., Winkler, P. M., Ye, P., Carslaw, K. S., Curtius, J., Dommen, J., Kirkby, J., Kulmala, M., Riipinen, I., Worsnop, D. R., Donahue, N. M., & Baltensperger, U. (2016). The role of low-volatility organic compounds in initial particle growth in the atmosphere. *Nature, 533*(7604), 527-531. doi:10.1038/nature18271

Valadbeigi, Y., Ilbeigi, V., Vahidi, M., Michalczuk, B., Matejcik, S., & Tabrizchi, M. (2020). Online detection and measurement of elemental mercury vapor by ion mobility spectrometry with chloroform dopant. *Journal of Chromatography A, 1634*, 461676.

Veres, P., Roberts, J. M., Warneke, C., Welsh-Bon, D., Zahniser, M., Herndon, S., Fall, R., & de Gouw, J. (2008). Development of negative-ion proton-transfer chemical-ionization mass spectrometry (NI-PT-CIMS) for the measurement of gas-phase organic acids in the atmosphere. *International Journal of Mass Spectrometry, 274*(1-3), 48-55.

Viggiano, A. A. (1993). In-situ mass-spectrometry and ion chemistry in the stratosphere and troposphere. *Mass Spectrometry Reviews 12*(2), 115-137.

Viggiano, A. A., Fernandez, A. I., & Troe, J. (2005). Ion-molecule kinetics at 15-700 Torr. *Physical Chemistry Chemical Physics 7*(7), 1533-1539. doi:10.1039/b417454b

Viggiano, A. A., Seeley, J. V., Mundis, P. L., Williamson, J. S., & Morris, R. A. (1997). Rate constants for the reactions of XO3-(H2O)(n) (X = C, HC, and N) and NO3-(HNO3)(n) with H2SO4: Implications for atmospheric detection of H2SO4. *Journal of Physical Chemistry A, 101*(44), 8275-8278.

Viidanoja, J., Reiner, T., & Arnold, F. (1998). Laboratory investigations of negative ion molecule reactions of formic and acetic acids: implications for atmospheric measurements by ion-molecule reaction mass spectrometry. *International Journal of Mass Spectrometry, 181*, 31-41.

Wang, F., Saiz-Lopez, A., Mahajan, A., Gómez Martín, J., Armstrong, D., Lemes, M., Hay, T., & Prados-Roman, C. (2014). Enhanced production of oxidised mercury over the tropical Pacific Ocean: a key missing oxidation pathway. *Atmospheric Chemistry and Physics*.

Wang, Q., Zhang, L., Liang, X., Yin, X., Zhang, Y., Zheng, W., Pierce, E. M., & Gu, B. (2020). Rates and Dynamics of Mercury Isotope Exchange between Dissolved Elemental Hg(0) and Hg(II) Bound to Organic and Inorganic Ligands. *Environmental Science & Technology, 54*(23), 15534-15545. doi:10.1021/acs.est.0c06229

Warneke, C., van der Veen, C., Luxembourg, S., de Gouw, J. A., & Kok, A. (2001). Measurements of benzene and toluene in ambient air using proton-transfer-reaction mass spectrometry: calibration, humidity dependence, and field intercomparison. *Int. J. Mass Spectrom., 207*(3), 167-182. doi:https://doi.org/10.1016/S1387-3806(01)00366-9

Wright, L. P., Zhang, L., & Marsik, F. J. (2016). Overview of mercury dry deposition, litterfall, and throughfall studies. *Atmospheric Chemistry and Physics, 16*(21), 13399-13416. doi:10.5194/acp-16-13399-2016

Wu, R., Wang, C., & Dibble, T. S. (2020). First experimental kinetic study of the atmospherically important reaction of BrHg + NO2. *Chemical Physics Letters*, 137928. doi:https://doi.org/10.1016/j.cplett.2020.137928

Wu, R., Wang, C., & Dibble, T. S. (2021). First experimental studies of the kinetics of BrHg reactions with O3 and abundant free radicals. *AGU Fall Meeting 2021*.

Xiao, Z., Munthe, J., & Lindqvist, O. (1991). Sampling and determination of gaseous and particulate mercury in the atmosphere using gold-coated denuders. *Water Air & Soil Pollution, 56*(1), 141-151.

Yamato, M., & Tanaka, H. (1994). Aircraft observations of aerosols in the free marine troposphere over the North Pacific Ocean: Particle chemistry in relation to air mass origin. *Journal of Geophysical Research: Atmospheres, 99*(D3), 5353-5377. doi:https://doi.org/10.1029/93JD03191

Yan, C., Nie, W., Äijälä, M., Rissanen, M. P., Canagaratna, M. R., Massoli, P., Junninen, H., Jokinen, T., Sarnela, N., Häme, S. A. K., Schobesberger, S., Canonaco, F., Yao, L., Prévôt, A. S. H., Petäjä, T., Kulmala, M., Sipilä, M., Worsnop, D. R., & Ehn, M. (2016). Source characterization of highly oxidized multifunctional compounds in a boreal forest environment using positive matrix factorization. *Atmospheric Chemistry and Physics, 16*(19), 12715-12731. doi:10.5194/acp-16-12715-2016

Yaws, C. L. (2012; 2013; 2014). *Yaws' Critical Property Data for Chemical Engineers and Chemists*. In. Retrieved from https://app.knovel.com/hotlink/toc/id:kpYCPDCECD/yaws-critical-property/yaws-critical-property

Ye, Z., Mao, H., Lin, C. J., & Kim, S. Y. (2016). Investigation of processes controlling summertime gaseous elemental mercury oxidation at midlatitudinal marine, coastal, and inland sites. *Atmospheric Chemistry and Physics*, *16*(13), 8461-8478. doi:10.5194/acp-16-8461-2016

Zhang, L., Liang, X., Wang, Q., Zhang, Y., Yin, X., Lu, X., Pierce, E. M., & Gu, B. (2021). Isotope exchange between mercuric [Hg(II)] chloride and Hg(II) bound to minerals and thiolate ligands: Implications for enriched isotope tracer studies. *Geochimica et Cosmochimica Acta, 292*, 468-481. doi:https://doi.org/10.1016/j.gca.2020.10.013

Zhang, Y., & Banks, C. (2006). A comparison of the properties of polyurethane immobilised Sphagnum moss, seaweed, sunflower waste and maize for the biosorption of Cu, Pb, Zn and Ni in continuous flow packed columns. *Water Research, 40*(4), 788-798.

Zhao, J., Eisele, F. L., Titcombe, M., Kuang, C., & McMurry, P. H. (2010). Chemical ionization mass spectrometric measurements of atmospheric neutral clusters using the cluster-CIMS. *Journal of Geophysical Research, 115*(D8). doi:10.1029/2009jd012606

Zhao, R., Mungall, E. L., Lee, A. K., Aljawhary, D., & Abbatt, J. P. (2014). Aqueous-phase photooxidation of levoglucosan–a mechanistic study using aerosol time-of-flight chemical ionization mass spectrometry (Aerosol ToF-CIMS). *Atmospheric Chemistry and Physics, 14*(18), 9695-9706.

Zheng, J., Khalizov, A., Wang, L., & Zhang, R. (2010). Atmospheric Pressure-Ion Drift Chemical Ionization Mass Spectrometry for Detection of Trace Gas Species. *Analytical Chemistry 82*(17), 7302-7308. doi:10.1021/ac101253n

Zhou, H., Zhou, C., Hopke, P. K., & Holsen, T. M. (2018). Mercury wet deposition and speciated mercury air concentrations at rural and urban sites across New York state: Temporal patterns, sources and scavenging coefficients. *Science of the Total Environment*, *637-638*, 943-953. doi:https://doi.org/10.1016/j.scitotenv.2018.05.047